Abstract:

The presented study investigates the vacuum induction re-melting of Ti-46Al-7Nb (at%) intermetallic alloy in a refractory crucible based on Y_2O_3. A series of re-melting experiments were performed at melting temperatures of 1630 ºC, 1680 ºC and 1730 ºC and three ranges of melting times (5, 15 and 30 minutes). Metallographic cross-sections for each experiment were prepared to obtain data for the microstructure and phase composition evaluation using SEM and EDS. A quantitative assessment of microstructure was based on Adaptive Contrast Control (ACC) software used to estimate a volume fraction of ceramic phase in the melt. The oxygen content in the solidified met was analyzed using the Inert Gas Fusion (IGF) method. The thermodynamic calculation of possible reactions is presented regarding the activity of the individual elements of the intermetallic and refractory crucible. Data presented in this work based on experimental results and thermodynamic calculation could be used as a guide for further melting and optimization of the TiAlNb melting process.

Key words:

TiAl intermetallic, vacuum induction melting, refractory crucible melting, inert gas fusion, volume fraction of pollutants.

Abstrakt:

Prezentovaná práce se zabývá vakuovým indukčním tavením intermetalické slitiny Ti-46Al-7Nb (at. %) v žáruvzdorných kelímcích na bázi Y_2O_3. Byla provedena série taveb pro teploty přehřátí taveniny 1630, 1680 and 1730 ºC a při různých dobách výdrže na této teplotě v rozmezí 5 až 30 minut. Ze slitin ztuhlých v tavících kelímcích byly připraveny metalografické výbrusy, které sloužily k hodnocení mikrostruktury a vyhodnocení složení fází. Pro získání těchto dat byly použity metosy elektronové mirkoskopie SEM a EDS. Kvantitativní hodnocení mikrostruktury, zejména obsahu oxidické faze ve slitině, bylo provedeno pomocí software Adaptive Contrast Control (ACC). Analýza obsahu kyslíku ve ztuhlé slitině byla provedena metodou IGF (fůze v inertním plynu). V této práci jsou pochody na rozhraní slitina/oxidický kelímek posuzován take z termodynamického hlediska a to s použitím aktivit jednotlivých složek v systému. Data prezentovaná v této práci mohou být použita pro nastavení a optimalizaci procesů tavení intermetalik TiAlNb.

Klíčová slova:

Intermetalikum TiAl, vakuové indukční tavení, taveni v žáruvzdornývh kelímcích, fůze v inertním plynu, oběmový podíl nečistot.

Bibliography of the Thesis

BARTÁK, T. Processing of Nb-containing TiAl Intermetallics and its Physical and Chemical Aspects. Brno: University of Technology Brno, Faculty of Chemistry, 2014, 82 p. Supervisor: prof. RNDr. Antonín Dlouhý, CSc., Supervisor-specialist: prof. Ing. Jaromír Havlica, DrCs.

Declaration:

I declare, that my PhD. dissertation "Processing of Nb-containing TiAl Intermetallics and its Physical and Chemical Aspects" was written on my own under the supervision of prof. RNDr. Antonín Dlouhý, CSc. All quotations from the used literary sources are accurate and complete.

Brno, 30.6.2014: .....

signature

Acknowledgement

The author of the dissertation thanks prof. RNDr. Antonín Dlouhý CSc, for supervising the doctoral study. Further thanks go to prof. Ing. Ladislav Zemčík, CSc, for his valuable help with the experimental part of this work. Many thanks to my colleagues at the Institute of Physics of Materials AS CR and all who worked together with us to achieve the results of this work.

Financial support was received from the Czech Science Foundation, contract number 106/07/0762 and a part of the study was supported within GA AS project number 1QS200410502.

Special thanks to my family for their support and patience during the whole study.

Contents

1. INTRODUCTION: **9**

2. TIAL ALLOYS: **11**

2.1. MICROSTRUCTURE 13
2.2. FRACTURE BEHAVIOUR 14

3. MELTING OF TIAL INTERMETALLICS **17**

3.1. YTTRIUM (TRI)-OXIDE 18

4. THERMODYNAMICS AND KINETICS ASPECTS OF VIM: **19**

4.1. FREE ENERGY CHANGE AND DRIVING FORCE OF CHEMICAL REACTIONS 19
4.2. THERMODYNAMICS OF CHEMICAL REACTIONS 20
4.3. GIBBS FREE ENERGY AND EQUILIBRIUM CONSTANT RELATIONSHIP 21
4.3.1. ADDITION OF REACTANTS OR PRODUCTS 23
4.3.2. TREATMENT OF ACTIVITY 24
4.3.3. EFFECT OF TEMPERATURE 24
4.5. DISSOLUTION OF Y_2O_3 IN TIALNB MELT 25

5. OBJECTIVES: **27**

6. EXPERIMENTAL: **29**

6.1. ACC (ADAPTIVE CONTRAST CONTROL) ANALYSES 31
6.2. OXYGEN CONTENT ANALYSES 32
6.3. THERMOCOUPLES 33
6.4. TEM LAMELLA PREPARATION USING SEM-FIB MICROSCOPE 33

7. RESULTS: **35**

7.1. THERMODYNAMICS CALCULATIONS 36
7.2. EXPERIMENTAL RESULTS 39
7.2.1. Y_2O_3 CRUCIBLES 39
7.2.2. MELTING EXPERIMENTS 39
7.2.3. VOLUME FRACTION OF CERAMICS PARTICLES 65
7.2.4. OXYGEN CONTENT 65

8. DISCUSSION: **69**

9. CONCLUSIONS: **72**

10. REFERENCES: **77**

1. Introduction:

Gamma titanium aluminides are intermetallic compounds based on the $L1_0$ type crystal lettice. Although the development of TiAl based alloys began about 40 years ago, the alloys have only been used in applications since about the year 2000. A wide range of potentially useful alloys containing three major intermetallic phases has been investigated: gamma - TiAl, alfa$_2$ - Ti_3Al and $TiAl_3$. Among the three, gamma TiAl received the most interest and has a highest number of possible applications. This phase - gamma TiAl has excellent mechanical properties and oxidation/corrosion resistance at elevated temperatures (above 600ºC). Generally, all these alloys are lightweight and resistant to oxidation and heat however they suffer from low ductility at room temperature. Titanium aluminides have limited heat workability. The density of gamma TiAl is about 4.0 g/cm³, which would result in weight savings of up to 50% over conventional Ni-based heat-resistant superalloys [1-3]. Their use is anticipated in several applications including automobiles and aircraft structures [1]. TiAl-based alloys have a strong potential to increase the thrust-to-weight ratio of aircraft engines [1]. This is especially valid for the engine's low-pressure turbine blades and the high-pressure compressor blades. These parts are usually made from a Ni-based superalloy, which is nearly twice as heavy as TiAl based alloys [4].

TiAl base alloys have generally proved difficult to process. The main disadvantage of this material class is several-fold higher production costs, as compared to similar Ni-based alloys. Induction skull melting (ISM) is the method of choice for melting reactive alloys because ISM has many advantages compared to other melting technologies [5, 6] such as classical vacuum induction melting (VIM) based on a refractory crucible [7]. The VIM melting route is cost-effective and the melt can, in principle, be overheated to any targeted pouring temperature provided if that melt-crucible and melt - furnace atmosphere interactions do not deteriorate the purity of the alloy [8]. In this research, reactivity of melt with yttria refractory during the VIM process has been investigate at temperatures between the range of 1630 ºC and 1730 ºC. Moreover, it is well know that the mechanical properties of TiAl base alloys are modified by the size and distribution of oxide inclusion particles. Therefore, in this research, the morphology, size and distribution of Y_2O_3 particles and their effects on microstructure, have been investigated together with the related oxygen content.

2. TiAl alloys:

TiAl-based alloys are one of the most advanced intermetallics that have successfully demonstrated their application potential in the aerospace and automotive industries. These intermetallics are being considered for military and civil applications such as turbine blades, exhaust valves and turbo charger rotors [1, 6]. The most attractive properties of TiAl-based intermetallics, when compared to similar Ni-based alloys, are low mass density, high specific strength, good oxidation resistance, high stiffness and strength at elevated temperature [1, 5]. Another significant feature enhancement of TiAl alloys is due to the addition of Nb [9]. A ternary phase diagram depicting the composition range relevant for applications (where the ratio of Al and Ti is approximately stechiometric and Nb composition is close to 7 at. %) is shown in Fig. 1.

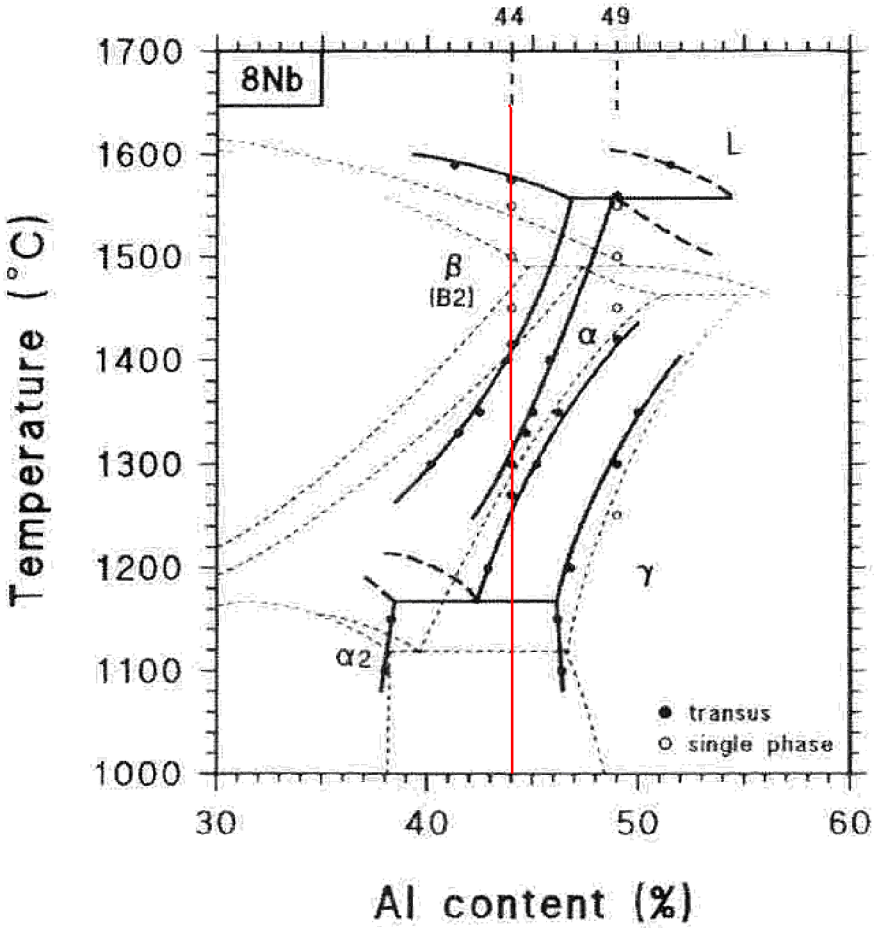

Fig. 1: Relevant section of the TiAlNb ternary phase diagram [10] at 8 at. % Nb - used alloy is marked by red line.

TiAl-based alloys consist of two phases (see Table 1) [2, 11, 12]. The majority phase is the ordered gamma TiAl phase with the tetragonal (FCT face-centered-tetragonal) structure. The minor phase Ti_3Al is the ordered with hexagonal (HCP hexagonal close-packed) lattice structure of the type DO_{19} and is known as α2. The crystal structures of both phases are shown in Figure 2.

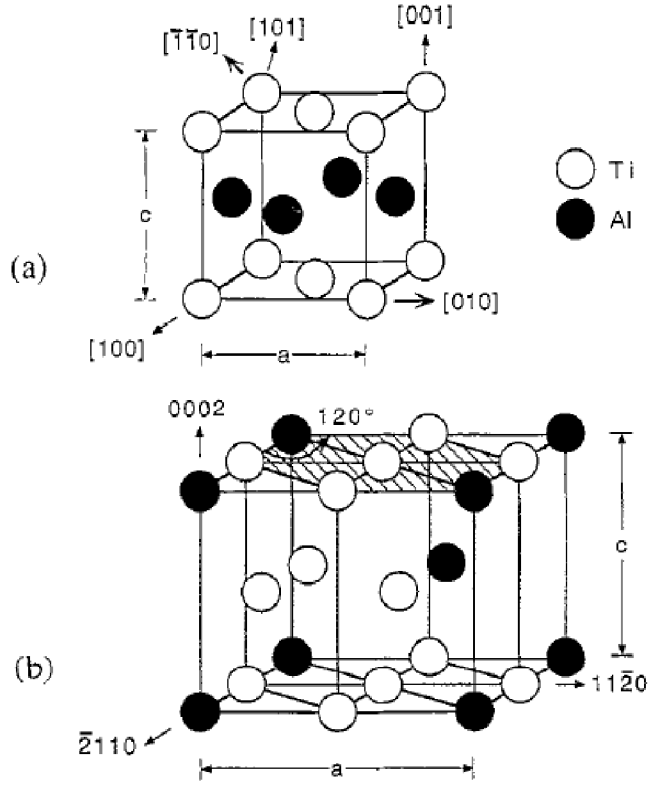

Fig 2: Lattice structure of (a) γ-TiAl phase and (b) α_2-Ti_3Al phase

The Al content in TiAl-based alloys has great effects on the microstructure and high-temperature strength [9]. Important parameters are summarized in Table 1. When decreasing the Al content, the volume fraction of the α2 phase increases. The average spacing between γ/γ′ and γ/α_2 lemallae decreases linearly with increasing the volume fraction of the α_2 phase. The best ductility typically occurs in the range between 46-50 atomic percent (at.%) Al, and increasing Al generally decreases the fracture toughness. The lamellar colony size in the cast TiAl-based alloys (with 44–50 at.% Al) increases monotonically when increasing the Al concentration because of the increased tendency to form the gamma phase [11, 12].

The Niobium content in the TiAl alloy substantially improved the oxidation resistance and microstructure. The lamellar spacing increases with higher Al and Nb contents. However, the influence of the Nb addition on the lamellar spacing is less pronounced than when Al is added. The coarsening of the lamellar laths during exposure to high temperature occurs for all alloys, but the microstructure degradation of the alloys with high Nb contents is slower than that of the alloys without the Nb addition [13]. Moreover, the increase of the Al content reduces the niobium concentration in the melt, thus reducing the role of niobium in the grain refinement [14]. Alloys based on the Ti-Al-Nb composition comprise numerous groups of alloys [15] including, on the one hand, compounds with a low concentration of Nb, which are

based predominantly on the α_2 (HCP) phase, and, on the other hand, Nb-enriched compounds based on the orthorhombic O phase [16].

Tab 1: Properties of α_2 and γ–TiAl phase [17-22]

Property	**α_2 phase**	**γ phase**
Volume density [g·cm^{-3}]	4.1 – 4.7	3.8 – 4.0
E modulus [GPa]	120 – 145	160 – 175
Ductility [%]	2 – 5	1 – 3
Strength [MPa]	700 – 990	400 – 650
Thermal conductivity [W·m^{-1}·K^{-1}]	7	22
Melting point [°C]	1180	1440
Creep limit [°C]	750	900
Oxidation limit [°C]	650	900

2.1. Microstructure

Three important microstructures of the TiAl-based alloys are: (1) the fully lamellar (FL) microstructure consisting of α_2 + γ phases; (2) the duplex microstructure (DP) consisting of α_2+γ and γ grains; and (3) the near gamma (NG) microstructure formed predominantly by the γ phase. It has been known for long time that the γ phase is very brittle and this causes the early failure of the titanium-aluminides. The TiAl-based alloys with a fully lamellar microstructure have the most balanced properties at both room and elevated temperatures. All of these structures are shown in Figure 3 [2, 11, 17, 19].

Fully lamellar structures are generally observed in as-cast conditions, and duplex structures are formed in thermomechanically-treated alloy versions [2]. The FL microstructure consists of equiaxed polycrystalline grains with densely-packed lamellae. The lamellae are composed of α_2 plates interspersed between many γ plates. The DP microstructure, however, is made up of lamellar grains with single-phase γ grains distributed around them [23-25].

Room-temperature (RT) tensile ductility and fracture toughness are two properties of considerable importance to the application of TiAl-based alloys [26, 27]. A great deal of research has focused on optimizing the fully lamellar (FL) structure to have a fine grain size. This is because a FL structure with a fine colony size is known to have better balanced properties than the FL structure with a large grain size and the duplex (DP) one with a fine colony size [28-32].

The coarse FL structure with a colony size of d > 500 μm, exhibit adequate fracture toughness but usually poor tensile ductility at room temperature. On the other hand, the DP structures with fine grain sizes (d < 50μm) show adequate tensile ductility but poor fracture toughness, and more importantly, poorer high temperature strengths and creep resistances, as

compared to the FL materials [33]. The room-temperature tensile yield strength, fracture strength, and ductility of the TiAl-based alloys increase when decreasing the colony size of the fully-lamellar structure is decreased. Based on these correlations, a material with fine fully lamellar (FFL) microstructures would be expected to have balanced mechanical properties [34-40].

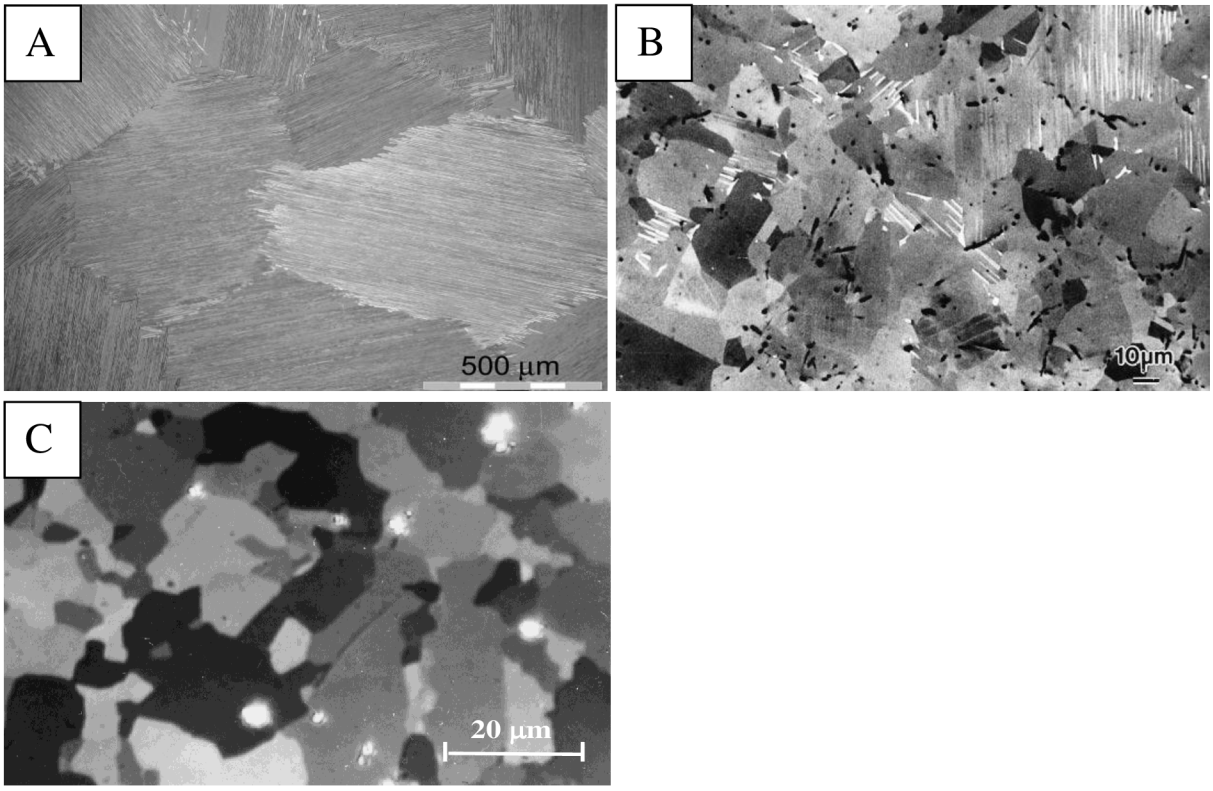

Figure 3: Types of TiAl based microstructures: (A) fully lamellar, (B) duplex, (C) equiaxed gamma.

2.2. Fracture behaviour

A characteristic mechanism of fracture of duplex materials is a grain boundary decohesion induced by plastic deformation. On the other hand, a fracture mechanism of lamellar microstructures causes delamination between the phases and cracking between the phases [41]. The lamellar microstructure is tougher than the duplex microstructure or equiaxed gamma because of the higher near-tip plasticity and an anisotropic composite-like fracture characteristic that yields a tortuous crack path, shear-ligament toughening, and improved resistance-curve behavior [29, 30, 37, 39]. The tensile ductility of the lamellar microstructure increases when the colony size is decreased, while the fracture toughness shows a maximum at a large colony size [27]. The initiation toughness of the lamellar TiAl-based alloys increases with increased grain size and the volume fraction of lamellar grains [38]. Both initiation toughness K_{IC} and the crack-growth toughness, K_S, increase with decreased lamellar spacing by affecting trans-lamellar micro cracking and the size of the shear ligaments. K_S increases with increased colony size, the volume fraction, and the width of

crackwake ligaments [42]. At a large grain size, K_S depends on the grain size indirectly through the influence of the grain size on the ligament width. The tensile ductility in the TiAl-based alloys is limited by the instability of micro cracks nucleated in the microstructure. The level of the tensile ductility depends on the K_{IC} value and the grain size [27]. High fracture toughness can be attained in large-grained lamellar TiAl-based alloys with a fine lamellae spacing (< 2 μm). The balanced properties of a moderate K_{IC} and plastic elongation (16 MPa√m and 1.5%) can be attained in the fully-lamellar TiAl alloys with a size of approximately 300 μm and a lamellae spacing of less than 2 μm [6].

3. Melting of TiAl intermetallics

Induction Skull Melting ISM is based on a segmented, water-cooled copper vessel situated in a vacuum or controlled atmosphere where the melting power is supplied via induction coil. Here, the melt is in a direct metal-to-metal contact with the crucible wall, without a refractory lining. The copper crucible is made up of water-cooled segments. The high frequency magnetic field generated by the coil, in effect, passes through the crucible to induce heat in the metal charge causing it to melt. The field also intensely stirs the liquid metal pool in the crucible. The stirring promotes a very homogeneous melt pool and effectively distributes even higher density alloying elements evenly throughout the poured casting. A thin layer of metal remains frozen against the bottom and the wall of the crucible forming a skull. The low velocity boundary layer in the liquid adjacent to the skull, together with the skull itself and the interface between the skull and the crucible wall serve as thermal resistances, reducing the heat conducted from the hot liquid into the cold crucible. The process is most often used in casting with over the lip pouring, but it can also be used in ingot production. In this case, open-bottom crucibles with a drawn down starter plug are used to slowly withdraw an ingot from top fed charge material. Induction skull melting is an energy demanding method [43, 44].

Therefore, the vacuum induction melting (VIM) method is preferable from an energy perspective. The VIM process involves the melting of metals by means of electromagnetic induction under vacuum [45-48]. Melting takes place within a furnace consisting of a refractory lining or crucible inside a water-cooled induction coil. The furnace assembly is completely enclosed by fabricated steel, a water-cooled furnace chamber that is evacuated by a series of vacuum pumps so that the charge may be melted down, refined and poured into molds under vacuum or inert gas. This process permits the refining of metals and alloys that contain elements having a strong affinity for certain gases such as oxygen. Chemical reactions, dissociation and flotation remove dissolved and chemically bonded impurities. Melt chemistry can thereby be accurately adjusted thereby producing an end product that is clean and homogeneous.

The selection of suitable materials or ceramic crucibles for melting the TiAl-based alloys using the VIM route is governed by several requirements. Important indicators of suitability are data provided by the manufacturer of ceramics, especially the speed of the crucible degradation, the particular melting cycle temperature and the maximum melting temperature (“melting points”). Stable oxides are used as refractory materials, namely oxides able to withstand temperatures above 1500ºC without chemical change and physical destruction. Their melting point is an important characteristic indicating the maximum temperature of use. From an economic point of view, the price and a number of processing cycles the material can withstand are important parameters of choice. The high productivity and continuity of production is affected by good melting pot lifetime [49]. A non-negligible

aspect is the thermodynamic stability of the ceramics used in the technological processes. It is important to find a compromise taking into account all the above aspects, because none of these parameters can be ignored.

The choice of casting mould material is a key step in the overall casting process. There is no refractory that would by completely inert as fare as the chemical reaction with the TiAl melt is concerned [50, 51]. The solidification temperatures of TiAl alloys are high (1550–1600 °C) and depend on alloying. The melt reactivity and high solidification temperatures demand more thermodynamically stable and chemically inert materials for mould manufacturing instead of traditionally applied zirconia (ZrO_2) and alumina (Al_2O_3).

3.1. Yttrium (tri)-oxide

Yttrium oxide is a white, water-insoluble, crystalline solid which is obtained mainly from the mineral Xenotim (YPO_4). The compound is used as an additive in the glass industry in order to increase the refractive index of special optical glasse. The Y_2O_3 ceramic crucibles are mainly used for high melting temperatures up to 2410 ° C and a high affinity for oxygen in situations where good thermodynamic stability is required [51].

Yttrium oxide has one of the lowest thermal conductivities of refractory oxides at high temperatures (0.007 $WK^{-1}m^{-1}$ at 1400 ºC). This property allows yttrium oxide to be used to reduce the heat flow on many substrates. Thermal expansion of yttrium oxide is moderate, like aluminum oxide. Yttrium oxide has an electrical resistivity of over 106 Ωm at room temperature and remains electrically insulating at 2000 ºC more than other refractory materials. Yttrium oxide has superior resistance to aggressive chemical attack at high temperatures and has superior thermal stability.

The resistance to molten metals, glass, slag, and salts leads to the products being used for coating crucibles and molds that handle the most highly-reactive molten materials, such as uranium, titanium, chromium, beryllium, and their alloys. Coatings of yttrium oxide are often used as barrier coatings to stop or prevent reactions, such as for diffusion bonding of reactive metals or for braze stop-off coatings [52]. A variety form of Y_2O_3 like paint, spray or electrophoretic deposition could be used [53]. Due to these properties, Y_2O_3 is one of the most stable oxides of all. Therefore, and due to the results of a previous work [48], it can be used to melt TiAl. However, due to the very high affinity of titanium and aluminum to oxygen, additional studies are required to address the possible contamination of the alloy during re-melting experiment.

4. Thermodynamics and kinetics aspects of VIM:

Reactions between intermetallics alloy and refractories can be predicted using thermodynamic calculations together with prediction criteria formulated at work [54].

Study of temperature stability in rections running at a constant pressure is important in order to predict thermodynamic equilibrium in metallurgical processes [47, 55-58]. For quantitative description of the reaction heat at a constant pressure the state function enthalpy H is used.

The enthalpy change in a reaction can be obtained by:

$$\Delta H = H_{2[products]} - H_{1[reactants]} \quad (1).$$

Reaction enthalpy ΔH depends on temperature and pressure. Therefore the standard reaction enthalpy ΔH_T^0 is usually defined as enthalpy change, where the $H_{2[products]}$ is the sum of the standard enthalpies of products and $H_{1[reactants]}$ the sum of the standard enthalpy of reactants at a standard pressure of 101 325 Pa (1atm) and constant temperature T. Typical cases of heat balance in chemical reactions are presented in Table 2..

Tab. 2: Heat balance in chemical reactions.

Exothermic reactions	**Endothermics reactions**
Released of heat.	Heat absorbing
At the end of reaction, the energy [H] is lower $\Delta H \lhd 0$	At the end of reaction, the energy [H] is higher $\Delta H \rhd 0$
$H_{1start} \rightarrow H_{2end}$	$H_{1start} \rightarrow H_{2end}$

Standard reaction enthalpy is calculated as:

$$\Delta H_T^0 = \Delta H_{Tprod}^0 - \Delta H_{Treak}^0 \quad (2).$$

The Kirchhoff equation describe the reaction enthalpy change when the temperature is changing

$$\frac{d(\Delta H)}{dT} = \Delta C_p \quad (3).$$

ΔC_p is the difference of the heat capacity of reactants and products. The integral of this reaction is used for high temperature metallurgical reactions [59-63].

$$\int_{\Delta H_{T1}}^{\Delta H_{T2}} d(\Delta H) = \Delta H_{T2} - \Delta H_{T1} = \int_{T_1}^{T_2} \Delta C_p dT \quad (4).$$

4.1. Free energy change and driving force of chemical reactions

Gibbs free energy is a thermodynamic property that predict whether a process will occur spontaneously at constant temperature and pressure. This theory was defined in 1876 by

Josiah Willard Gibbs. Gibbs free energy G is defined as $G = H - TS$ where H is enthalpy, T is temperature and S is entropy.

For reactions in which the temperature is changed during the reaction the following equation was defined:

$$\Delta G = \Delta H - T\Delta S \tag{5}.$$

Temperatures for this equation must be in Kelvin. The above equation is often referred to the Gibbs-Helmholtz equation, since the values of ΔH and ΔS are usually derived from tables of standard entropy and enthalpy.

Gibbs energy dependence on temperature can also be expressed as:

$$\left(\frac{d\left(\frac{G}{T}\right)}{dT}\right)_p = -\frac{H}{T^2} \tag{6}.$$

The equation states that the change in the $\frac{G}{T}$ ratio at constant pressure as a result of an infinitesimally small change in temperature is equal to $\frac{H}{T^2}$.

For a chemical reaction the equation reads:

$$\left(\frac{d\left(\frac{\Delta G}{T}\right)}{dT}\right)_p = -\frac{\Delta G}{T^2} \tag{7}.$$

with ΔG as the change in Gibbs energy and H as the enthalpy change

$$0 = \frac{\Delta G(T_2)}{T_2} - \frac{\Delta G(T_1)}{T_1} = \Delta H_p^0\left(\frac{1}{T_2} - \frac{1}{T_1}\right) \tag{8}.$$

This equation quickly enables the calculation of the Gibbs free energy change for a chemical reaction at any temperature T_2 with knowledge of just the Standard Gibbs free energy change of formation and the standard enthalpy change of formation for the individual components at 25°C and standard pressure.

4.2. Thermodynamics of chemical reactions

Some chemical reactions are reversible. For any reaction in the equilibrium state the rates of the forward and backward (reverse) reactions are equal. In the following equation, the arrows pointing in both ways indicate the equilibrium state of the reaction. In the general expression A and B are reactant chemical species, S and T are product species, and α, β, σ, and τ are the stechiometric coefficients of the respective reactants and products

$$\alpha A + \beta B \leftrightarrow \sigma S + \tau T \tag{9}.$$

The equilibrium state of a reaction is said to lie "far to the right" if, at equilibrium, nearly all the reactants are consumed. Conversely, the equilibrium position is said to be "far to the left" if hardly any product has formed from the reactants.

$k_+A^\alpha B^\beta$ = forward reaction rate

$k\_S^\sigma T^\tau$ = backward reaction rate

where A, B, S and T are active masses and k_+ and k_- are rate constants. Since at equilibrium forward and backward rates are equal:

$$k_+A^\alpha B^\beta = k\_S^\sigma T^\tau \quad (10).$$

and the ratio of the rate constants is also a constant, now known as an equilibrium constant.

$$K = \frac{k_+}{k_-} = \frac{[S]^\sigma [T]^\tau}{[A]^\alpha [B]^\beta} \quad (11).$$

The equality of forward and backward reaction rates, however, is a necessary condition for chemical equilibrium, though it is not sufficient to explain why equilibrium occurs.

The equilibrium constant for a reaction is indeed a constant, independent of the activities of the various species involved, though it depends on temperature as observed by the van 't Hoff equation. Although the macroscopic equilibrium concentrations are constant in time reactions do occur at the molecular level.

The equilibrium constant can be related to the standard Gibbs energy change for the reaction by the equation

$$\Delta G^0 = -RT \ln K_C \quad (12).$$

where R is the universal gas constant and T the temperature.

When the reactants are dissolved in a medium of high ionic strength the quotient of activity coefficients may be taken to be constant. In that case the concentration quotient K_C,

$$K_C = \frac{[S]^\sigma [T]^\tau}{[A]^\alpha [B]^\beta} \quad (13).$$

where [A] is the concentration of A, etc., is independent of the analytical concentration of the reactants. For this reason, equilibrium constants for solutions are usually determined in media of high ionic strength. Kc varies with ionic strength, temperature and pressure (or volume). Likewise K_C for gases depends on partial pressure.

4.3. Gibbs free energy and equilibrium constant relationship

The relationship between the Gibbs energy and the equilibrium constant can be found by considering chemical potentials μ [60]. Chemical potential is contribution of one mole of one component to the total free energy μ_x. It is also called partial molar Gibbs energy. For the component A the equation is,

$$\mu_A = G_A = \mu_A^0 + RT \ln a_A \tag{14}$$

where μ_A^0 is the standard chemical potential and the a_A is activity of compound A

The extent of reaction ξ approach to solving multiple reaction systems is a general formulation that works for many reaction systems. It is defined

$$\xi = \frac{n_i - n_i^0}{\nu_i} \tag{15}$$

where n_i represents the amount of substance of component in exact time of reaction, n_i^0 is the amount of substance at the beginning of reaction, ν_i is the stechiometric coefficient in the equation of chemical reaction.

In order to meet the thermodynamic condition of equilibrium, the Gibbs energy must be stationary, meaning that the derivative of G with respect to the extent of reaction : ξ, must be zero. It can be shown that in this case, the sum of chemical potentials of the products is equal to the sum of those corresponding to the reactants. Therefore, the sum of the Gibbs energies of the reactants must be the equal to the sum of the Gibbs energies of the products.

$$\alpha\mu_A + \beta\mu_B = \sigma\mu_S + \tau\mu_T \tag{16}$$

Substituting expressions like this into the Gibbs energy equation:

$$dG = Vdp - SdT + \sum_{i=1}^{k} \mu_i dN_i \quad \text{in the case of a closed system} \tag{17}$$

At constant pressure and temperature we obtain:

$$\left(\frac{dG}{d\xi}\right)_{T,p} = \sum_{i=1}^{k} \mu_i \nu_i = \Delta_r G_{T,p} \tag{18}$$

which corresponds to the Gibbs free energy change for the reaction.

This results in:

$$\Delta_r G_{T,p} = \sigma\mu_S + \tau\mu_T - \alpha\mu_A - \beta\mu_B \tag{19}$$

By substituting the chemical potentials:

$$\Delta_r G_{T,p} = \left(\sigma\mu_S^0 + \tau\mu_T^0\right) - \left(\alpha\mu_A^0 + \beta\mu_B^0\right) + \left(\sigma RT \ln[S] + \tau RT \ln[T]\right) - \left(\alpha RT \ln[A] + \beta RT \ln[B]\right) \tag{20}$$

the relationship becomes where *S, T, A* and *B* should be activities or concentration of reaction components:

$$\Delta_r G_{T,p} = \sum_{i=1}^{k} \mu_i^0 \nu_i + RT \ln \frac{[S]^\sigma [T]^\tau}{[A]^\alpha [B]^\beta} \tag{21}$$

$$\sum_{i=1}^{k} \mu_i^0 \nu_i = \Delta_r G^0 \tag{22}$$

which is the standard Gibbs energy change for the reaction – thermodynamics potential. Using van't Hoff isotherm could be calculated possibility of chemical reaction. One of these three cases would be possible:

$\Delta G > 0$	reaction in this direction is not thermodynamically probable
$\Delta G = 0$	equilibrium state
$\Delta G < 0$	reaction in this direction is thermodynamically probable

Reaction will be possible only in case when $\Delta G < 0$, but even if this condition is true reaction would not run because of kinetics resistance of reaction [54].Changes of Gibbs energy are an important thermodynamic condition to assess whether the reaction is possible or not. However, it is not enough to say that the reaction will proceed in the direction of reactants or of products because additional parameters such as pressure or activity of reacting compounds contribute to the overall balance.. It is possible to use the set of criteria [54] to predict if there are possible reactions and which element will be responsible for these reactions,

$$a_R \rangle A_i a_i^{B_i} \qquad (23).$$

where a_R is activity of the element reducted from the ceramics crucible, $a_{\ddot{i}}$ is the activity of a single element of melted alloy and A_i, B_i are constants related to thermodynamic data and stechiometrics rates of reaction.

Even if the reaction would not be possible, we have to take in account the fact that melting of pure metal in oxide crucible is not possible without contamination of alloy by elements of crucible. Reason for this is oxygen pressure equilibrium at the beginning of melting process. There is pure yttrium oxide on the one side and melted Al-Ti alloy on the other so if the activity of yttria in the alloy is very low, the dissociation pressure is very high. Crucible oxide dissociate to yttrium and oxide, both entering to the melt [64].

4.3.1. Addition of reactants or products

Result of complex interactions between the particles of solution may reduce the availability of components for the chemical reaction. It means that the concentration of solution components does not indicate the exact available components for reaction. Effective concentration or activity can be used. Values of component activities are them modified and consist of an actual molecular or ionic concentration and activity coefficient γ [65-66], where

γ = effective concentration / real concentration

If the solution is ideal and pure substance the activity coefficient is one. If the reaction is between gases the "effective pressure" is called gas fugacity f. Gas fugacity coefficient is

analogous with activity coefficient, because any gas is not ideal. Factors that can have an impact on reaction equilibrium are summarized in Table 3

Tab 3: Factors affected reaction equilibrium.

Factor	Equilibrium shift	Equilibrium constant
Decreasing of product concentration or increasing of reactant concentration	In direction of products	No change
Decreasing of reactant concentration or increasing of product concentration	In direction of reactants	No change
Decreasing or increasing of pressure	No change if the volume can be variable	No change
Decreasing or increasing of temperature	Change is depend on Enthalpy	K is changed
Adittion of catalyzator	Any effect	No change

4.3.2. Treatment of activity

The expression for the equilibrium constant can be rewritten as the product of a concentration quotient, Kc and an activity coefficient quotient, Γ.

$$K = \frac{[S]^{\sigma}[T]^{\tau}\ldots}{[A]^{\alpha}[B]^{\beta}\ldots}\frac{\gamma_S^{\sigma}\gamma_T^{\tau}}{\gamma_A^{\alpha}\gamma_B^{\beta}} = K_C\Gamma \qquad (24).$$

4.3.3. Effect of temperature

The effect of changing temperature on an equilibrium constant is given by the van 't Hoff equation. Isochore is derived from a combination of van't Hoff isotherm (14) and the Gibbs-Helmholtz equation (5). Van't Hoff isotherm derivatives based on temperature consequently by adjustments gradually getting van't Hoff equation isochore.

$$\frac{d\ln K}{dT} = \frac{\Delta H^0}{RT^2} \qquad (25).$$

Thus, for exothermic reactions, (ΔH^0 is negative) K decreases with an increase in temperature, but, for endothermic reactions, (ΔH^0 is positive) K increases with an increase in temperature. An alternative formulation is

$$\frac{d\ln K}{d\left(\frac{1}{T}\right)} = -\frac{\Delta H_m^0}{R} \qquad (26).$$

At first sight this appears to offer a means for obtaining the standard molar enthalpy of the reaction by studying the variation of K with temperature. In practice, however, the method

is unreliable because error propagation almost always gives very large errors on the values calculated in this way.

In the temperature limits integrated form is more widely used.

$$\ln\left(\frac{(K_p)_2}{(K_p)_1}\right)=\frac{\Delta H^0}{R}\left(\frac{1}{T_2}-\frac{1}{T_1}\right) \tag{27}$$

$(K_p)_1$ is equilibrium constant of T_1 and $(K_p)_2$ of T_2.

In metallurgical processes we focused on the partial pressure of vapor, depending on the temperature. It also takes into account evaporation of the melt components. Until the saturated vapor pressure, the evaporation of metal continue. The Clausius-Clapeyron equation describes this process.

$$\frac{d(\ln p^0)}{dT}=\frac{L_e}{RT^2} \tag{28}$$

$$\ln p^0=-\frac{L_e}{RT}+const. \tag{29}$$

where L_e is condensing or vaporization heat.

In the temperature limits integrated form of Clausius-Clapeyron, the equation is analogical to the van't Hoff equation

$$\ln\left(\frac{p_2^0}{p_1^0}\right)=-\frac{L_e}{R}\left(\frac{1}{T_1}-\frac{1}{T_2}\right) \tag{30}$$

T_1 boil temperature p_1^0 = 1atm,

Standard free energy diagrams dependent on temperature are used for calculations in chemical metallurgy. They can predict the possibility of reactions and describe a wide range of reactions. The feasibility of reaction is determined by setting the value of Gibbs energy change for reactions (which must be negative) and K (whose value must be sufficiently high). The study of oxide formation using this dependence is shown in the Ellingham diagrams [65-67].

4.5. Dissolution of Y_2O_3 in TiAlNb melt

Dissolution, sometimes called solvatation, is process of mixing molecules of solvent together with molecules or ions of a solutate. Two elemental steps cause the solvatation of solid phase in this case the wall of the ceramic crucible in liquid - melt. The first step is a process on phase interface where the wall of the ceramic crucible is touching and mixing together with melt, very close to the surface of the solid state. This area is called the interspherical area and its thickness depends mainly on diffusion in the case that the liquid state is not moving. The second step is a transport process that is responsible for transfer of dissolved matter from the interspherical area to liquid. One or both of these partial processes

could control the speed of the whole process. The flow of the liquid close to the crucible wall could also be caused by solvatation itself, because there is a difference between densities of instersperical area and melt. In the case the density of liquid closer to the wall is higher than the density of melt itself, movement will be caused by spontaneous flow, also called natural driven density convection [68]. The dissolution of solid state depends mainly on the hydrodynamics conditions of the process, i.e. it depends on the shape of the solid state and the speed of liquid flow.

The shedding of the ceramic crucible wall is caused by dissolving in the melted material touching this wall. This process is called corrosion and because the viscosity of melt is typically very high, this process is very slow. Another situation is on the surface of melted material in the area where the melt, ceramic wall and atmosphere of surroundings are in contact. This is the effect of surface tension of the melt caused by the different concentration of dissolved material on the surface. Corrosion in this area is usually faster, as is demonstrated in Figure 4.

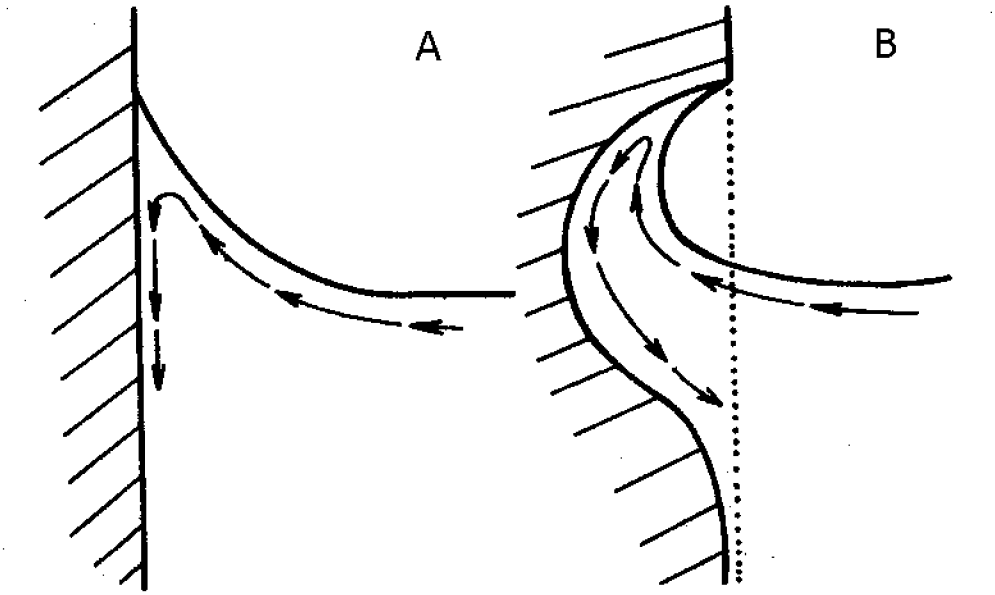

Fig 4: Surface corrosion of crucible wall: A – at the start of melting process, B – after some time [68].

5. Objectives:

Melting of intermetallic compounds is conventionally carried out in induction or arc furnaces with water-cooled copper crucibles. Although, using water-cooled copper crucibles is very efficient in preventing impurities in the melt, this method has low energy efficiency and is expensive for the production of castings. Furthermore achieving a desirable superheat above the liquids in this process is difficult and, due to the low superheat, the melt has insufficient fluidity for filling the entire mold cavity [50]. Another method for melting these materials is using conventional melting and casting processes like VIM. In these processes, ceramic crucibles are used instead of water-cooled copper crucibles [43, 44]. These ceramics should resist in the melting and casting conditions of intermetallic compounds and should not react with them. Reactions between crucible and molten intermetallics will cause the deterioration of crucibles, the contamination of melt and finally, a decrease in the mechanical properties of cast components [50, 69-71]. Thus, melting these compounds in ceramic crucibles requires further investigations in order to reduce production costs and make the technology market-competitive [55].

The main focus of this work is the interactions between TiAl melt and ceramic crucibles, interactions that may lead to contamination of the TiAl alloys. We would like to provide new data on how the melting process depends on melting temperature and melting time. The reaction zone between ceramics and intermetallic melt will be investigated together with the microstructure of the as-cast alloys. A link will be established between the empirically obtained results and thermodynamic calculations. Finally, the reaction mechanisms in the melt-ceramic systems will be described and a level of alloy contamination will be characterized.

Particular objectives are to:

- conduct a series of re-melting VIM experiments with TiAlNb alloy while using Y_2O_3 refractory crucibles (purity 99.99 at. %),
- perform these experiments for different temperatures (1630ºC, 1680 ºC, 1730 ºC) and different melting times (5, 15 and 30 minutes),
- conduct optical and SEM investigation of interfaces between the ceramic crucible wall and solidified alloys,
- analyze microstructures and local concentrations of elements using SEM-EDS
- evaluate the degree of ceramic particle content using ACC image analyzer,
- use the “Fusion of inert gas” method to analyze oxygen content,
- perform thermodynamic calculation for each temperature and each melting time,
- compare the experimental data with the thermodynamic model.

6. Experimental:

Two different TiAl intermetallic alloys have been studied in this work. The melting charges were cut from primary ingots manufactured by FLOWSERVE Corporation (Dayton USA) and GfE Gesellschaft für Elektrometallurgie Metalle und Materialien GmbH (Nürnberg Germany). In what follows, the two material sources are identified as FS (Flowserve) and GfE (Gesellschaft für Elektrometallurgie). The composition specified by the manufactures of the two master alloys is presented in Table 4. The primary ingots were delivered in the form of cylinders of 90mm in diameter and 210-280mm in length.

Tab. 4: Chemical composition of primary ingots (manufacturer data)

FS ingot

Element	Ti	Al	Nb	Cr	Ni	Si	O	C	N	H
wt %	Bal	29.80	15.90	0.70	0.30	0.07	0.08	0.01	0.01	0.0003
at %	Bal	45.80	7.10	0.56	0.21	0.10	0.19	0.03	0.03	0.0120

GfE ingot

Element	Ti	Al	Nb	Cr	Ni	Si	O	C	N	H
wt %	Bal	29.09	15.74	0.91	0.3	0.03	-	-	-	-
at %	Bal	45.81	6.70	0.66	0.18	0.06	-	-	-	-

A Balzers type VSG02 vacuum induction melting furnace was used for melting the TiAlNb intermetallics in a Y_2O_3 ceramic crucible manufactured by Treibacher Industrie AG, Althofen, Austria. The dimensions of the as-delivered crucibles were 55 mm in diameter and 110 mm in height. The following procedure was adopted for each of eleven melting experiments: The crucibles were cut shorter to a height of 80 – 85 mm and were annealed at temperature of 1000 °C of one hour before the VIM experiments in order to remove residual moisture [72, 73]. In the next step, the crucibles were placed in an outer inductor crucible and fixed with corundum sand to ensure a stable position in the inductor. The primary alloy ingot in the shape of a cylinder with a diameter of 36 mm and 70 mm in height was inserted into the crucible. Ingots of the same shape and weight were used for all melting experiments. A small pin of Y_2O_3 with dimensions of 7×7 mm and a 25 mm height was cut out from the cut-off top of the crucible. The pin was built into the bottom of the crucible, and served later as a preferential site for the melt-refractory interaction study. Due to a thermally induces shrinkage the interface between ceramics and intermetallics was better defined at the pin. The furnace was pumped out several times and purged with 99.9% purity argon before the melting trial. The argon pressure was controlled at 1.3×10^4 Pa during the melting experiments [45, 46] to prevent the evaporation of the melted components mainly aluminum. The temperature was kept at the melting temperature (see Table 3). The temperature was measured by the two types of thermocouples. The thermocouple shield was further coated using the Y_2O_3 spay delivered

by ZYP Coatings, Inc. Figure. 5 shows the VIM furnace furnished with the Y_2O_3 crucible and the thermocouple before the meeting experiment. The re-melted alloy was held at the temperature of the experiment for a given hold time and then solidified inside the crucible.

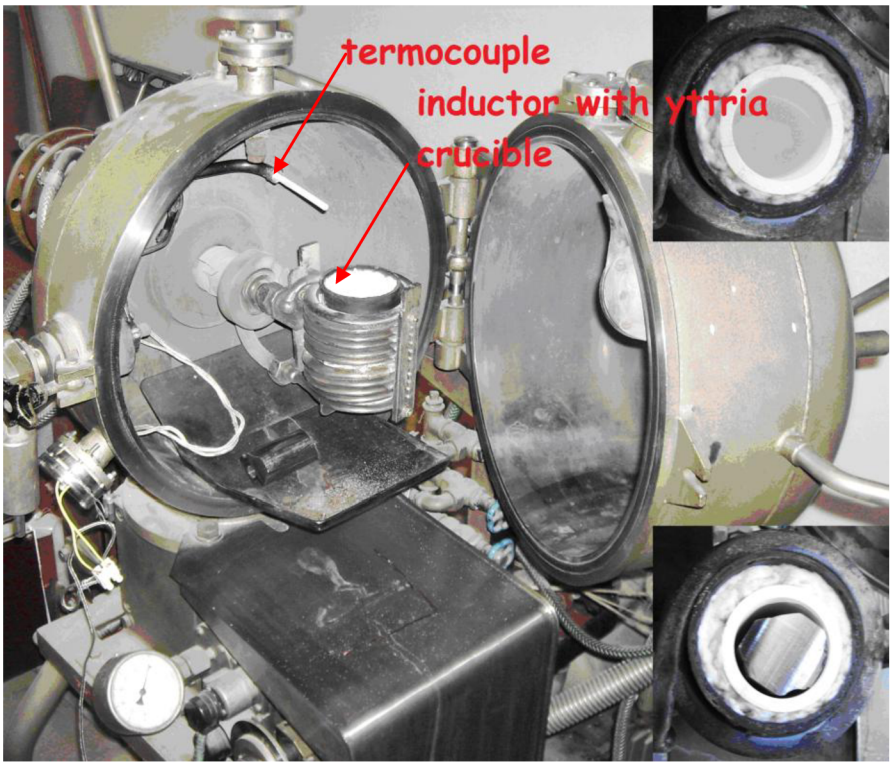

Fig. 5: VIM furnace before the melting trial.

The solidified melt and the crucible were cut in slices perpendicular to the crucible axis as shown in Figure 6. Cutting operations were performed using a ISOMET 5000 saw. Metallographic cross-sections were prepared from one side of the slice. Metallographic samples were first (after cutting) fixed in a polymer resin. Standard grinding and polishing operations using emery paper up to a grid and diamond pastes resulted in the acceptable quality of the cross-sections.

A thin carbon film about 20nm coated the cross-sections in order to improve the contrast of the SEM images take from the composed structure of the insulating ceramics and the conducting intermetallics.

The assessment of the alloy quality and observations of interface between the ceramic crucible and intermetallic alloy were carried out using methods of optical and electron microscopy. Optical microscopy was mainly used as a check of the sample quality before the SEM observations. One of the objectives was the quantitative assessment of ceramic particles and their volume fraction in the as-solidified ingots. Nevertheless, acquired light microscopy images do not have a sufficient contrast for evaluation.

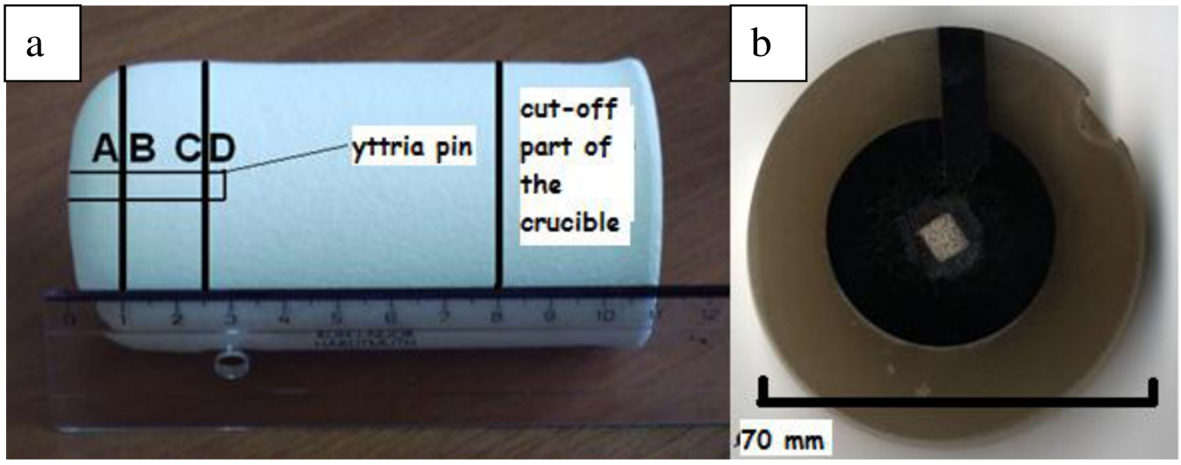

Fig. 6: (a) – Y_2O_3 crucible (cut-off part, ceramics pin) and after melting (cuts A/B,C/D) (b) – metallographic cross section coated by thin carbon layer.

The most important method for observation and elemental analysis of the experimental alloys was scanning electron microscopy (SEM). The best contrast for the evaluation of the ceramic particles was the backscattered electron mode providing very good material contract. Qualitative and quantitative chemical analysis with information was obtained using an energy dispersive x-ray spectrometer (EDS) with the SEM. A special method of TEM sample preparation in the form of thin lamellae for transmission electron microscopy using focused ion beam (FIB) facility was used for selected melts. The following electron microscopes were used for SEM investigations: (i) SEM – JEOL 6460 with EDS, WDS (Wave Dispersive System) and EBSD (Electron Back Scattered Diffraction) from Oxford Instruments (ii) FESEM – Zeiss Leo 1530 Gemini with EDS-EDAX (iii) FESEM – TESCAN Lyra with FIB, GIS (Gas Injection System) and nano-manipulator, SDD-EDS and EBSD system from Oxford Instruments [74-76].

A Philips CM20 –transmission electron microscope was used in order to characterize the microstructure of lamellas prepared on a FIB-SEM microscope. EDS and SA diffraction analysis was performed mainly in the area of the as-solidified melt and the refractory wall.

6.1. ACC (Adaptive contrast control) analyses

Fifty images on average from optical and mainly scanning electron microscopy for each melting experiment were analyzed to determine the content of ceramic particles. An analysis of images was performed using ACC (Adaptive Contrast Control) software by SOFO, which is suitable for the analysis of structures and objects in images. The ACC algorithm can accurately control structures and increase the contrast in the image depending on the size and structure density. The main advantage of this software is that the user does not change the image itself, but another layer covers the image where the structures are marketed according to user preferences. Quantitative measurements are then only a question of calculating what number of pixels has been marketed. Post-processing data analysis show a

great deal of data about the structure of the image, the shape of particles and other information. Figure 7 documents how ACC improves the image contrast before the quantitative assessment [77].

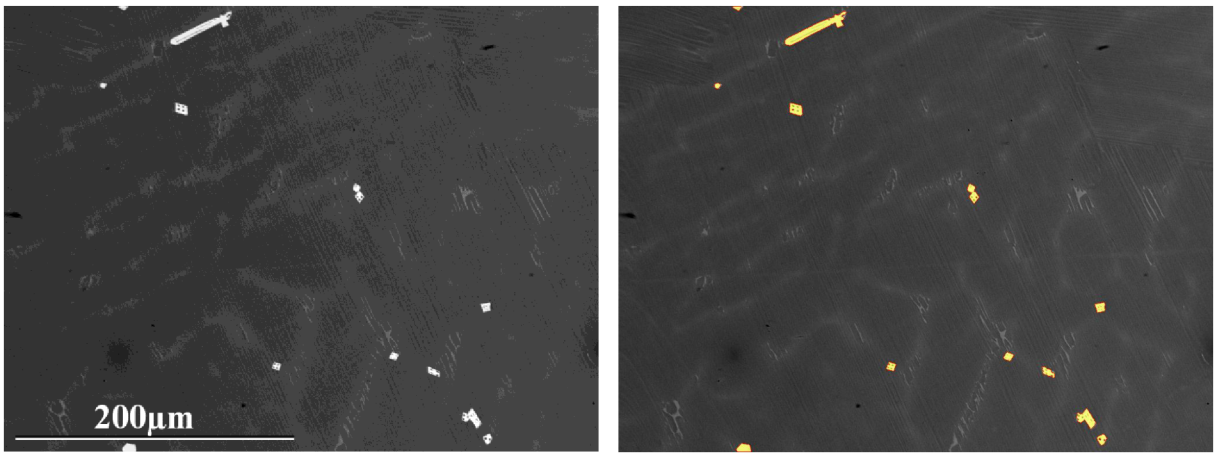

Fig. 7: Typical Example of ACC based image quality improvement (a) – SEM image (b) – marked SEM image

6.2. Oxygen content analyses

Samples for oxygen analysis were cut from the middle part of the re-melted and re-solidified ingots. The oxygen content was investigated using cube samples with an edge dimension of 3 mm. The weight of these cubes was approximately 100 - 150 mg and on average eight cubes were used to assess the oxygen content in one material state. The oxygen content was determined by the Inert Gas Fusion method (IGF). These measurements were performed using an LECO TC436 analyzer available from VUHZ a.s. Dobra.

The schematic block representation of the LECO TC436 system is shown in Figure 8. The IGF analyzer includes an impulse furnace (1) with graphite crucible (2) for receiving the sample (3) in a nickel cage with oxygen containing sample. The furnace includes a supply of a carrier gas. During fusion, the output flow part of the furnace includes conduit leading the product of fusion through a hot copper oxide catalyst (4) operating at the temperature of approximately 650ºC. The product of fusion in the form of (CO) is converted to CO_2. The output conduit of tho catalyst is coupled to a CO_2 infrared detector (5) which detects oxygen in the form of CO_2. The detector provides an output signal to a microprocessor, which calculates the amount to oxygen in a sample. Conduit from the IR detector is coupled to a scrubber (6), which eliminates carbon dioxide from the flow of fusion and sends it to the atmosphere [78].

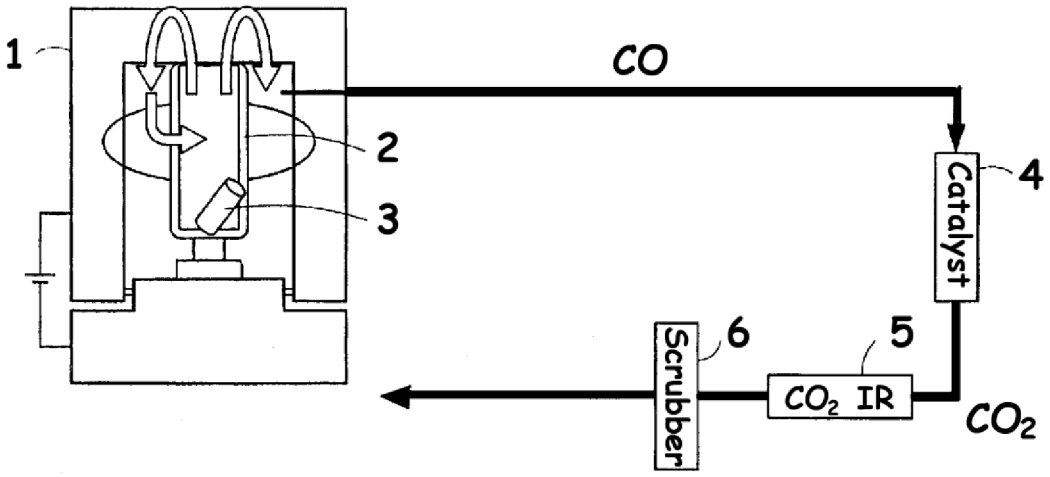

Fig. 8: Scheme of the LECO TC 436 equipment

6.3. Thermocouples

Type B thermocouples use a platinum–rhodium alloy for each conductor. One conductor contains 30% rhodium while the other conductor contains 6% rhodium. These thermocouples are suited for use at up to 1800 °C. Type B thermocouples produce the same output at 0 °C and 42 °C, limiting their use below about 50 °C. Type C (tungsten 5% rhenium – tungsten 26% rhenium) thermocouples are suited for measurements in the 0 °C to 2320 °C range [79]. This thermocouple is well-suited for vacuum furnaces at extremely high temperatures. It must never be used in the presence of oxygen at temperatures above 260 °C. Both types of thermocouples were protected by the Mo-Al_2O_3-ZrO_2 shield [80] further coated using the Y_2O_3 spay delivered by ZYP Coatings, Inc. The main advantage of the C type of thermocouple stems is the possibility of using the same thermocouple for all experiments even for those lasting a long time at a temperature of 1730 °C.

6.4. TEM lamella preparation using SEM-FIB microscope

The preparation of TEM lamellas using high performance scanning electron microscopes is currently a very popular method. A source of focused ions is used for milling the material, and the electron part provides the possibility of observing the process. The main advantage of this method is the choice of sampling area. It is very necessary for sampling deformation bonds, material interfaces and many other examples [81].

In the case of sampling an interface between two phases there could be a problem with the very high difference of milling rates of two different phases and the danger of destroying the sample surface by side ions of FIB. However the protective layer deposition, in most of cases a platinum layer, is used to cover the area of interest. In several steps, the lamella with a thickness around 1μm is prepared to be lifted out. Using the manipulator with a very fine

needle the lamella is lifted out and welded onto the TEM lamella holder. This holder is usually suitable for using in TEM's and could be used for the final thinning and polishing of the lamella. After this step, the thickness of lamella is between 40-300 nm and could be directly used in TEM.

7. Results:

A series of eleven re-melting experiments was performed using the VIM method. The parameters of all the experiments are summarized in Table 5. Two types of primary ingots fabricated by two producers were used as melting charges see also Table 4. A matrix drawn schematically in Figure 9 characterizes the VIM experiments in terms of temperature and melting time. Data related to the milling temperature and time, date of experiment, the thermocouple used for the experiment and the type of primary ingot are summarized in Table 5.

Tab. 5: Summary of VIM experiments

Melt	Date	Init. alloy	Temperature [°C]	Time [s]	Thermocouple type	TEM lamellae
T11	27/5/2010	GfE	1630	300	C	-
T9	2/2/2010	GfE	1630	900	C	-
T10	5/2/2010	GfE	1630	1800	C	-
T5	25/9/2008	GfE	1680	300	B	-
T6	25/3/2009	GfE	1680	300	B	2 pc.
T1	10/10/2007	FLW	1680	900	B	-
T2	7/11/2007	FLW	1680	900	B	-
T3	5/3/2008	FLW	1680	1800	B	-
T4	22/8/2008	FLW	1680	1800	B	-
T7	1/10/2009	GfE	1730	300	C	-
T8	19/11/2009	GfE	1730	900	C	-

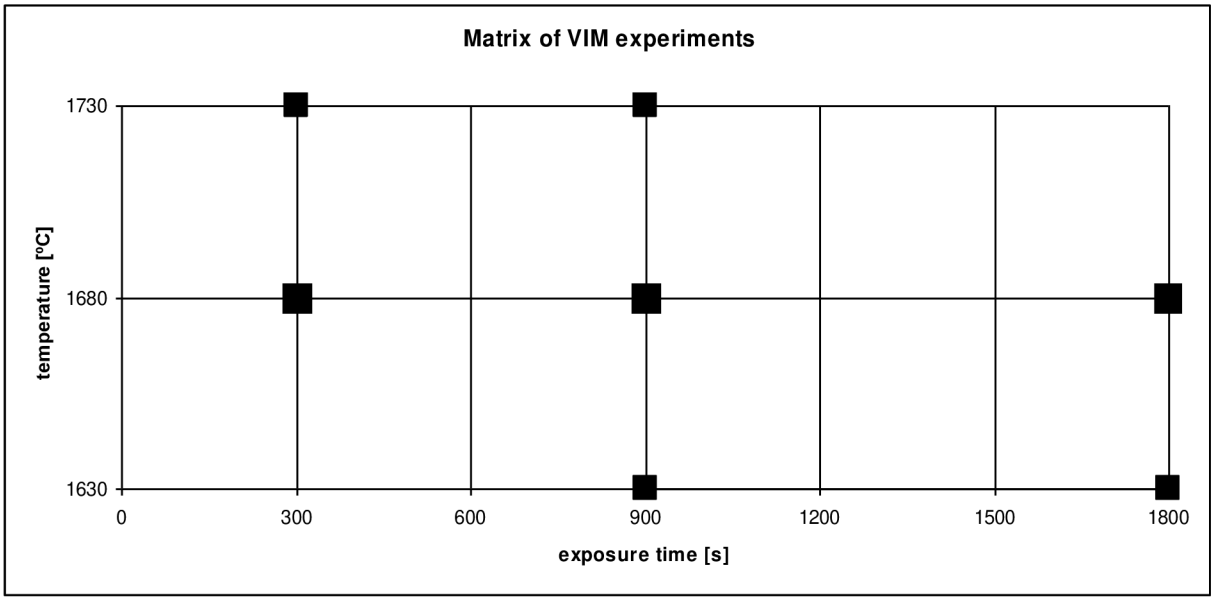

Fig. 9: Matrix of VIM experiments

7.1. Thermodynamics calculations

Interaction melt TiAl – **crucible** Y_2O_3

This chapter focuses on the thermodynamics of reactions between the Y_2O_3 ceramic crucible and the TiAl intermetallic melt. Thermodynamic calculations in this work were carried out under specified conditions of constant pressure and temperature. Calculations were chosen constant - melting temperature and under these conditions, the change in Gibbs energy of reaction corresponding to a given criterion. This leads to the conclusion if system is stable or not.. Data used in thermodynamic calculations have been calculated from the database software HSC Chemistry 5.1 version (Licence: Laboratory of Metallurgy, Department of Materials Science, Helsinki University of Technology) [48]. Direct reactions of melt with yttria are not probable, because the change of Gibbs energy is positive. Using equation based on the standard Gibbs terms, there is no driving force for the formation of corundum, retile or Ti-Al and Ti-Y solutions. Possible partial reactions are summarized in Table 6.

Reactions with both major elements of intermetallic (summarized in Table 7) are not probable because in the investigated temperature range the change of Gibbs energy is positive.

Tab. 6: Standard thermodynamic data for reactions of TiAl with Y_2O_3 refractory [48, 82].

Reaction 1: Y_2O_3**+1.5TiAl→1.5**TiO_2**+1.5Al+2Y**

T (^oC)	ΔH (kJ)	ΔS (J/K)	ΔG (kJ)
1630	644	62	530
1680	636	58	535
1730	632	55	540

Reaction 2: Y_2O_3**+2TiAl→**Al_2O_3**+2Ti+2Y**

T (^oC)	ΔH (kJ)	ΔS (J/K)	ΔG (kJ)
1630	429	21	394
1680	420	16	403
1730	415	14	411

Tab. 7: Partial reactions of melt components with Y_2O_3.

Ti/ Y_2O_3

1.5[Ti]+0.5 Y_2O_3 **→1.5TiO+[Y]**

T (^oC)	ΔH (kJ)	ΔS (J/K)	ΔG (kJ)
1630	159	15	130
1680	156	14	130
1730	155	13	130

1.5[Ti]+ Y_2O_3 **→1.5**TiO_2**+2[Y]**

1630	499	22	457
1680	493	19	457
1730	491	18	457

2[Ti]+ Y_2O_3 →Ti_2O_3+2[Y]			
1630	416	35	350
1680	412	32	350
1730	410	31	350
3[Ti]+ 1.667 Y_2O_3 →Ti_3O_5+3.333[Y]			
1630	763	69	634
1680	754	63	633
1730	751	62	632
Al/ Y_2O_3			
2[Al]+ Y_2O_3→Al_2O_3+2[Y]			
1630	235	-32	296
1680	230	-35	298
1730	228	-36	300

Changes of Gibbs energy are an important thermodynamic condition to assess whether the reaction is possible or not. However, it is not enough to say that the reaction will proceed in the direction of reactants or of products because additional parameters such as equilibrium pressure or activity of reacting compounds contribute to the overall balance. It is possible to use the set of criteria [54] to predict if there are possible reactions and which element will be responsible for these reactions.

If the inequality (23) holds true for all elements of the alloy the reaction with the ceramic wall is not thermodynamically probable on the other hand if the inequality (23) is not fulfilled the reaction is thermodynamically possible for the element with the highest difference of activities.

As it is demonstrated in Figures 10, 11 and 12 the activity of yttria for reactions Y_2O_3+1.5TiAl→1.5TiO_2+1.5Al+2Y and Y_2O_3+2TiAl→Al_2O_3+2Ti+2Y is under given conditions much higher than 1 in the whole range of temperatures and that is the reason why reactions in this systems are not probable. Data presented for the plot were obtained as follows: standard thermodynamic data are summarized in Table 6, Al and Ti activities in TiAl for temperature 1630ºC were taken from literature [45] as were 1680°C and 1730°C [82]. The graphs in Figures 10, 11 and 12 show the activity of yttria in whole range of temperature.

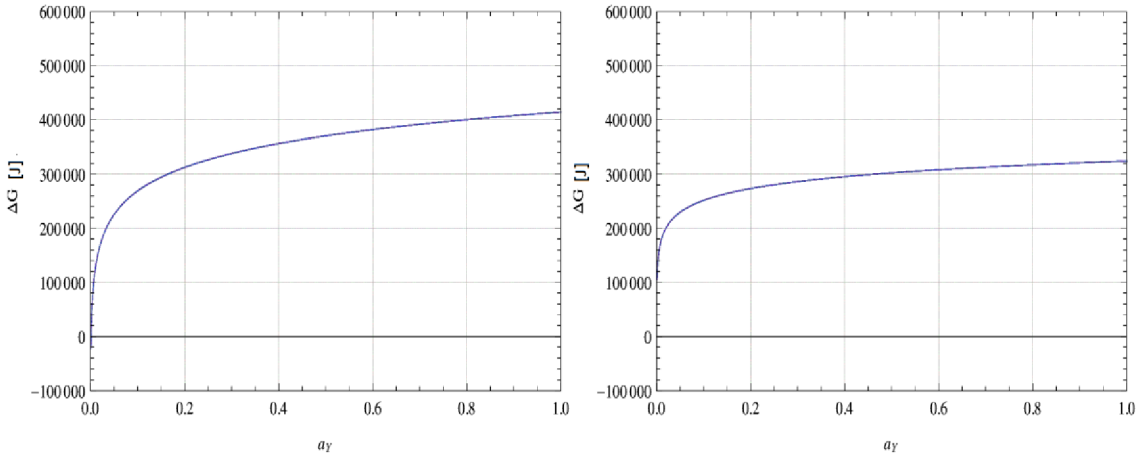

Fig: 10: Activity of Yttria for reactions 1 and 2 in Table 6 - temperature 1630°C

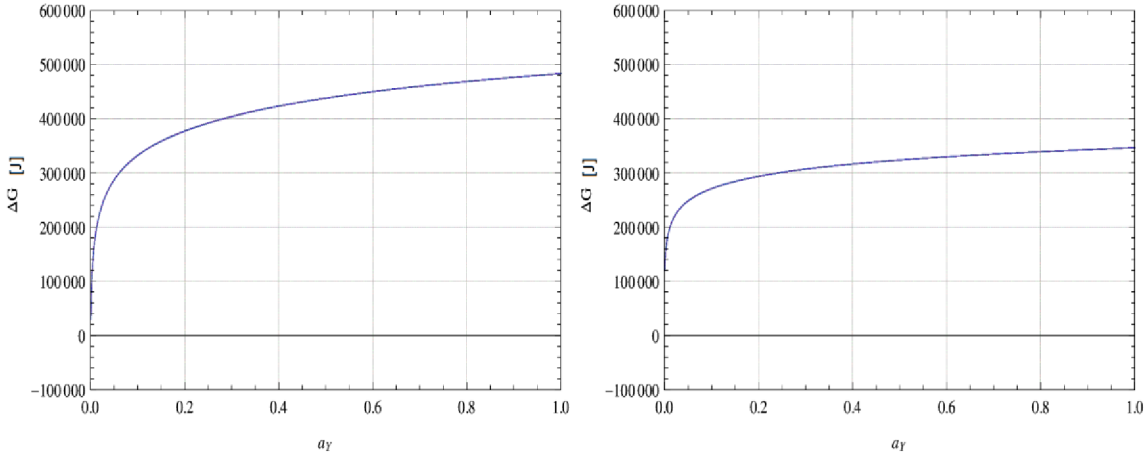

Fig: 11: Activity of Yttria for reactions 1 and 2 in Table 6 - temperature 1680°C

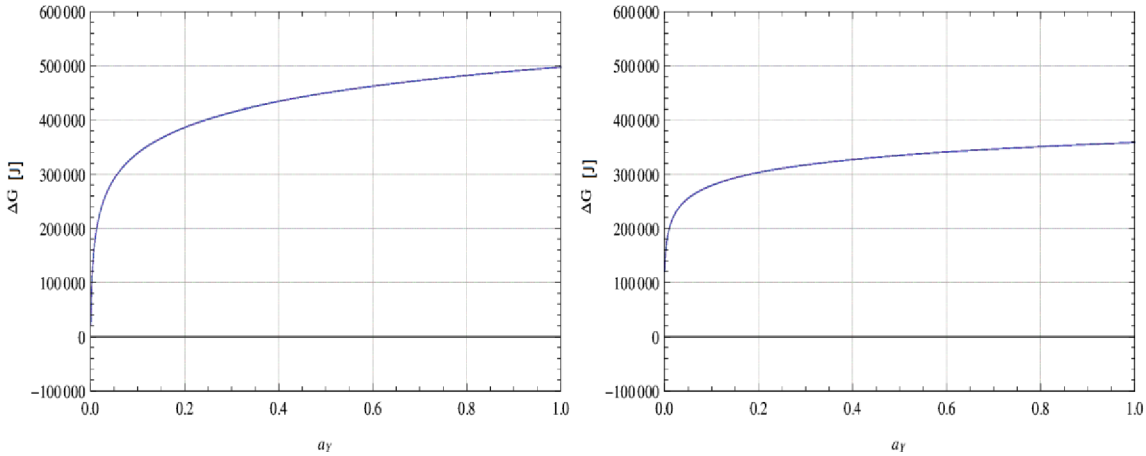

Fig: 12: Activity of Yttria for reactions 1 and 2 in Table 6 - temperature 1730°C

7.2. Experimental results

7.2.1. Y_2O_3 crucibles

A typical microstructure of the Y_2O_3 crucible is documented in the SEM image in Figure 13. Figure 13 also shows locations in which chemical analysis of the crucible composition has been performed using EDS. The results of these analyses are summarized in Tab. 8. These results suggest that small yttria grains that function as a binder material glue together large Y_2O_3 grains with sizes of about 200 μm. Large differences in chemical composition between big solid grains and small connective particles are probably caused by the different absorption coefficients of measured spectra. During the quantification of spectra, factory standards of the EDS system have been used.

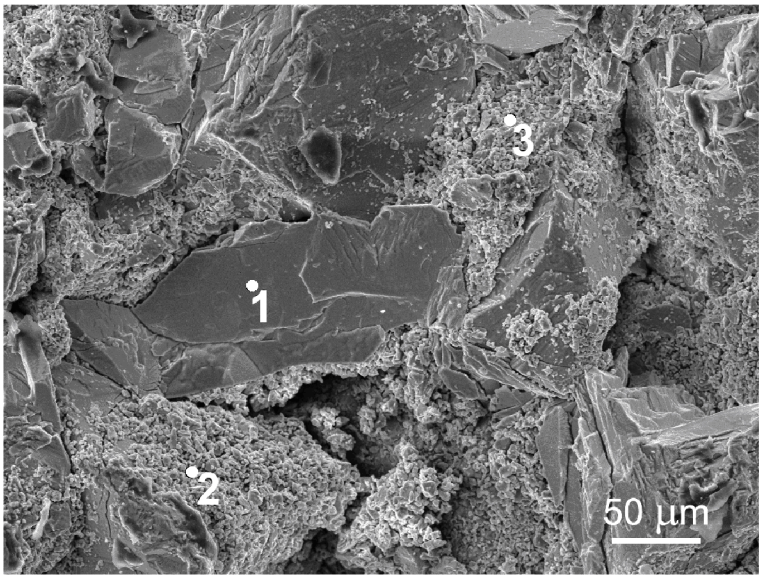

Fig. 13: SEM image documenting a structure of the Y_2O_3 ceramic crucible.

Tab. 8: EDX analyses in locations shown in Figure 13 (at. %)

Element	O	Y
1	73.4	26.6
2	58.7	41.3
3	69.8	30.2

7.2.2. Melting experiments

- **Melt T1**

The melting charge for this experiment was 176.1 g of primary FLW ingot. After reaching the melting temperature at 1680 °C the experiment was successfully ended after a holding time of 1370 s. Temperature variations during the experiment were limited in a range between 1670°C and 1690°C. In this experiment, the thermocouple was left in the position inside the melt after the end of the holding period. This enabled the direct measurement of the

temperature while the remelted material was cooled down to room temperature. The solidification temperature 1558°C was evaluated from the screen plot, because the data acquisition system was corrupted at the same point. A view of the corresponding metallographic cross sections is presented in Figure 14.

SEM observations and analysis

Analytical electron microscopy was used to investigate both sides of the cross-section thought the Y_2O_3 – TiAl interface. The cross-sections are shown in low magnification pictures presented in Figure 15. The results in Table 9 suggest that the Y_2O_3 ceramic grains separated directly from the TiAl alloy. A corresponding magnified view is presented in Figure 16 and Table 10.

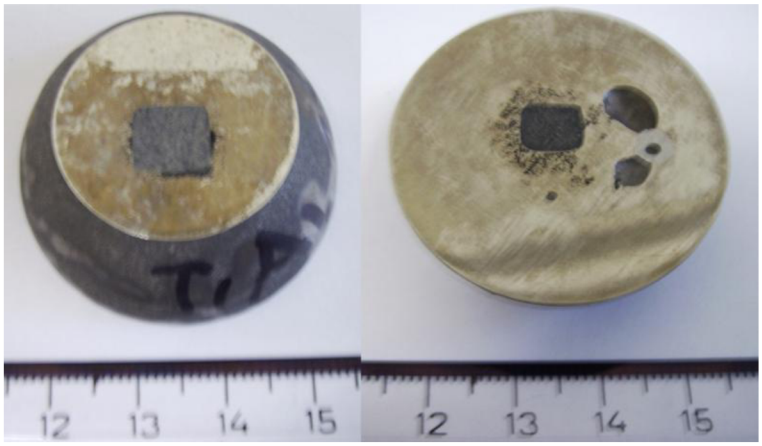

Fig. 14: Images of cross-sections

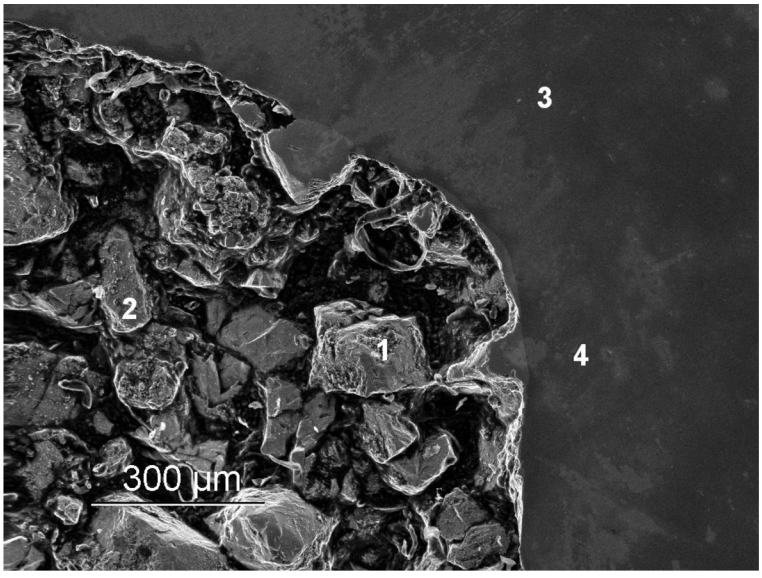

Fig. 15: Overview of the interface with markers indicating positions of the EDS chemical analysis (SEM - SE)

Tab. 9: EDX analyses in locations shown in Figure 15 (at. %)

Element	O	Y	Al	Ti	Nb
1	61.7	38.3			
2	70.4	29.6			
3			44.8	46.8	8.4
4			44.8	47.6	7.4

The high magnification image shown in SEM – SE in Figure 16 documents the sharp interface between TiAl intermetallics and Y_2O_3 refractory. In spite of the fact that the Y_2O_3 refractory grain sticks to the TiAl alloy, there is almost no indications of a chemical reaction between the two phases.

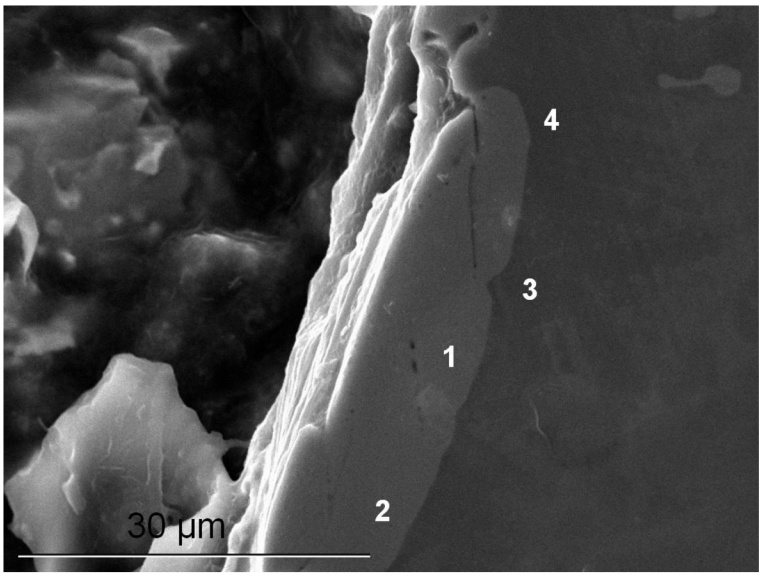

Fig. 16: High magnification (SEM - SE) image of Y_2O_3 grain stuck to the TiAl alloy

Tab. 10: EDX analyses in locations shown in Fig. 16 (at. %)

Element	O	Y	Al	Ti	Nb
1	67.7	32.3			
2	67.0	33.0			
3			45.1	45.2	9.7
4			46.5	43.9	9.6

In the M1 experiment the interface between the alloy and the thermocouple shield was investigated. The thermocouple was left in the alloy during the solidification. Figure 17 shows a detailed view of the interface as well as individual separate phases. The figure suggests that the interface layer has a thickness of approximately 300 µm. However, as can be seen in the bottom right corner of the image, the protective coating of Y_2O_3 significantly affects the

thickness of the layer, which in places where the Y_2O_3 coating did not peel off, only extends over about 50-100 μm. The analyses of phase compositions are summarized in Table 11.

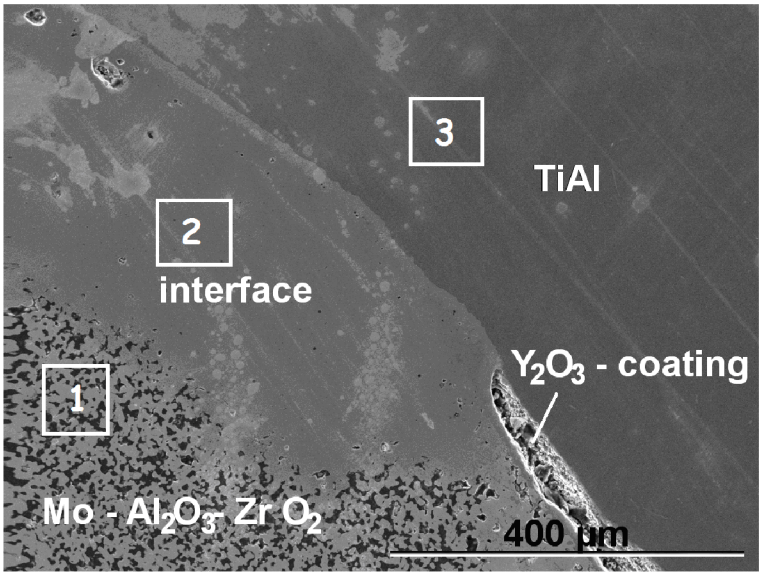

Fig. 17: Overview SEM – SE image of TiAl and Y_2O_3 coated cermet shell interface

Tab. 11: EDX analyses in locations shown in Figure 17 (at. %)

Element	O	Al	Ti	Nb	Mo
1	44.8	7.7	0.0	0.0	43.5
2	63.7	21.5	10.0	0.0	4.8
3	0.0	46.0	47.3	6.7	0.0

- **Melt T2**

The melting charge for this experiment was 272 g of the primary FLW ingot. This experiment was expected to end after 2600 s at the melting temperature. Nevertheless, after reaching the melting temperature at 1680ºC, the experiment was ended after only 1520 s, because the thermocouple was damaged as is shown on the Figure 18. The temperature of the experiment varied in a range from 1670 ºC to 1690 ºC. The holding time at the melting temperature is thus similar to the one accumulated in the experiment T1. Figure 19 clearly shows the difference between the data acquired from the two detectors of the electron microscope. On the left side back scattered electrons are presented while image using the secondary electrons is shown on the right.

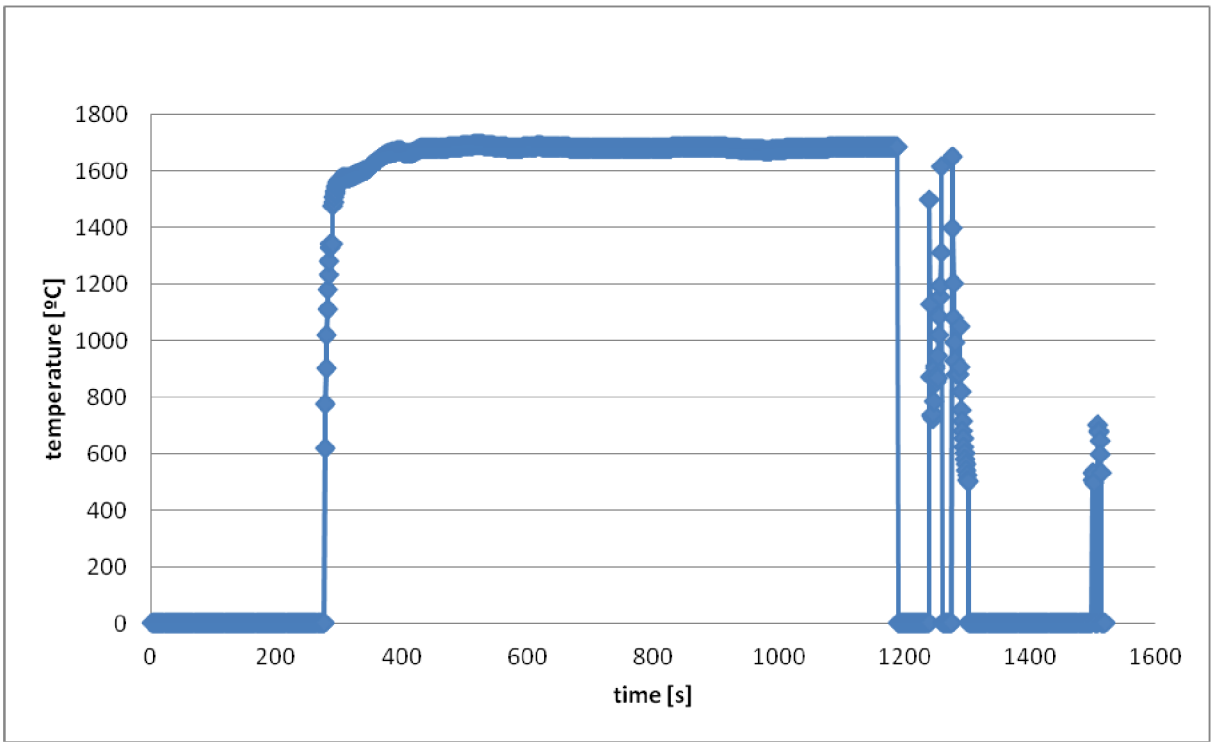

Fig. 18: Time-temperature data recorded for experiment T2

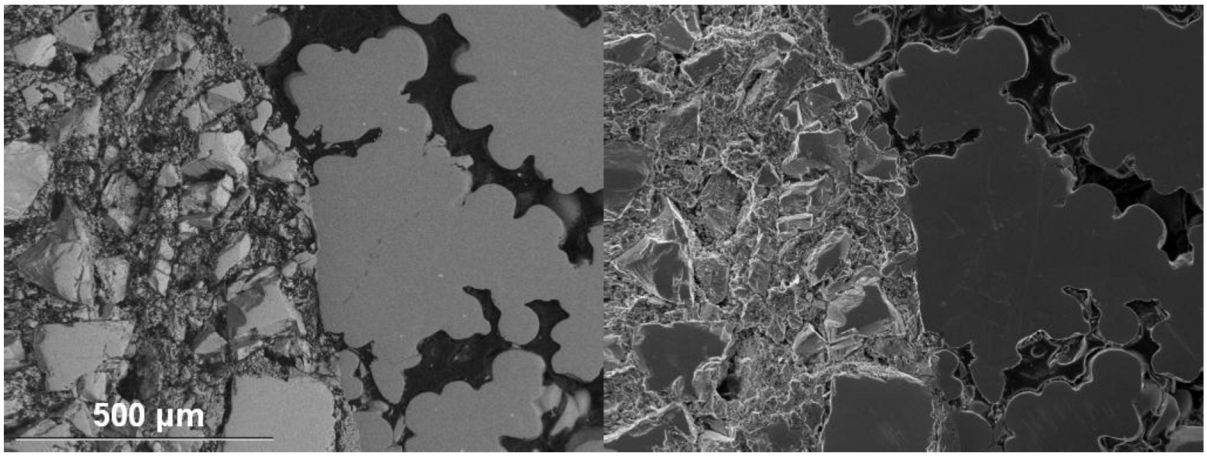

Fig. 19: Comparison of two different SEM imaging modes BSE (on the left) and SE (on the right)

- **Melt T3**

The melting charge for this experiment consumed 258.7 g of the primary FLW ingot. After reaching the temperature of 1680ºC, the experiment was successfully finished after an accumulated time of 2310 s. The temperature of the experiment varied from 1670 ºC to 1690 ºC. However, at the time of 800 s, there was a short excursion to a temperature of 1720°C, for about 30 s. Figure 21 shows that the ceramic pin detached from the bottom of the crucible and molten alloy floated during the experiment.

In this experiment, the thermocouple was left inside the molten intermetallics after the holding period had finished. This enabled the direct measurement of the temperature during the cooling of the re-melted material down to room temperature. The solidification temperature of 1524 °C was evaluated from the recorded data, as is demonstrated in Figure 20.

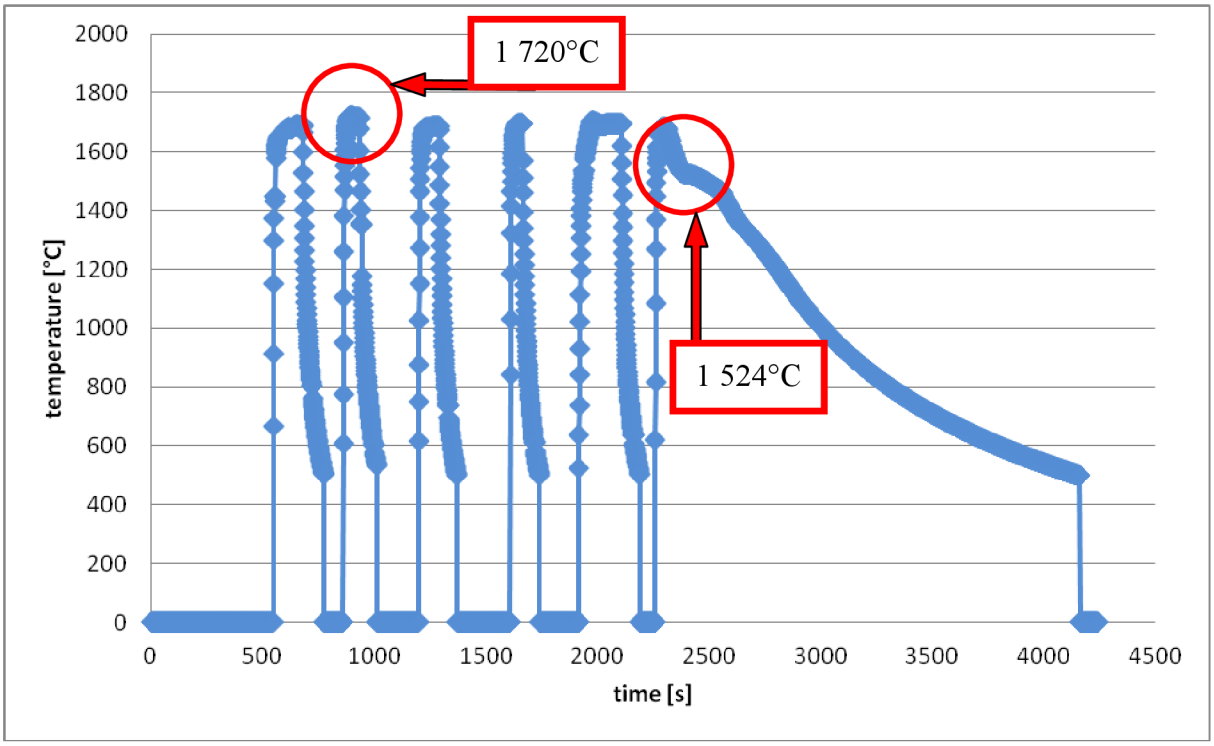

Fig. 20: Time-temperature data recorded for experiment T3.

SEM observations and analysis

Figure 22 presents a low magnification image of metallographic cross-sections investigated by SEM. Y_2O_3 particles are left behind the floating pin. Figure 23 shows a detail of the area and points of EDS analyses. The results of EDS investigations are summarized in Table 12.

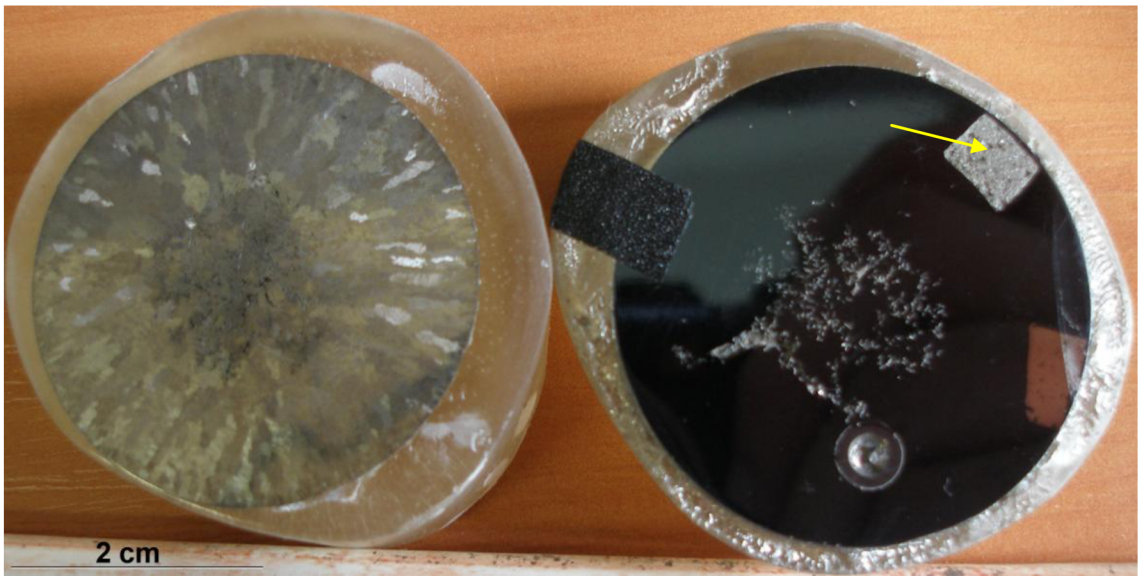

Fig. 21: Overview image of metallographic cross-sections, samples of the melt T3.

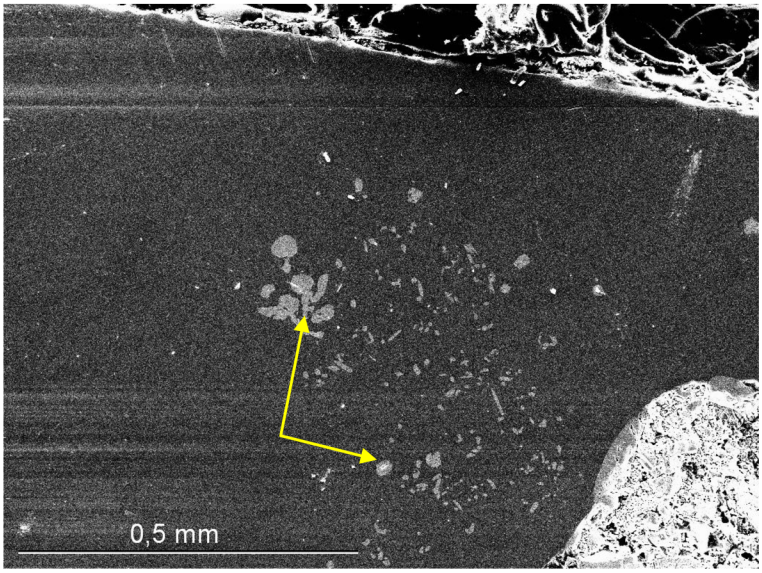

Fig. 22: SEM image of the area around the floating pin.

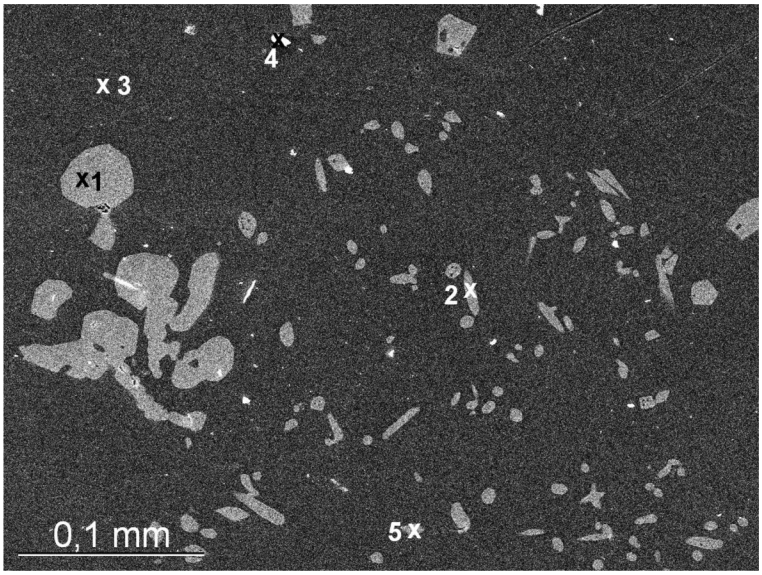

Fig. 23: Ceramic particles in the TiAlNb alloy. The five points indicate positions of the EDS analyses.

Tab. 12: EDX analyses in locations shown in Figure 23 (at. %)

Element	O	Al	Ti	Y	Nb
1	57.9			42.1	
2	54.8	5.3	5.3	34.6	
3		46.2	46.2		7.6
4	45.2	6.5	5.6	42.7	
5	59.3			40.7	

- ## Melt T4

The melting charge for this experiment consumed 260.2 g of the primary FLW ingot. This experiment replaced the trial of T3, the results of which could have been biased due to the Y_2O_3 pin failure. Therefore, in the T4 experiment, no pin was stuck to the crucible bed. In spite of this difference, the experimental results of the T4 trial confirmed the finding of the T3 experiment.

The melt was held at the melting temperature of 1680 ℃ for 2550 s and then the experiment was successfully finished. The Temperature of the experiment varied from 1670 ℃ to 1690 ℃ during the holding period. In order to protect the thermocouple from damage during a long-therm immersion, the temperature of the melt was measured discontinuously in several short-time periods. The measured data are shown in Figure 24.

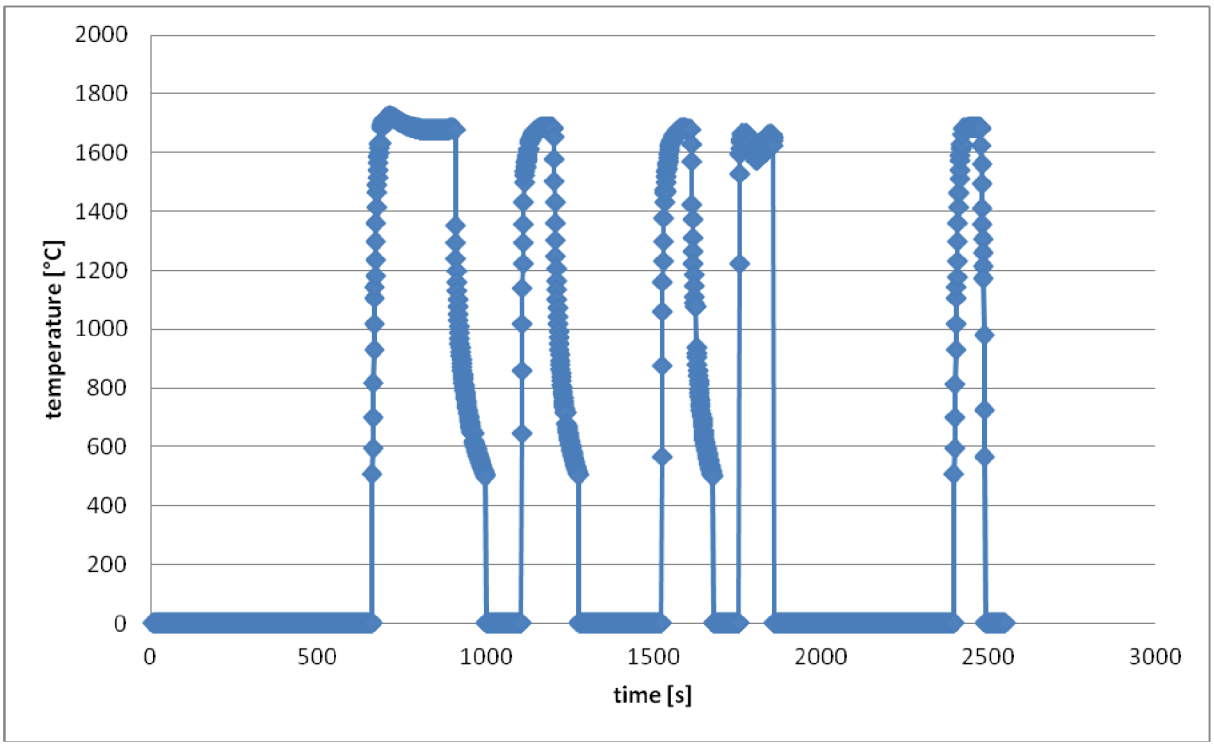

Fig. 24: Time-temperature data recorded for Melt T4 experiment.

SEM observations and analysis

A dendritic structure of TiAlNb intermetallics is shown in Figure 25. The size and shape of Y_2O_3 particles is very different. The size of particles can vary from a few micrometers to hundreds of micrometers. A detailed view of the particle morphology is presented in Figure 26. The corresponding results are summarized in Table 13.

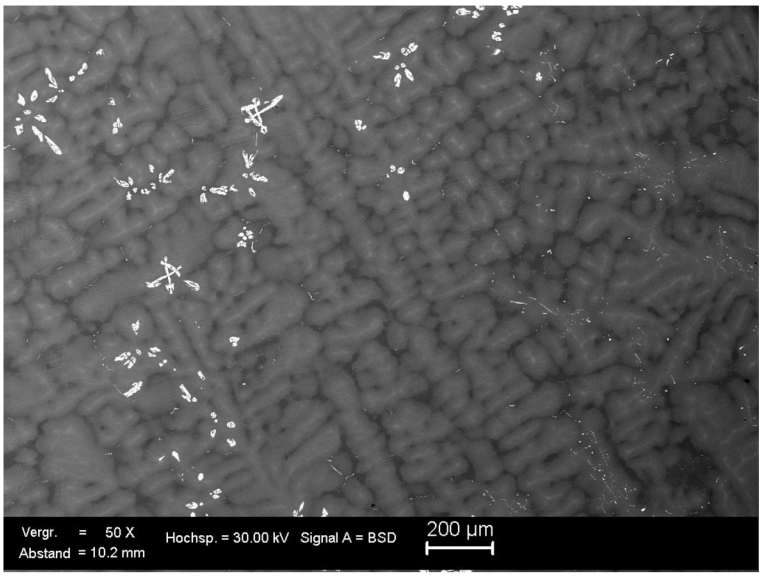

Fig. 25: Review image of TiAl dendritic structure with different sizes of Y_2O_3 grains (BSE)

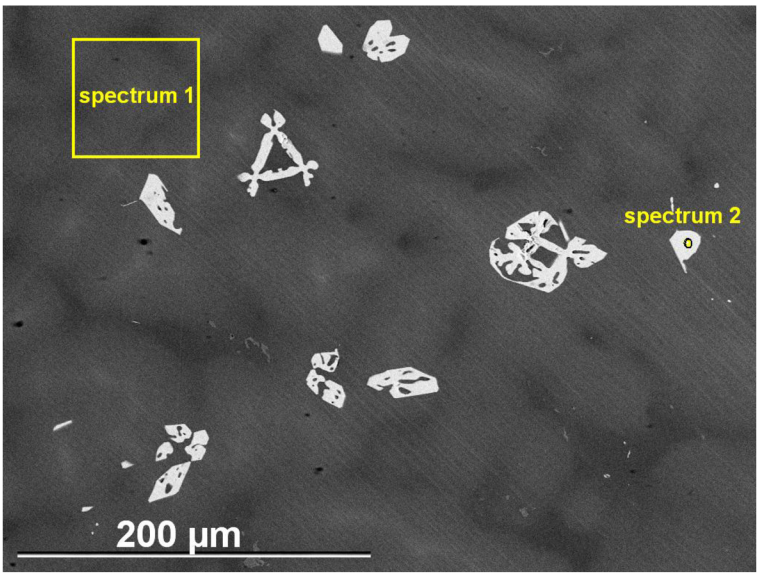

Fig. 26: SEM - BSE image of a TiAlNb re-solidified alloy with two markers that indicate positions of the EDS analyses.

Table 13: EDX analyses in locations shown in Figure 26 (at. %)

Element	O	Al	Ti	Y	Nb
1		48.9	42.4		8.7
2	64.4			35.6	

- **Melt T5**

The melting charge for this experiment consumed 258.7 g of the primary GfE ingot. The melting temperature of 1680 ℃ was kept steady for a holding period of 300 s. After reaching the melting point at 1680 ℃, the experiment was successfully finished at 950 s. The temperature during the experiment varied in a range from 1670 ℃ to 1690 ℃. The temperature in this and further melts was measured continuously using a C type thermocouple, and the corresponding record is shown in Figure 27. An SEM image of typical a microstructure is shown in Figure 28 and results of the several analyses from intermetallics and yttrium oxide are summarized in Table 14.

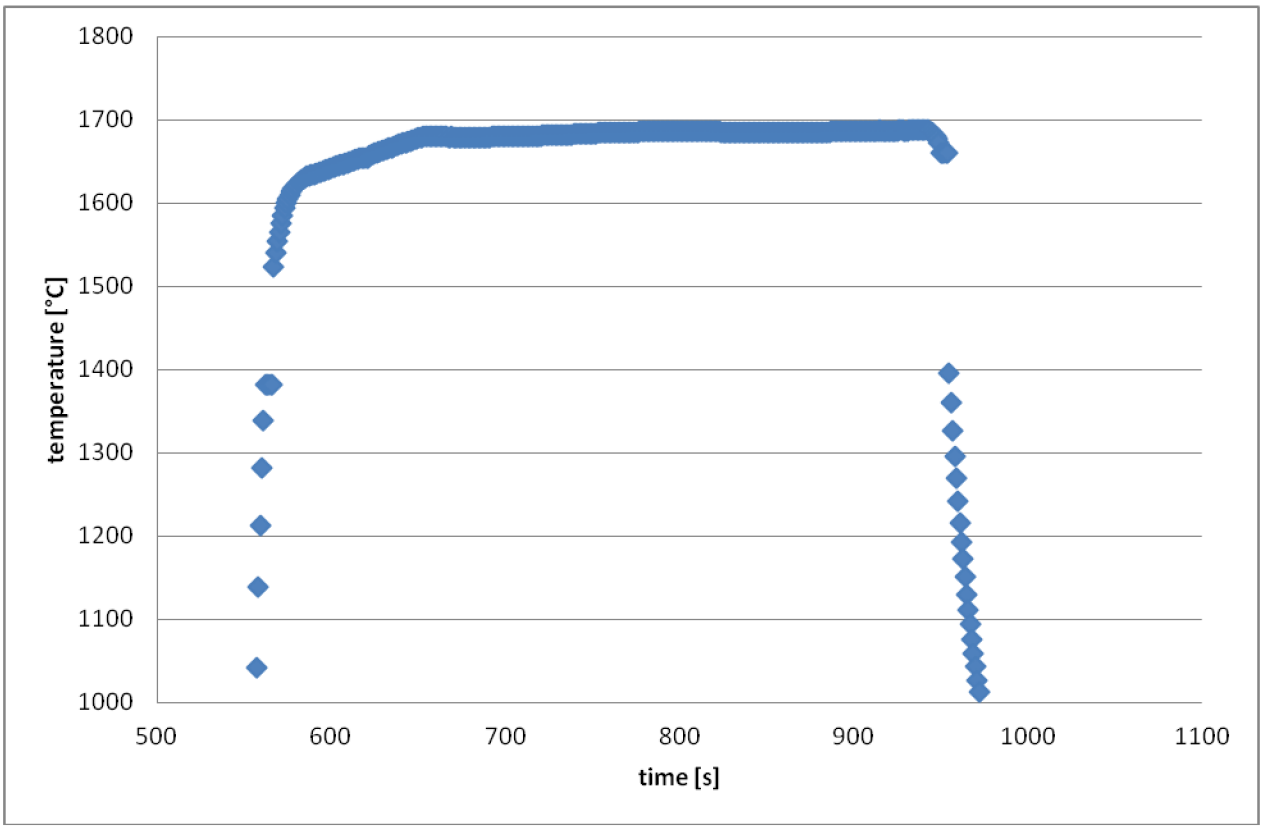

Fig. 27: Time-temperature data recorded for the melting experiment melt T5.

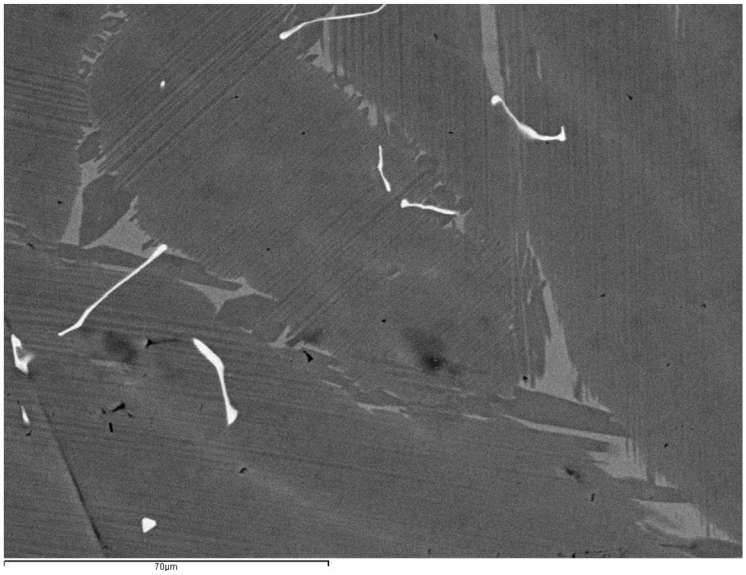

Fig. 28: SEM - BSE image of TiAlNb lamellar structure with α phase region between grains and elongated Y_2O_3 particles.

Tab. 14: Average EDX analyses of Y_2O_3 and TiAlNb from several locations for melt T5 (at. %)

Element	O	Al	Ti	Y	Nb
Intermetallic		47.8	44.4		7.8
Y_2O_3	65.3			34.7	

- **Melt T6**

The melting charge for this experiment represented 239.2 g of the primary GfE ingot. The holding time at the melting temperature of 1680 °C was 300 s. This melting trial was performed without the ceramic pin fixed to the bottom of the crucible.

After reaching the melting temperature at 1680 °C, the experiment lasted for 1095 s after which it was successfully finished. The temperature of the experiment varied in a range from 1670 °C to 1690 °C. The temperature was measured continuously and the corresponding data are recorded in Figure 29.

SEM observations and analysis

Figure 30 provides an overview of the sample after cutting and the preparation of metallographic surfaces. Figure 31 shows a detail of the marked area in Figure 30. Figures 31 and 32 shown as high contamination of alloy by yttrium oxide particles. SEM – EDS analysis confirmed all expected phases and their composition. Only the analysis 2 and 5 presented in Table 16 do not correspond with the composition of basic materials.

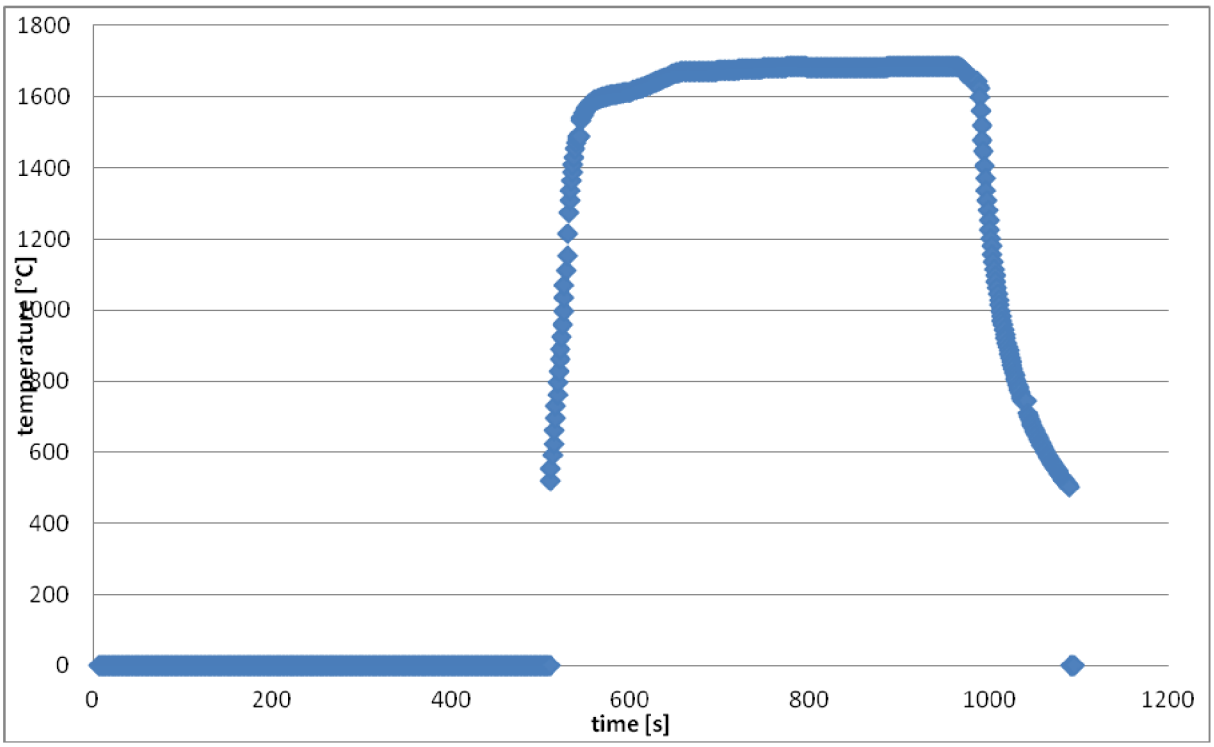

Fig. 29: Time-temperature data recorded for the experiment melt T6.

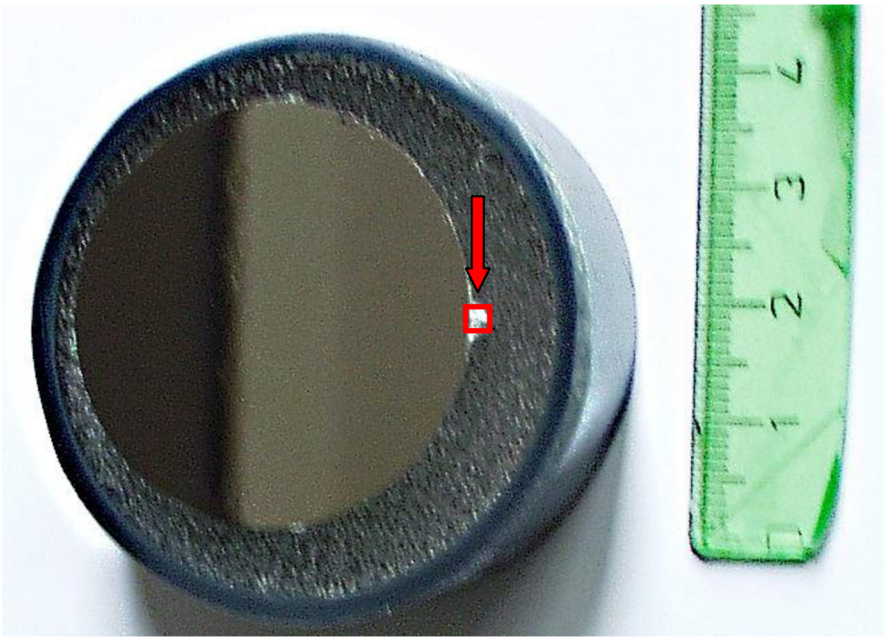

Fig. 30: Overview of the TiAlNb alloy cross-section after melting and re-solidification. The area marked by an arrow indicate a position where the melt penetrated into the crack in the crucible wall.

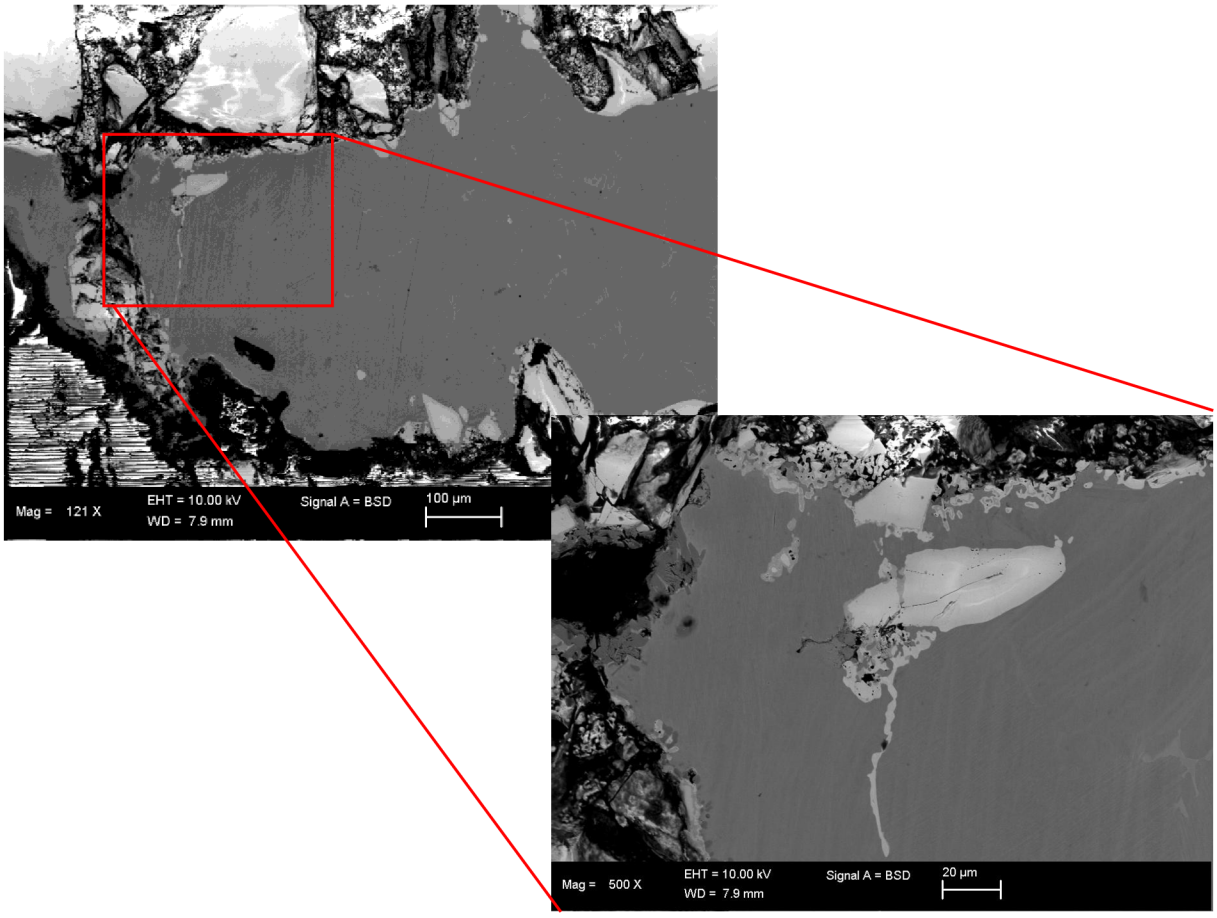

Fig. 31: SEM - BSE image of TiAlNb lamellar structure with α phase between grains and Y_2O_3 particles inside the TiAl solidified melt.

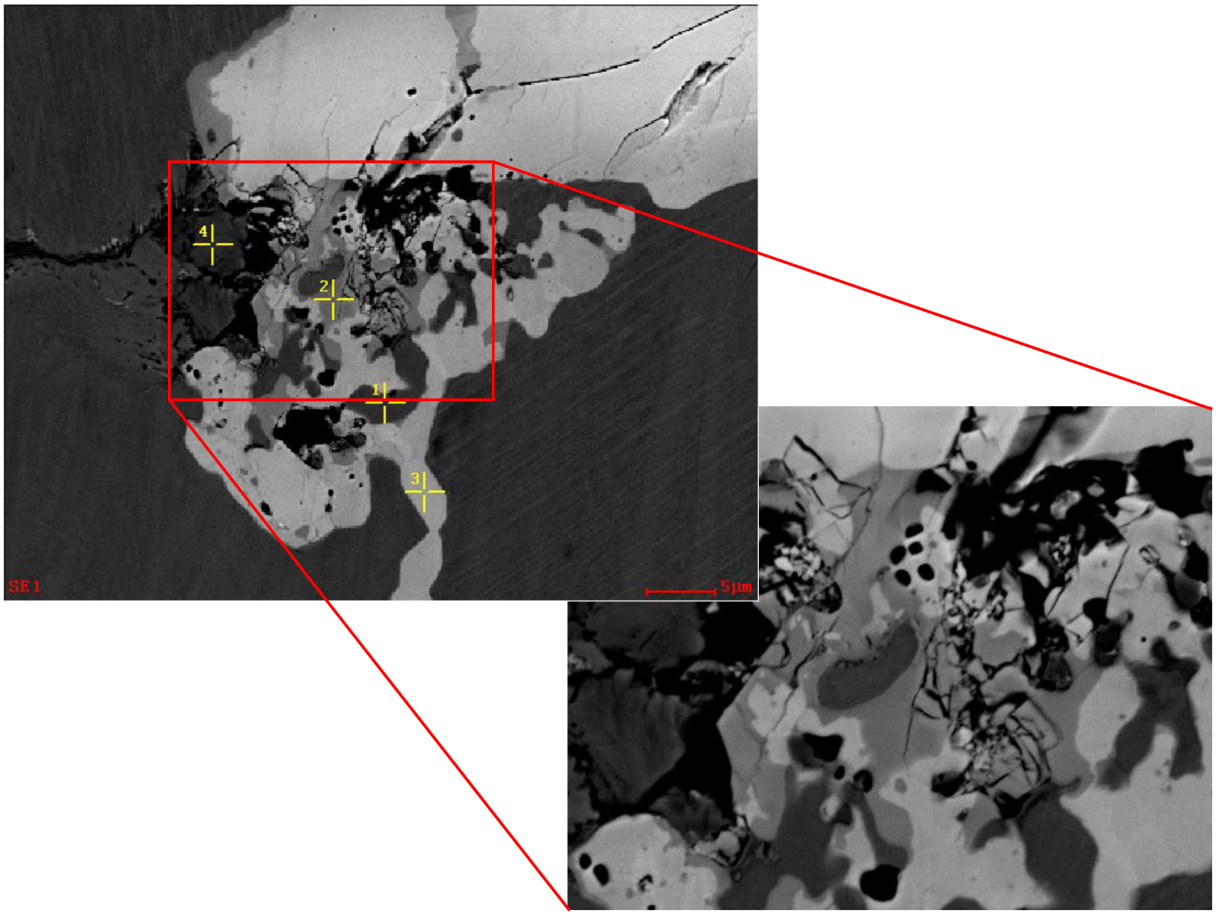

Fig. 32: The detailed microstructure of the process region between TiAlNb alloy and Y_2O_3 ceramics. Points indicate places of the EDS analysis.

Table 15: EDX analyses in locations shown in Figure 32 (at. %)

Element	O	Ni	Al	Y	Nb	Ti	Cr
1	8.6	0.4	36.4	0.0	2.5	52.1	0.2
2	53.2	0.1	18.3	16.4	1.3	10.5	0.2
3	66.8	0.0	0.2	31.5	0.1	0.7	0.7
4	7.6	0.4	35.9	0.0	2.6	53.4	0.1

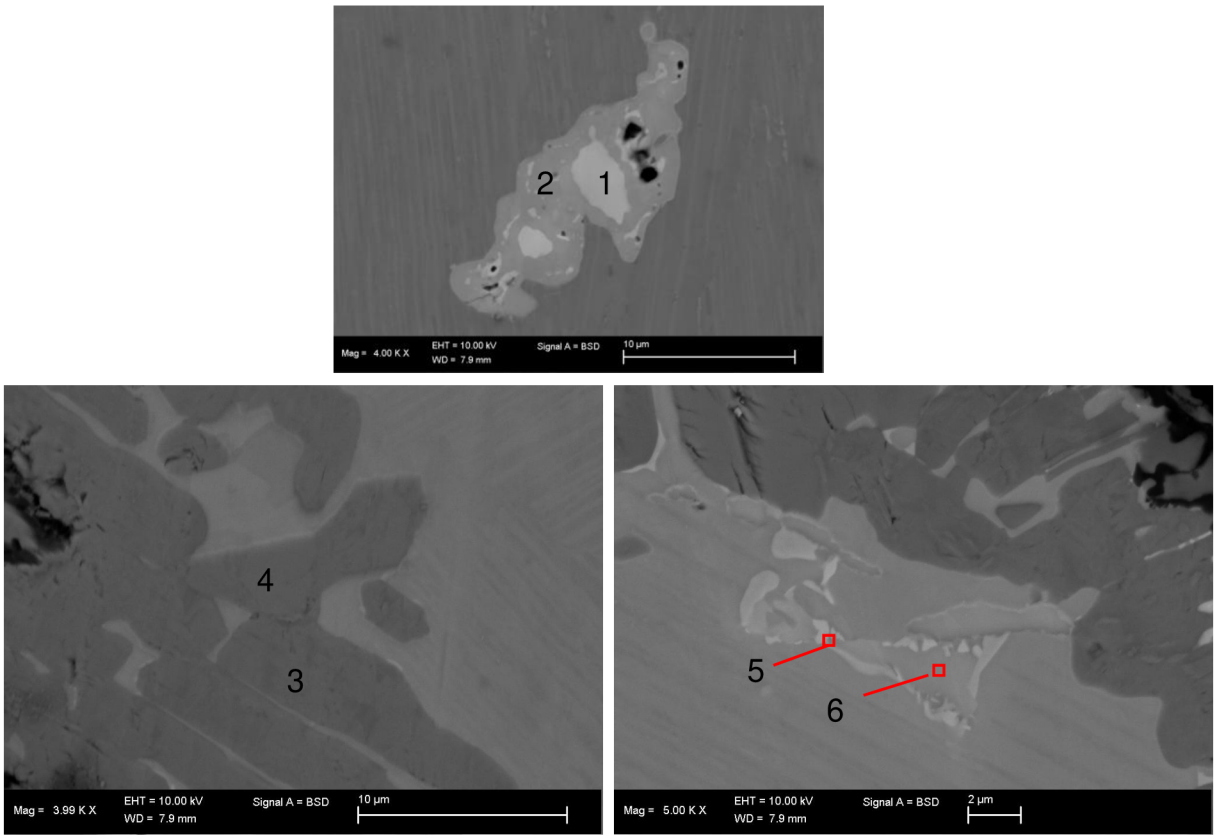

Fig. 33: Detailed image of TiAlNb structure containing complex phases situated in the solidified melt.

Table 16: EDX analyses in locations shown in Fig. 33 (at. %)

Element	O	Ni	Al	Y	Nb	Ti	Cr
1	67.0	0.0	0.3	31.1	0.1	0.9	0.6
2	57.4	0.1	16.9	17.6	1.2	6.5	0.3
3	8.0	0.3	36.6	0.0	2.5	52.4	0.2
4	9.1	0.4	36.1	0.0	2.5	51.7	0.2
5	8.5	13.3	43.2	0.0	14.2	14.3	6.6
6	9.2	0.2	36.0	0.0	15.1	34.2	5.3

- **Melt T7**

The melting charge for this experiment consumed 246.6 g of the primary GfE ingot. The melting temperature of 1730 °C was kept for a holding period of 300 s. This melting trial was performed with the ceramic pin fixed to the bottom of the crucible.

After reaching the melting temperature at 1730 °C the experiment was successfully finished at 870 s. The temperature of the experiment varied between 1725 °C and 1735 °C. The temperature was measured continuously and the corresponding record is shown in Figure 34.

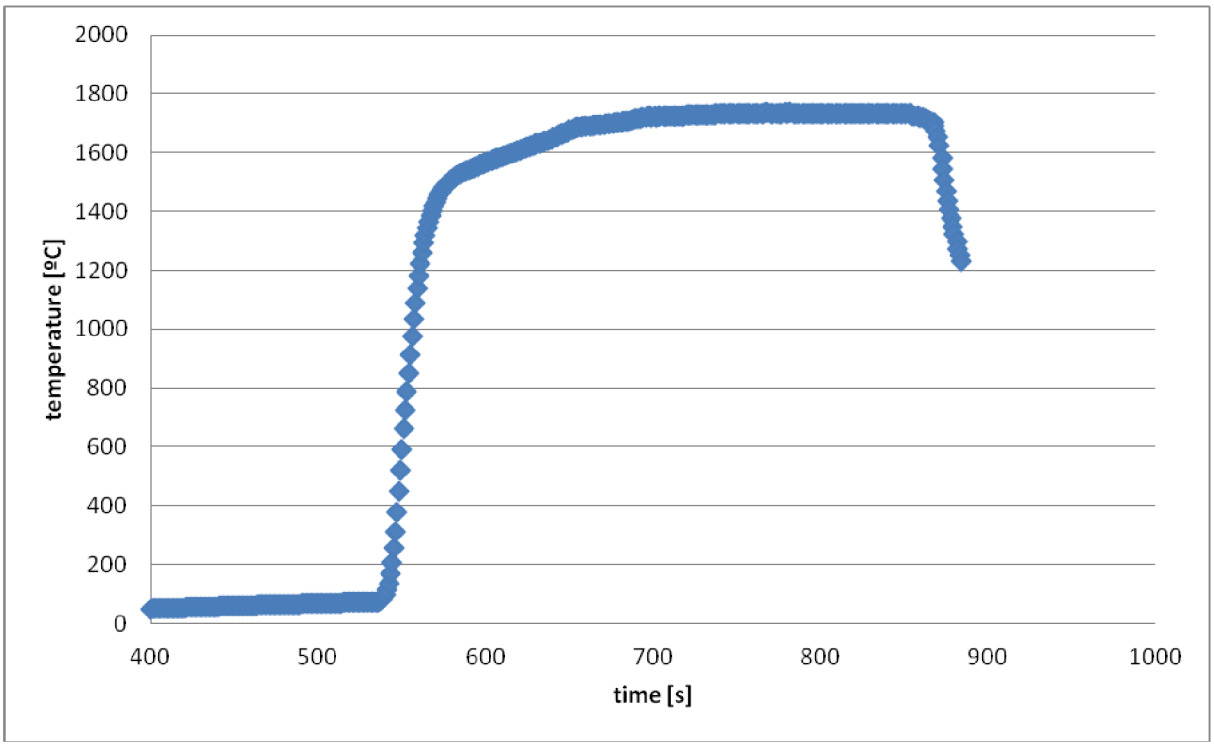

Fig. 34: Time-temperature data recorded for the melting experiment Melt T7.

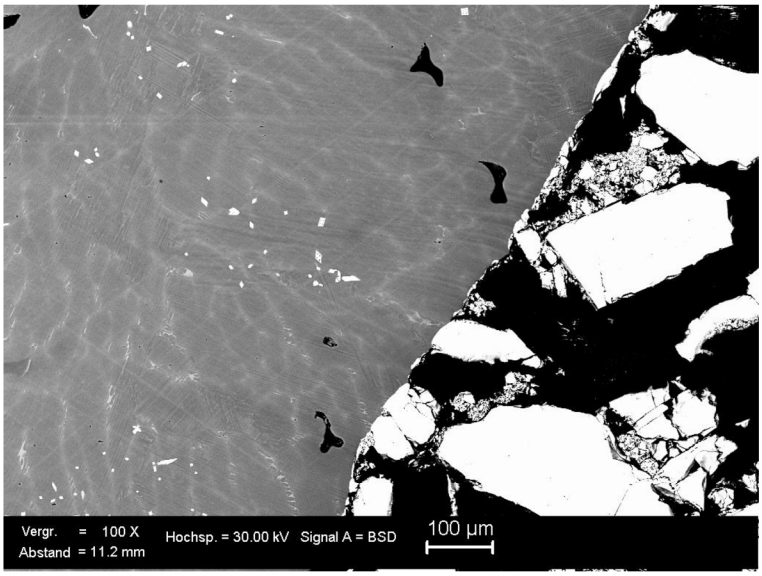

Fig. 35: Overview SEM - BSE image of TiAlNb lamellar structure contains Y_2O_3 ceramics particles and α phase between grains.

SEM observations and analysis

An overview image of the TiAlNb – Y_2O_3 interface is presented in Figure 35. A lamellar structure of TiAlNb intermetallics is shown in Figure 36. The size and shape of Y_2O_3 particles is very different. The size of particles can vary from a few micrometers to hundreds of micrometers and bigger sharp grains have a porous structure. A detailed view of the

particles morphology is presented in Figure 36. Corresponding EDS results are summarized in Table 17.

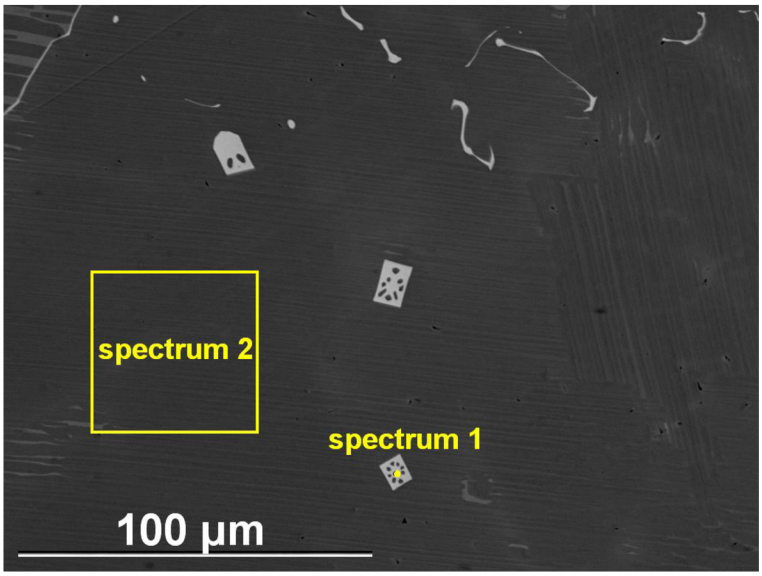

Fig. 36: SEM - BSE image of a TiAlNb with marked areas of EDS analyses.

Tab. 17: EDX analyses in locations shown in Fig. 36 (at. %)

Element	O	Al	Ti	Y	Nb	Cr
1	54.2			45.8		
2		45.4	45.8		8.2	0.6

- ## Melt T8

The melting charge for this experiment was prepared as 259.1 g the primary GfE ingot. The holding time of the alloy at the temperature 1730 ºC was 900 s. This melting trial was performed with the ceramic pin fixed on the bottom of the crucible.

The required melting temperature of 1730 ºC was slightly exceed and a part of the experiment was performed at the temperature of 1750 ºC. A red arrow in Figure 37 marks these fluctuations. The melting temperature was stabilized at 1730 ºC after about 60 seconds. The experiment was successfully finished at 1900s. The temperature of the experiment varied between 1725 ºC and 1750 ºC. The temperature was measured continuously and recorded data are shown in Figure 37.

SEM observations and analysis

Figure 38 presents an image of the structure of TiAl intermetallics near the Y_2O_3 ceramic wall after re-melting experiment T8. Large yttrium oxide particles around 50 µm can be observed inside the solidified alloy Smaller elongated particles Y_2O_3 are also evident in the structure of sample T8. Some shrinkage porosity was also observed in Figure 38. Average EDS results are summarized in Table 18.

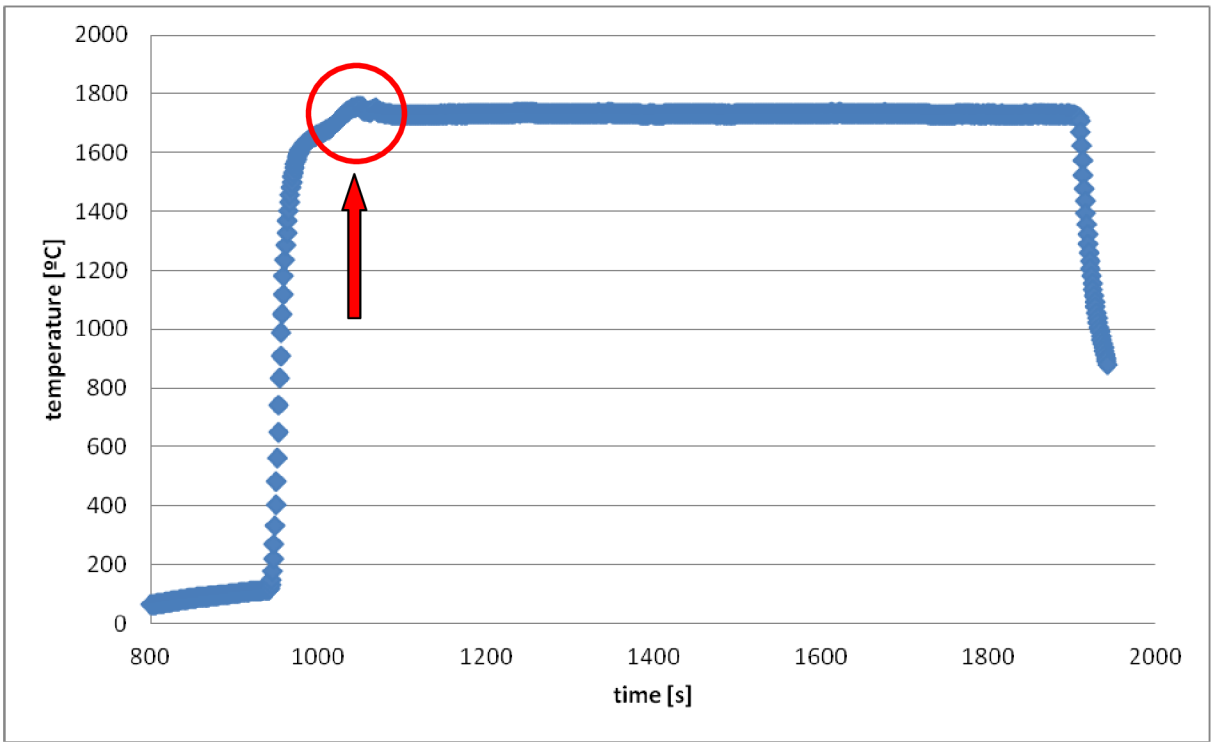

Fig. 37: Time-temperature data recorded for the melting experiment melt T8.

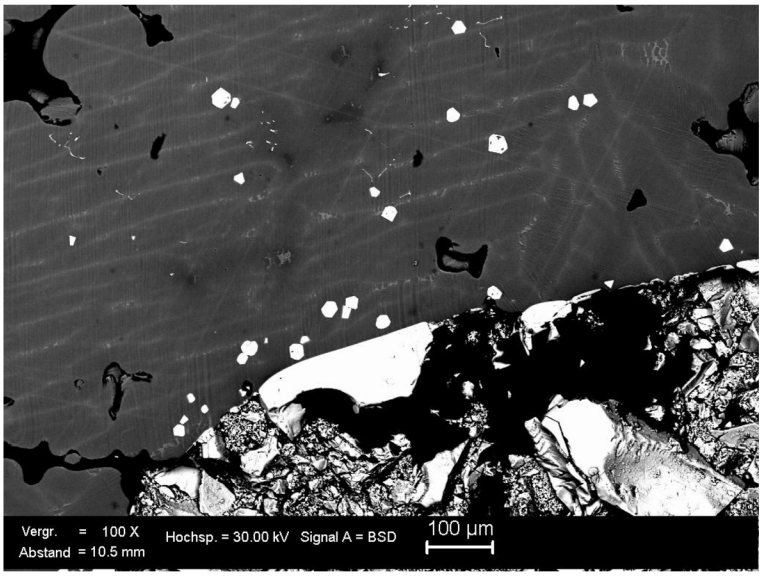

Fig. 38: Overview SEM - BSE image of interface between TiAlNb solidified alloy and Y_2O_3 ceramics rod. White Y_2O_3 particles and α phase between grains are visible.

Table 18: Average EDX analyses from selected places after re-melting experiment T8 (at. %)

Element	O	Al	Ti	Y	Nb
Intermetallic		47.5	44.6		7.9
Y_2O_3	66.3			33.7	

- **Melt T9**

The melting charge for this experiment consumed 247.1 g of the GfE alloy primary ingot. The melting temperature of 1630 °C was kept approximately constant for a holding period of 900 s. This melting trial was performed with the ceramic pin fixed to the bottom of the crucible.

The temperature of the finished experiment varied between 1600 °C and 1635 °C. The remelting trial was successfully finished at 1880 s. The temperature was measured continuously and the corresponding record is shown in Figure 39. After reaching the melting point at 1630 °C the experiment ran smoothly up to the holding time of 1265 s when we had encountered problems with the instability of the furnace power supply, as is shown in Figure 39 four temperature decrements of about 30 °C were recorded.

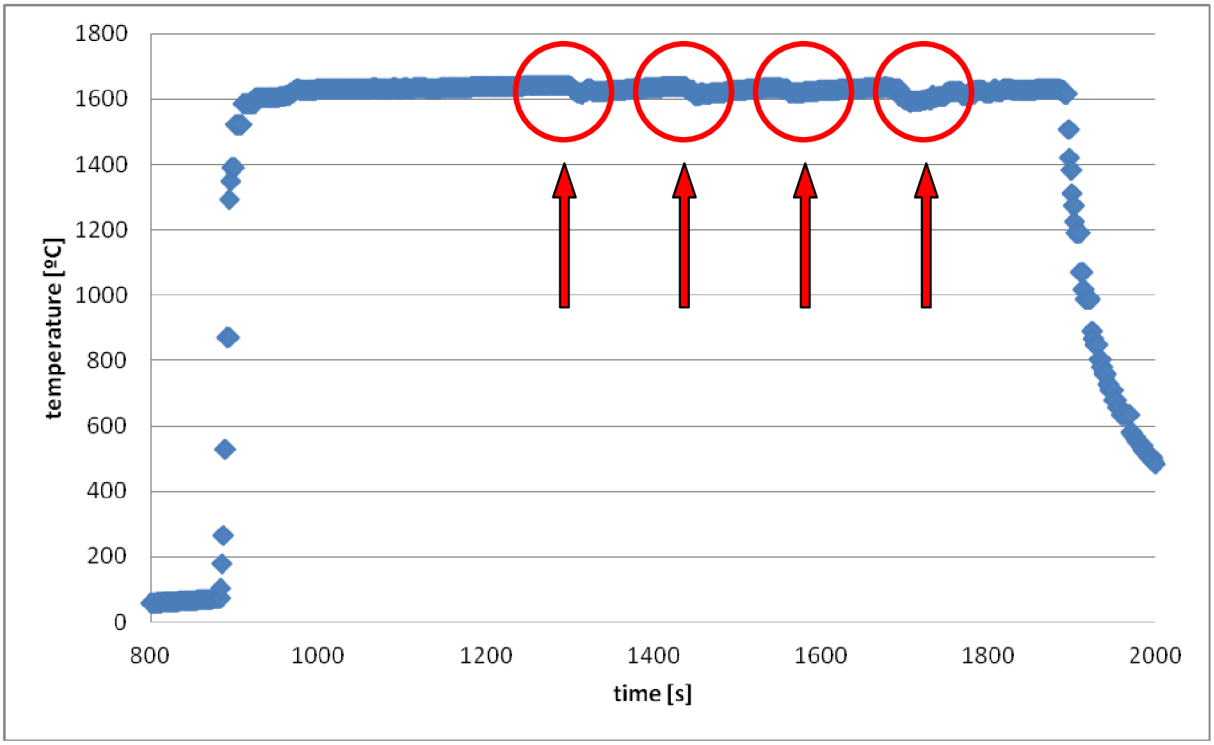

Fig. 30: Time-temperature data recorded for the melting experiment Melt T9.

SEM observations and analysis

Figure 40 shows the microstructure of TiAlNb intermetallics close to the Y_2O_3 ceramic wall. Contamination of the alloy by very small yttrium oxide particles can be observed in Figure 40. The cross-section reveals few places with small holes porosity composed during the solidification of the melt. A detailed image of the microstructure is shown in Figure 41. The dendritic structure with small yttria particles was confirmed by EDS analysis. The results of this analysis are summarized in Table 19.

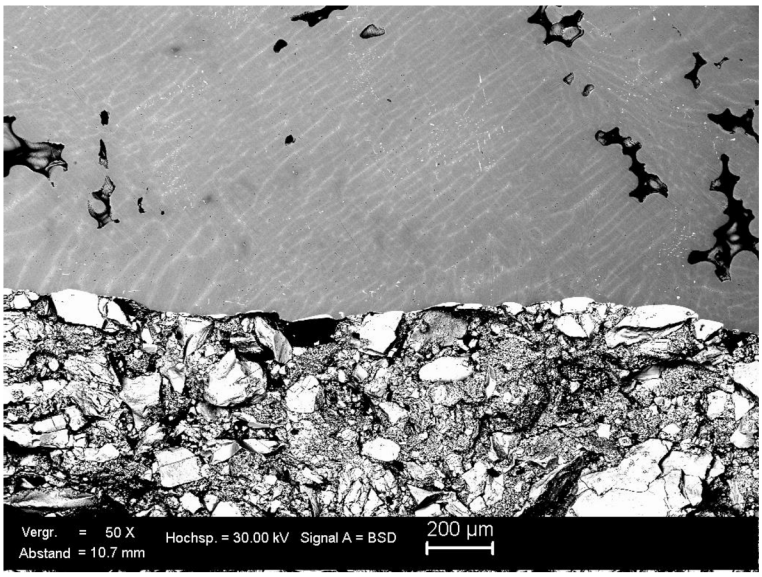

Fig. 40: Overview SEM - BSE image of TiAlNb and Y_2O_3 interface.

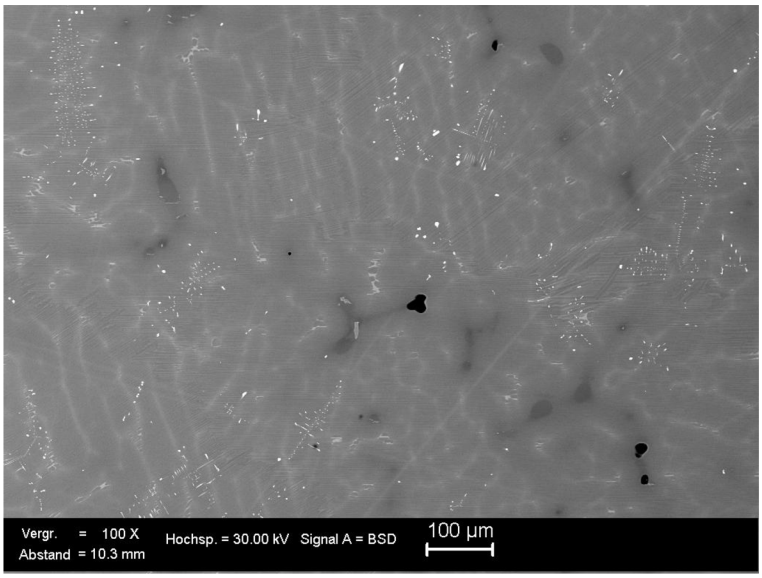

Fig. 41: Detailed image of the microstructure of experiment melt T9, with marked places of EDS analysis.

Table 19: Average EDX analyses from selected places after re-melting experiment T9 (at. %)

Element	O	Al	Ti	Y	Nb
Intermetallic		46.5	45.8		7.7
Y_2O_3	66.7			33.3	

- ## Melt T10

The melting charge for this experiment was prepared as 266.3 g of the primary GfE ingot. The overheat period of the alloy at the temperature of 1680 °C was 300 s. This melting trial was performed with the ceramic pin fixed on the bottom of the crucible.

After reaching the melting temperature at 1680 °C, the experiment was successfully finished at 950 s. The temperature of the experiment varied between 1670 °C and 1690 °C. Te

small crack in the ceramics wall shown in Figure 42 was filled with melted intermetallics as it is documented in the cross-section. This specific area was investigated using SEM and EDS. The temperature was measured continuously and the corresponding record is shown in Figure 44.

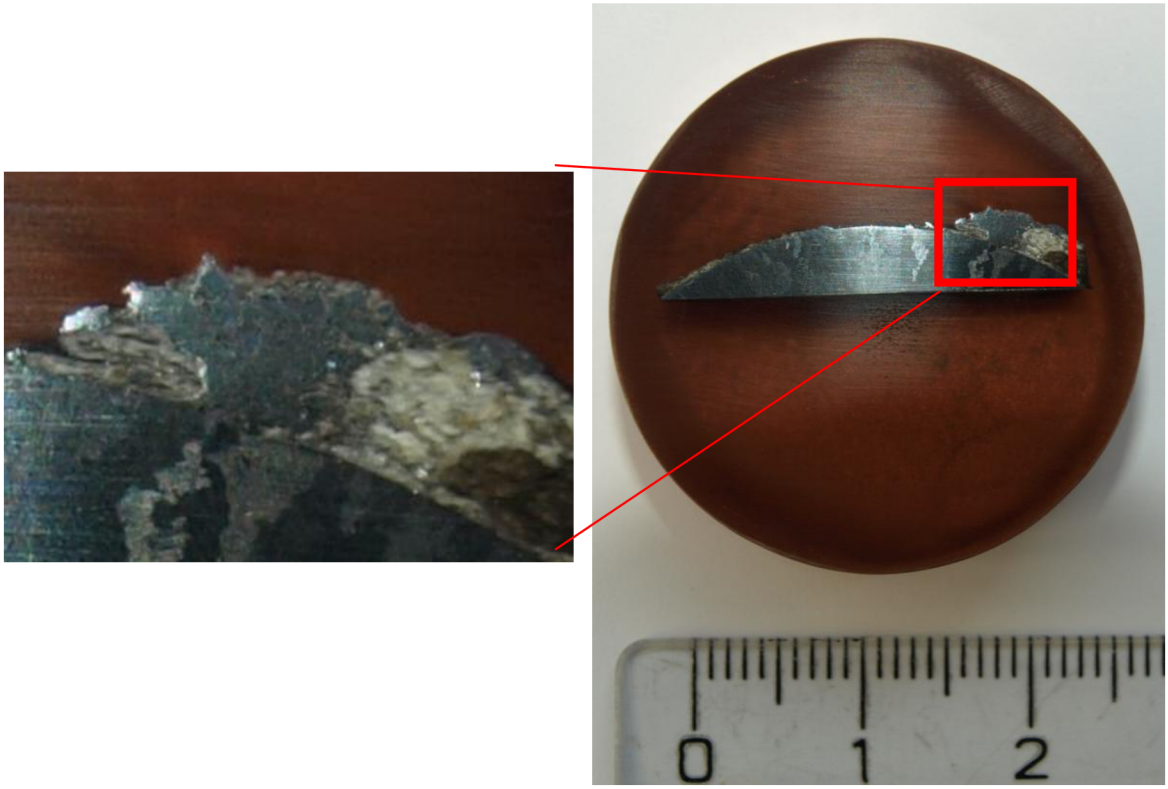

Fig. 42: Overview of the small piece of the TiAlNb alloy with a part of the crucible wall attached after melting and re-solidification. The area marked by a red rectangle indicates a position where the melt penetrated into the crack in the crucible wall.

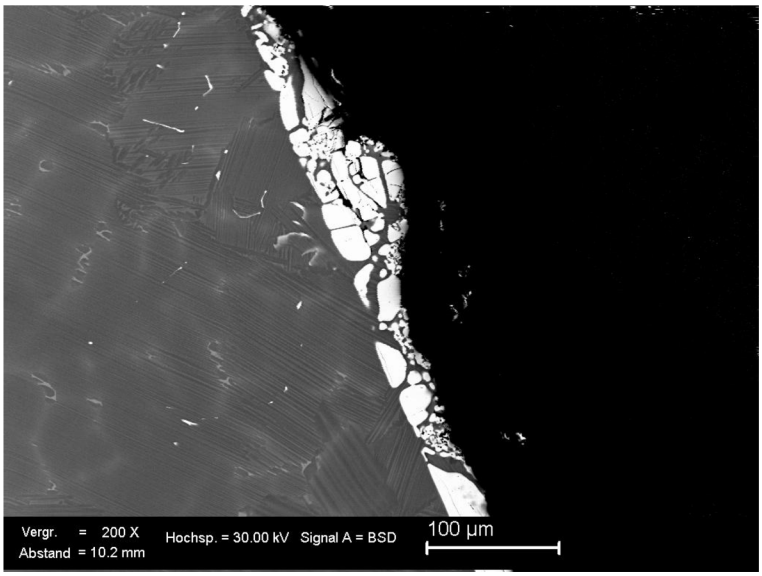

Fig. 43: Overview SEM - BSE image of interface between TiAlNb solidified alloy and Y_2O_3 ceramics wall. The interface and contamination are clearly visible inside the solidified melt.

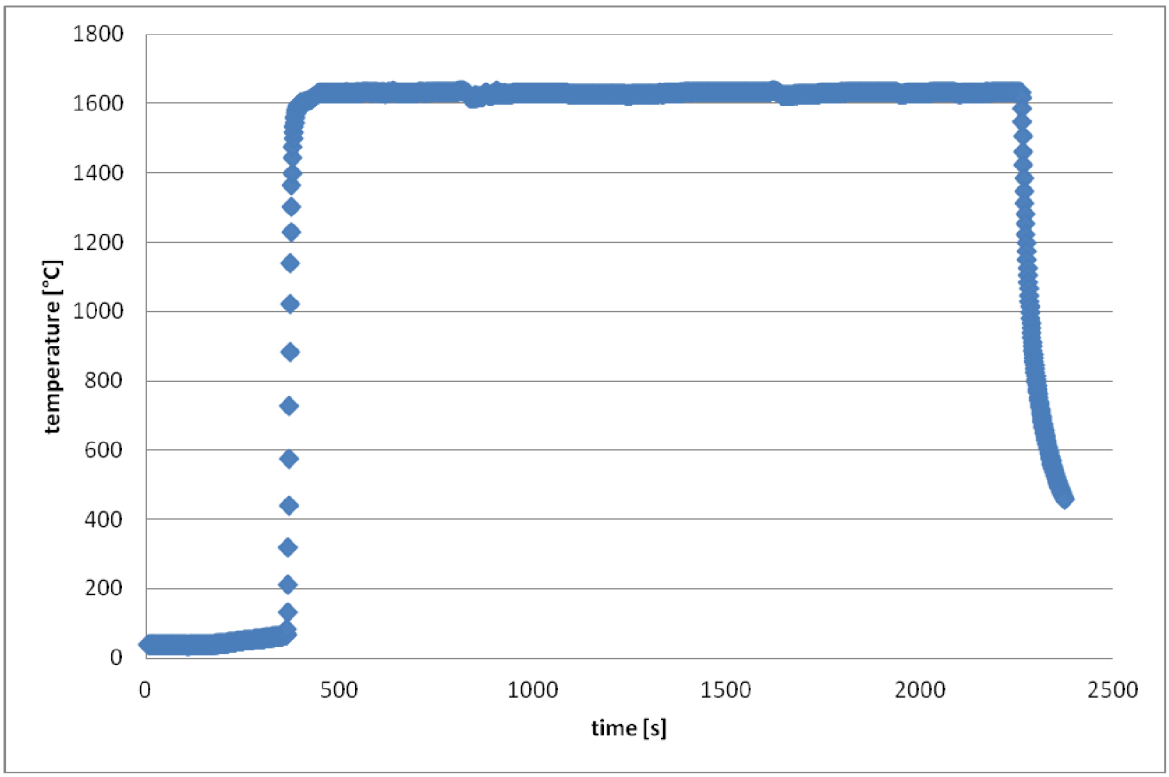

Fig. 44: Time-temperature data recorded for the melting experiment melt T10

SEM observations and analysis

The microstructure of TiAlNb intermetallic alloy close to the Y_2O_3 ceramic wall is presented in Figure 43. The SEM image in Figure 43 also documents contamination of the alloy by very small yttrium oxide particles. A detailed image of the microstructure is shown in Figure 45. The dendritic structure with small grains was also determined by EDS analysis. The results of this analysis are summarized in Table 20.

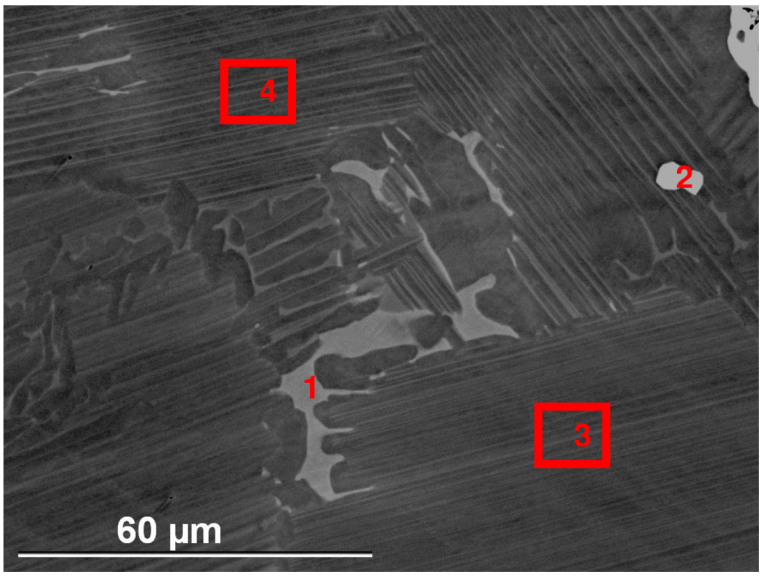

Fig. 45: Detailed BSE image of the microstructure of TiAlNb intermetallics after experiment Melt T9, with marked places of EDS analysis.

Tab. 20: EDX analyses in locations shown in Figure 45 (at. %)

Element	O	Al	Ti	Cr	Y	Nb
1		37.4	48.9	2.6		11.1
2	56.9				43.1	
3		45.8	45.7	0.5		8.1
4		45.8	45.2	0.7		8.4

TEM lamella preparation and observation

Using FIB – SEM microscope with nano-manipulator, TEM lamella from the area marked in Figure 46 was prepared. As it is shown in Figure 46 there is a very interesting area with the potential that some products of possible reaction could be found. Figure 47 proves that only two presented phases are TiAl intermetallics and material of crucible wall. In the same Figure 47 two TEM lamellas prepared on the TiAl - Y_2O_3 interface are ready to lift-out. After the lift out and transfer to the support grid, final polishing improved the thickness and surface quality, to be sufficient for TEM observation. The results from a transmission electron microscope did not confirm either the interaction products or gradients of elemental composition at the Y_2O_3-TiAl interface.

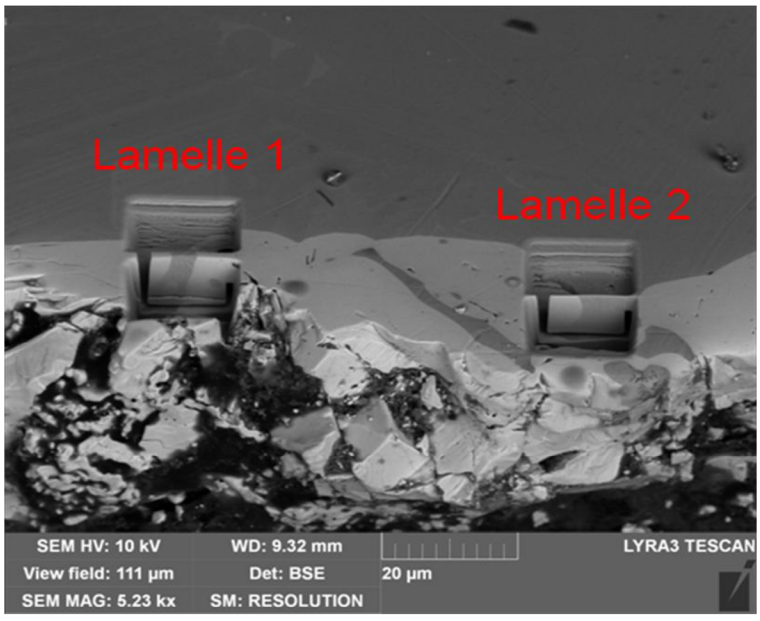

Fig. 46: Detailed BSE image of TEM lamellas ready for lift out - TiAl – Y_2O_3 interface.

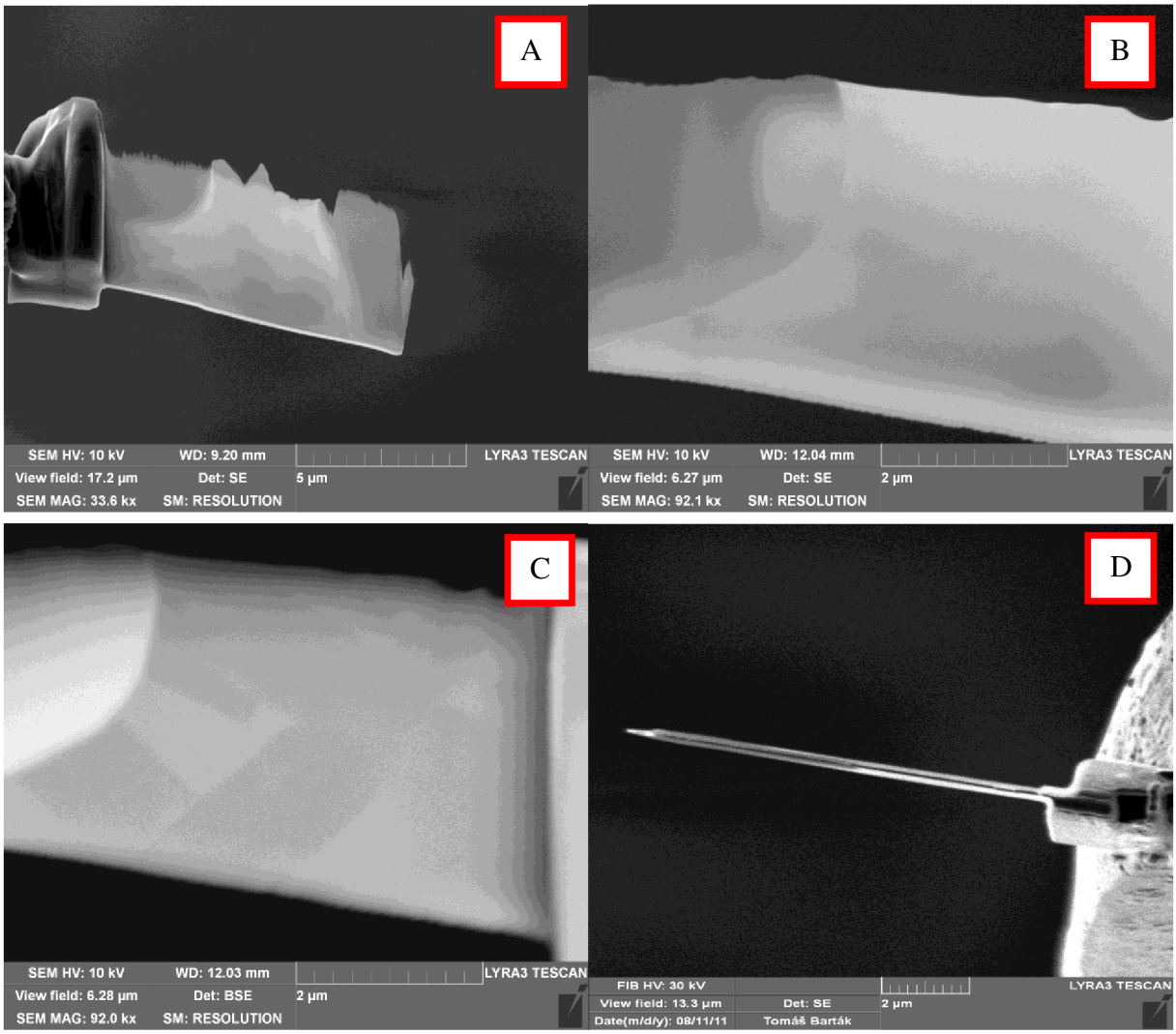

Fig. 47: Detailed BSE images of final lamellas of TiAl – Y2O3 interface: A – lamella 1 overview, B – lamella 2 SE image, C – lamella 2 BSE image, C – overview of final thickness.

- **Melt T11**

The melting charge for this experiment was prepared as 239.7 g of the primary GfE ingot. The time of overheat of the alloy at the temperature 1630 °C was 300 s. This melting trial was performed with the ceramic pin fixed on the bottom of the crucible.

Detail images of the cracked yttrium oxide crucible and pieces of the crucible after re-melting trial T11 are shown in Figure 48. Strong erosion of the inner part of the ceramics wall, a detailed image of the penetration of the TiAl intermetallic in to the wall and the image of thermocouple shield after the re-melting experiment are documented in Figure 48. The SEM image in Figure 49 is detail of cross-section documented in Figure 48.

After reaching the melting temperature at 1630 °C the experiment was successfully finished at 1000 s. The temperature of the experiment varied between 1625 °C and 1635 °C. The cross-section of the sample was investigated using SEM and EDS. The temperature was measured continuously and the corresponding record is shown in Figure 50.

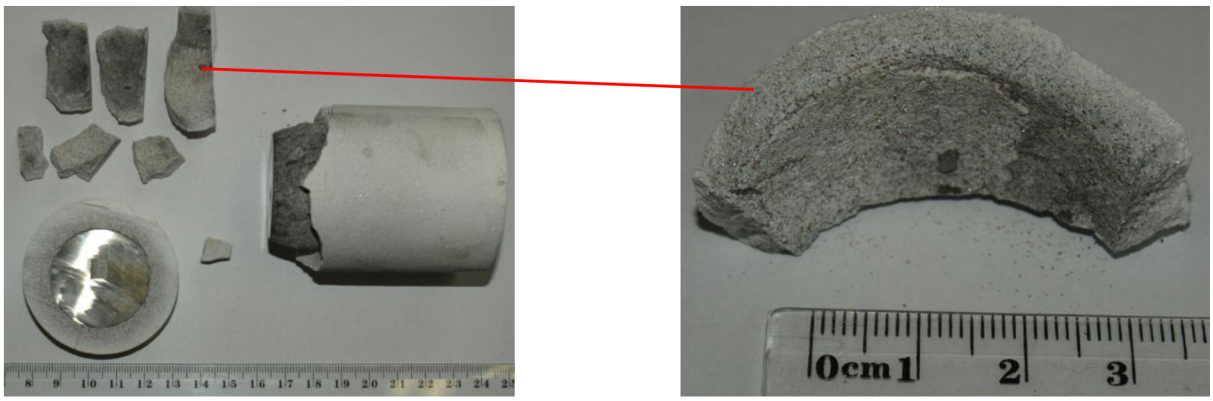

Fig. 48: Overview images of parts of crucible with solidified melt and part of the thermocouple shield.

SEM observations and analysis

Figure 49 shows an overview of the microstructure of TiAlNb intermetallics close to the Y_2O_3 ceramic wall. Also visible in the image is the contamination of the alloy by very small yttrium oxide grains. The overall results of EDS analysis are summarized in Table 21. Time-temperature data acquired during re-melting experiment T11 are presented in Figure 50.

Table 21: Average EDX analyses from selected places on alloy and ceramics (at. %)

Element	O	Al	Ti	Y	Nb
Intermetallic		45.8	45.7		0.5
Y_2O_3	56.9			43.1	

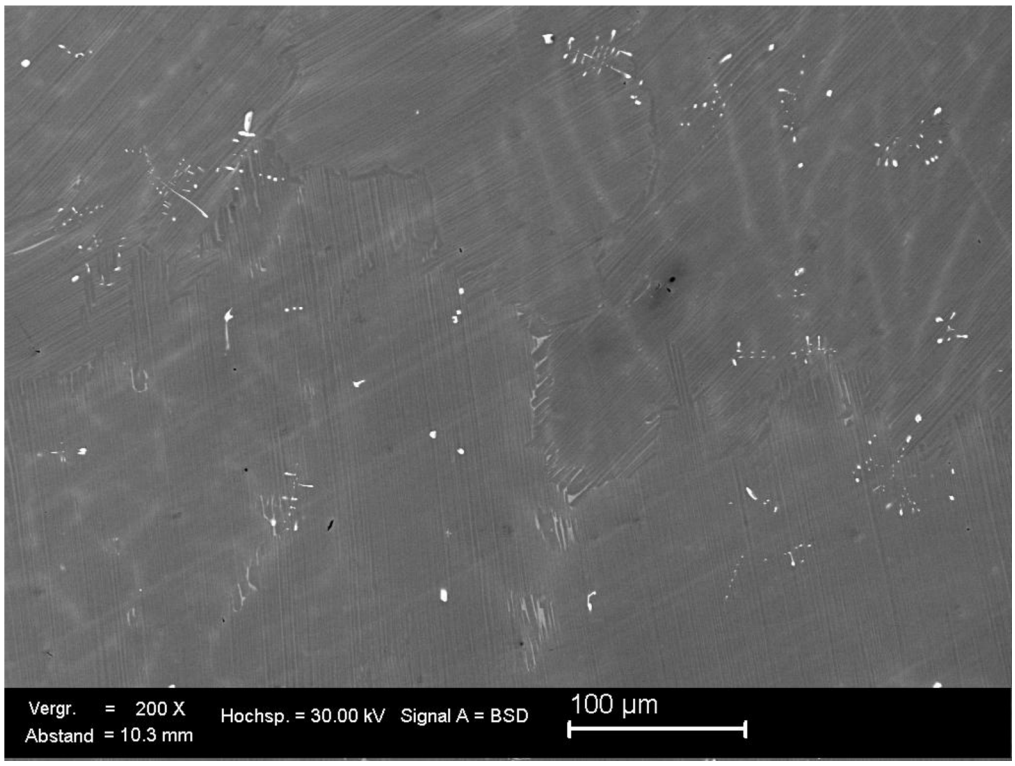

Fig. 49: Detailed BSE image of the microstructure of TiAlNb alloy after experiment T11.

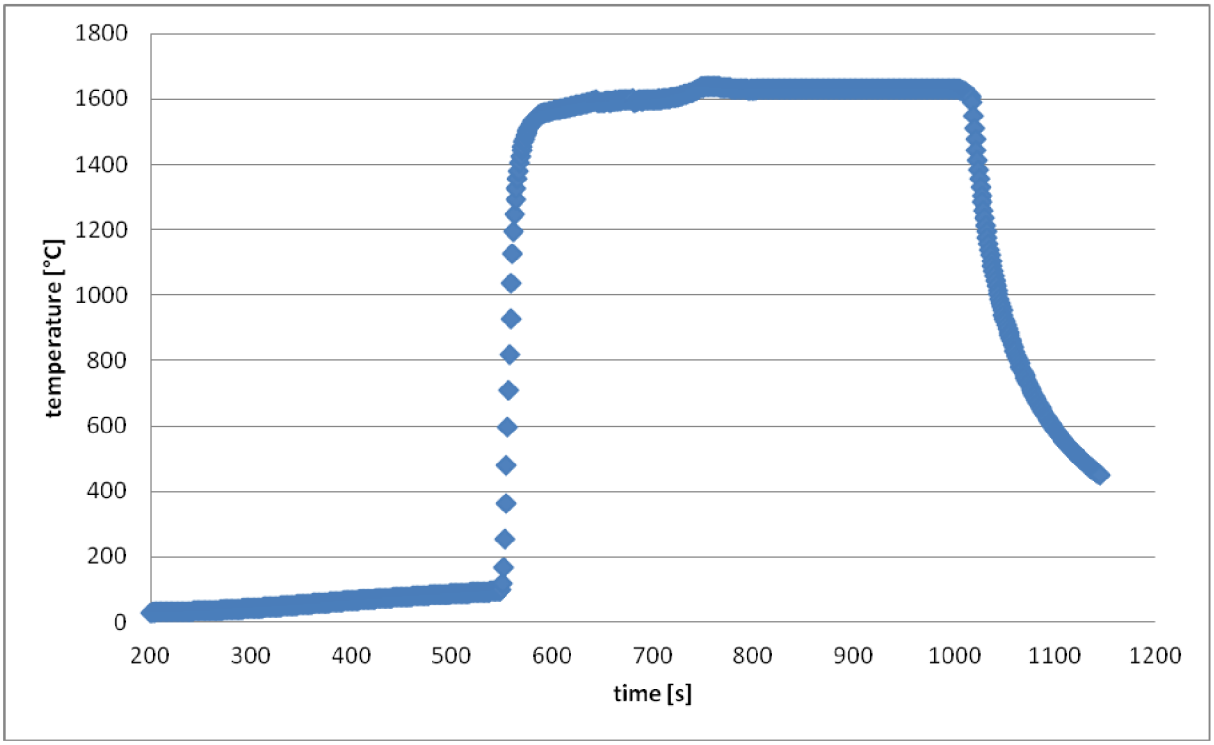

Fig. 50: Time-temperature data recorded for the melting experiment melt T11.

7.2.3. Volume fraction of ceramics particles

The volume fraction of ceramics particles was obtained from the SEM and OM images of cross sections with several magnification modes. The data on the particle volume fraction for each melt were evaluated from at least 50 SEM images. All images were analyzed by ACC 6.1. image analyzer. Table 22 and Figure 51 show a summary of the results of all experiments.

Tab. 22: Table of yttrium oxide particles content

time [s] \ temperature [°C]	**1630**	**1680**	**1730**
300	0.2 ± 0.02	0.4 ± 0.03	0.7 ± 0.05
900	0.3 ± 0.02	0.5 ± 0.04	0.9 ± 0.04
1800	0.4 ± 0.03	1.7 ± 0.10	-

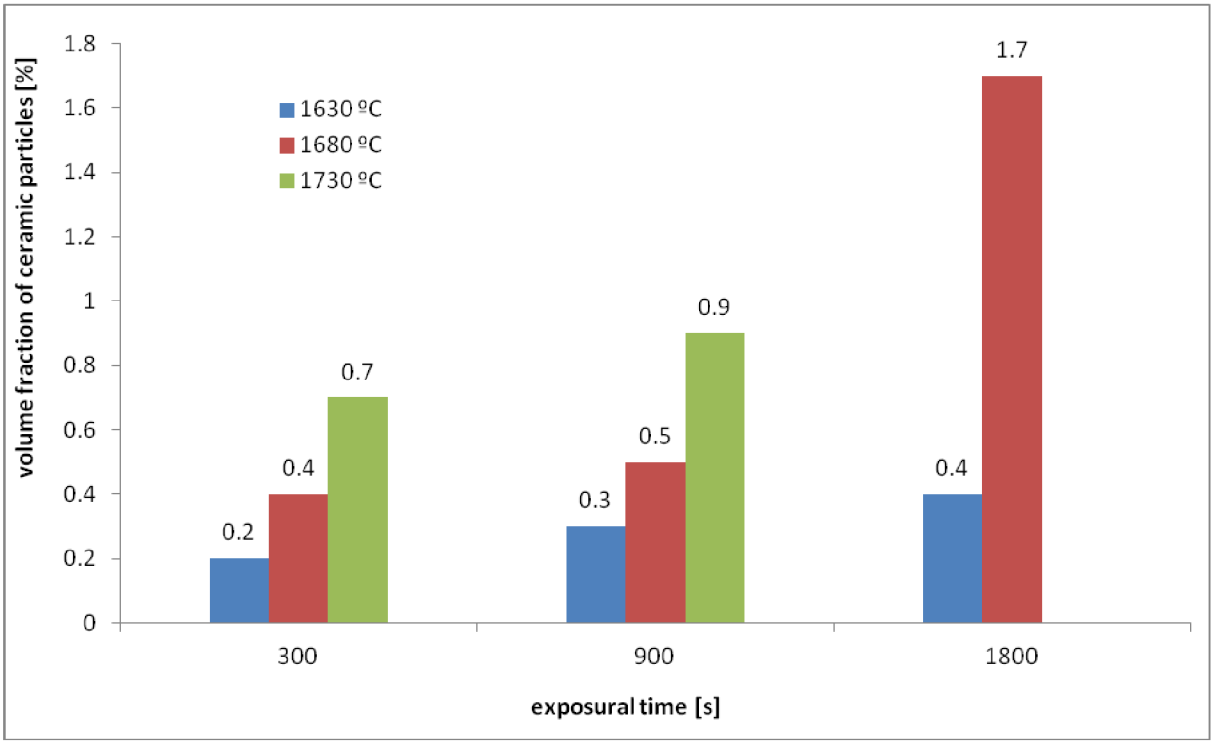

Fig. 51: Volume fraction of ceramics phase Y_2O_3 in the re-melted alloys.

7.2.4. Oxygen content

The Inert Gas Fusion (IGF) method was used to characterize the oxygen contamination of re-melted alloys. The results presented in Table 23 summarize a detailed position – based analysis where sampling across the re-melted ingot was taken into consideration. The result of average content of oxygen did not correspond to the average value calculated from table, because for some experiments not all available values are presented in the table.

The real oxygen content values are presented in Figure 52. To compare the real amount of oxygen coming to the alloy during the melting procedure, Figure 53 presents values of the oxygen content excluding content measured in primary ingots. In Figure 54 the data are presented together with the primary ingot oxygen content. This value used as the initial state and is seen in the Figure 54. The rate of oxygen contamination can be accessed from the fitted lines.

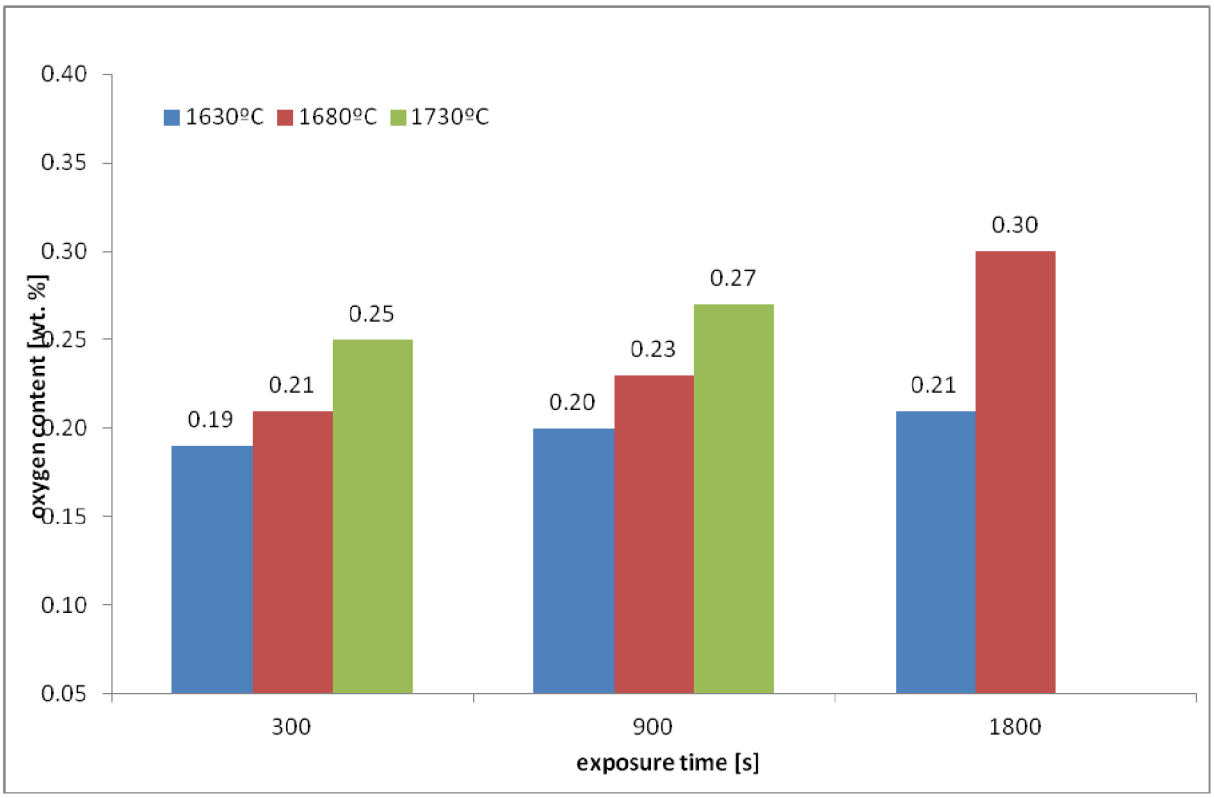

Fig. 52: Graph of the overall oxygen content

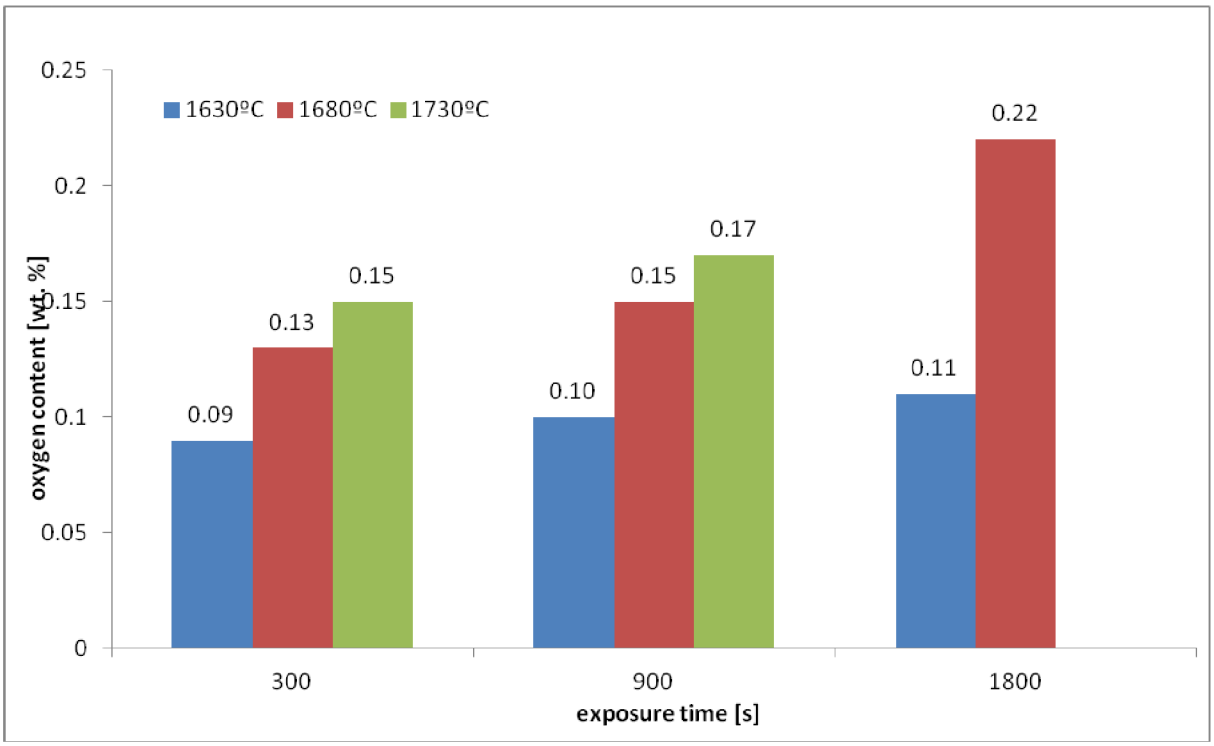

Fig. 53: Graph of oxygen content excluding the content of oxygen in the primary ingot

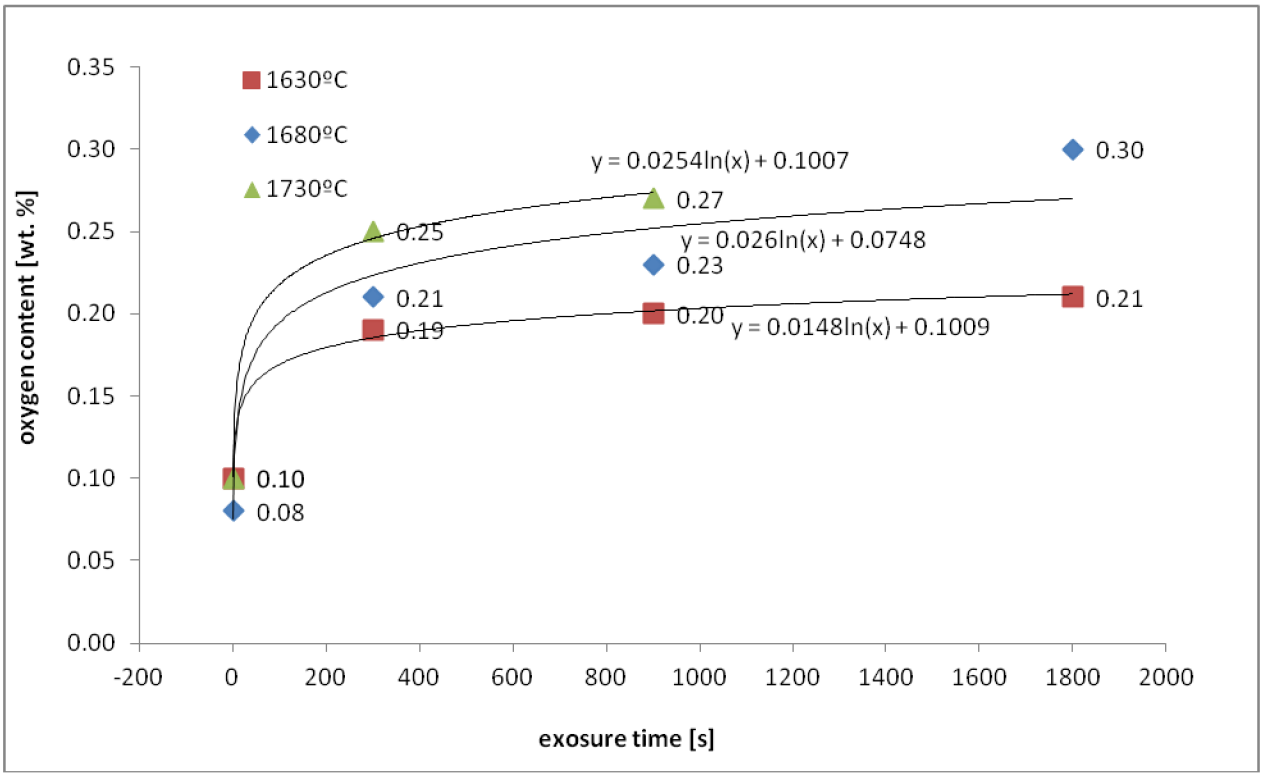

Fig. 54: Oxygen contamination as a function of exposure time, the temperature of the re-melting experiment is a parameter.

Tab. 23: Results of oxygen content analyses for all melts (wt. %)

wt.%	PI	**1**	**2**	**3**	4	**5**	**6**	**7**	8	**9**	Ø	minus PI
T1	0.078	0.2024	0.2320	0.2203	0.1841	0.1913					**0.206**	**0.128**
T2	0.078	0.2206	0.2232	0.2371	0.2197	0.2183	0.2172	0.2145	0.2184		**0.221**	**0.143**
T3	0.078	0.3014	0.3562	0.3418	0.2885	0.2618	0.2357	0.2914	0.3054	0.2890	**0.296**	**0.218**
T4	0.078	0.2358	0.2307	0.2402	0.2381	0.2290	0.2380	0.2364	0.2358	0.2467	**0.237**	**0.159**
T5	0.102	0.3246	0.2415	0.2467	0.1995	0.2025	0.2023	0.2023	0.2027	0.2011	**0.225**	**0.123**
T6	0.102	0.2080	0.2089	0.2041	0.2048	0.1957	0.2005	0.2044	0.2013	0.2055	**0.204**	**0.102**
T7	0.102	0.2768	0.2479	0.2351	0.2305	0.2051	0.2211	0.2684	0.2923		**0.247**	**0.145**
T8	0.102	0.3544	0.3395	0.3448	0.2361	0.2353	0.2366	0.2358	0.2381	0.3641	**0.274**	**0.172**
T9	0.102	0.2523	0.2408	0.2029	0.1910	0.2044	0.2013	0.2043	0.2048		**0.213**	**0.111**
T10	0.102	0.2107	0.2107	0.1940	0.2001						**0.197**	**0.095**
T11	0.102	0.1933	0.1972	0.1952	0.1872	0.1869	0.1885	0.1844	0.1875	0.1870	**0.190**	**0.088**

8. Discussion:

The results presented in this study present the first ever data on the contamination of TiAlNb – type alloy by oxygen during melting. The melting procedure was based on a cost effective induction melting in a refractory crucible. Different temperatures and holding times in a relevant range were considered. Based on the previous results [48], yttrium oxide crucibles were chosen to be the best crucible material whit a low contamination potential. Lower temperatures and short melting times lead to promising results as far as the contamination and purity of the final melt is concerned. These conditions, however, may not be sufficient to assure the required homogeneity of the final ingot [83-85]. This work provides a guide for optimizing melting parameters. Attention was paid to quantitative analysis of the oxygen content, shape and size of yttrium oxide particles as well as the volume fraction of yttrium oxide particles, depending on the melting temperature and melting time.

TiAl melting technology is a very complex process and many articles focus on it. The influence of parameters such as temperature, pressure, inert atmosphere and the addition of minority elements to improve the alloy quality was investigated [45-48, 54, 71-73, 86-88]. Previous studies, however did not address the issue of continuous temperature measurement during the re-melting experiments. This challenging task was fulfilled in the present work. However the old method of temperature measurement using a B type thermocouple (platinum - rhodium) was not sufficient, mainly for temperatures exceeding 1680 °C and melting times longer than 900s. Using the C type of thermocouple (tungsten-rhodium) enabled continuous measuring of temperature during all experiments. Proper control of the melting process in terms of the thermocouple could be very influential even for a potential industrial application. Each case of temperature instability could have severe consequences for the quality of final casting products [83].

One of the first questions about the suitability of melting TiAlNb intermetallics in Y_2O_3 crucibles is if the crucible material is stable enough and if there is some expected reactions between crucible and alloy. The basis for an answer was published in the work [48, 89] in which the Y_2O_3 crucible was first used, and this work builds on that study. Results of thermodynamic calculations presented in this work based on the value of Gibbs free energy of reactants and products confirms that in the range of temperatures between 1630 °C - 1680 °C no reaction ise expected. Nevertheless, as was discovered in the work [54] it is important to use even the activity of system compounds in the form of prediction criteria to say if the reaction is possible or not. As is presented in this work, the activity of compounds in the melt is very low and the stability of the crucible material is too high so that direct reactions of components are not possible over the whole range of studied temperatures. Theoretical work concerning calculations of activity of Ti and Al using the FactStage software in a wider range of temperature has been presented [82], and the results are in agreement with our results based on presented pressure of gaseous Al [46]. Nevertheless, at the beginning of reaction when the

TiAl alloy is pure and does not content any Y, it would expect strong potential for decomposition or dissociation of Y_2O_3 and transport of Y and O to the melt. Driving force for this process is dissociation pressure of oxygen the beginning of melting procedure, when the activity of yttria in melt is very close to 0. At the image 55 - relationship between activity and thermodynamics potential.

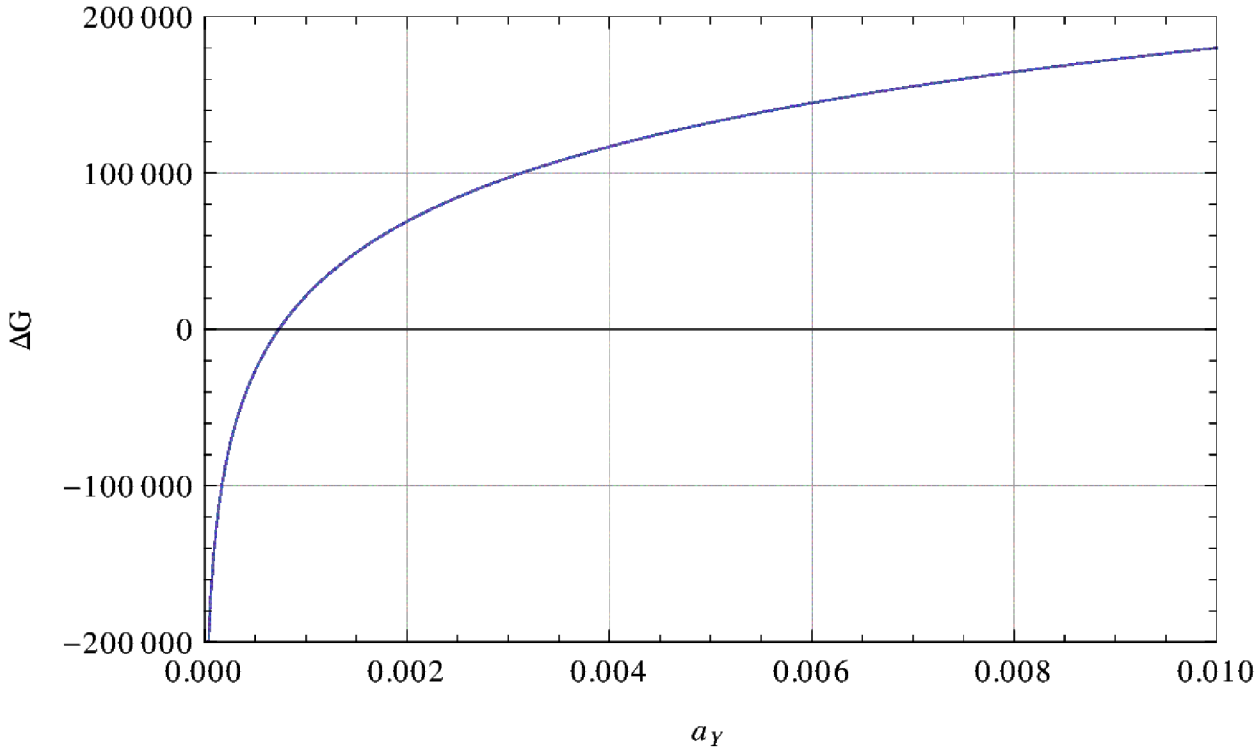

Fig. 55: Activity of Yttria at the beginning of melting process for temperature 1680°C

Thermodynamic calculations have been confirmed by a series of melting experiments, the results of which are presented in this work. Cutting the solidified melt – crucible structure was performed with a circular saw using a new holder designed especially for this experiments. The method of preparation of metallographic cross-sections was taken from [46] and improved to achieve smooth surface without scratches. For a brief inspection of cross-sections, light microscopy was used. The final analysis of microstructure and composition was performed using SEM and EDS system. EDS analysis proved to be a very useful technique to evaluate the composition of relatively large areas in a range from hundreds of nanometers to a couple of micrometers – depending on the diameter of the beam and accelerating voltages. However, a proper study of the chemical composition of ceramics - intermetallic interface required the limitation of the interaction volume between the electron beam and specimen. Therefore, in order to reduce the interaction volume, TEM lamellae from the interface were prepared using electron microscope with FIB. This unique method is sufficient to prepare the TEM sample from the exact location. The results from TEM

confirmed that no gradient of concentration or wide diffusion layer is presented across the intermetallic-crucible interface.

SEM images were used for the quantitative evaluation of the contamination of re-melted intermetallic by Y_2O_3 particles. Using ACC software, a representative number of images were analyzed in different magnifications. Values of surface particle content are in related magnification corresponding to volume fraction. The results of the volume fraction of ceramic particles are shown in Figure 49. There is a clear influence of temperature on the level of melt contamination by Y_2O_3 particles. Comparing the same exposure time (30 min) there is more than four times higher contamination by yttria particles in the 1680 °C experiment compared to 1630 °C. The difference in shorter time experiments is smaller, which means that the exposure time also has less influence. Not only the volume fraction of particles was observed. The obtained SEM data enable assessment of Y_2O_3 particle sizes, see Figure 56. There are three different exposure times for one temperature 1680ºC (images a, b, c). As shown these images reveal the correlation between exposure time and size and shape of Y_2O_3 ceramics particles. A quantitative assessment of the ceramic particle volume fraction yielded results shown in Figure 10 and demonstrate the size distribution of yttria grains in the ceramic wall before being used for the melting experiment. Assuming these facts, we can say that the smaller particles as a binder of larger grains is disconnected from the crucible wall in the first minutes of melting. Once the smaller grains are dissolved out of from the wall there is no longer support for bigger grains and these could be take out from the wall too . This kind of erosion is typical for furnace material used in glass technology [68].

The contamination of the intermetallic melts by the oxygen during the re-melting experiments is on one hand direct consequence of the dissolution of yttrium oxide in the melt but on the other hand, is connected to the volume fraction of yttria grains ejected into the sample.

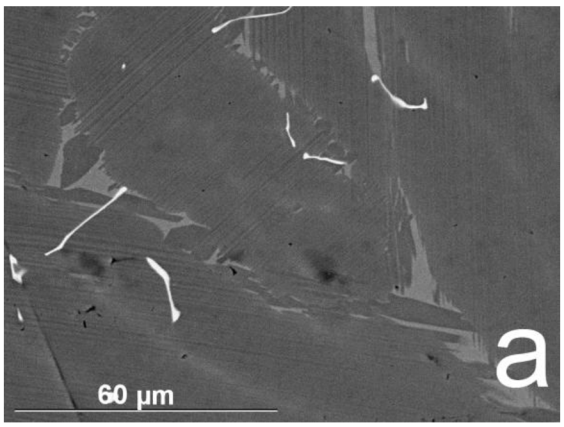

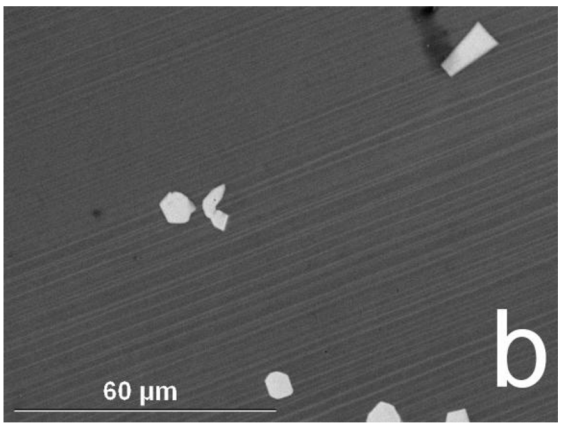

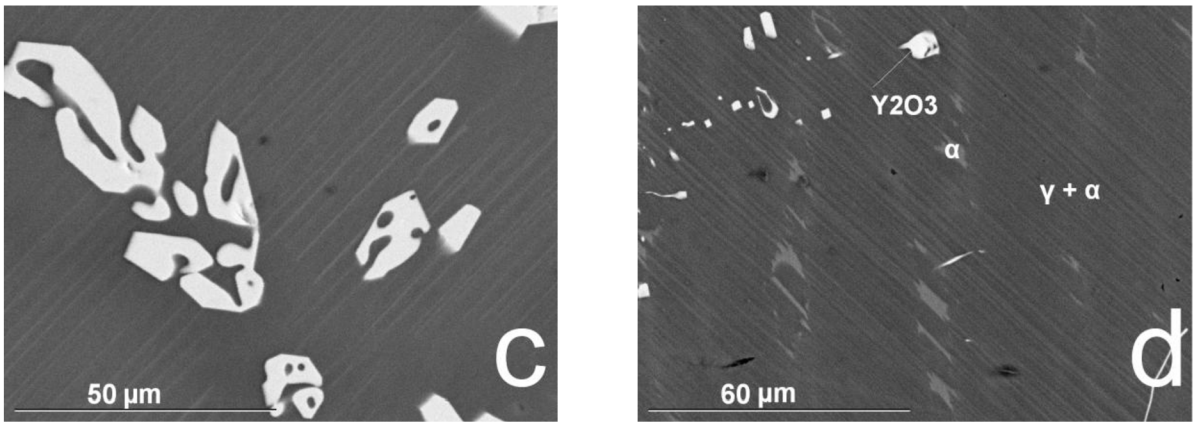

Fig. 56: Microstructure of TiAl alloy after re-melting (a) melt T6, (b) melt T2, (c) melt T4, (d) melt T7.

9. Conclusions:

This dissertation reports on VIM experiments in which a primary master niobium containing a TiAl intermetallic alloy was re-melted in Y_2O_3 crucibles at three different temperatures and at three different melting times. Based on the experimental results, following conclusions can be drawn:

1) The vacuum induction melting (IVM) method was used to perform eleven different re-melting experiments of intermetallic alloy Ti47Al7Nb in Y_2O_3 ceramic crucibles. Three different melting temperatures and three different melting times were used. The metallographic sample preparation method for preserving the interface between the solidified melt and ceramic crucible was developed.

2) The solidified intermetalic – ceramic interface was observed using light and scanning electron microscopy and analyzed by an X-ray energy dispersive (EDX) analyzer. Lamellas for transmission electron microscopy were prepared using an electron microscope with an integrated focus ion beam. Thin samples were use to identify the composed phases using selected area diffraction.

3) Reactions at the interface between the solidified intermetallic and Y_2O_3 ceramics crucible were not observed. No products of reactions between the melt and crucible where found. These results were supported by thermodynamic calculations. There is possibly a slight gradient of elemental composition at the interface of alloy and crucible, however, this gradient is probably the effect of the dissociation of ceramic crucible wall during the beginning of melting process. We can say that there is no sharp reaction interphase and the gradient of the concentration of minor elements around the interface is very small.

4) However, the contamination of the TiAl melt is quite intensive. The mechanism of this process is ceramic wall erosion caused by inductive current induced by melt blending. Therefore, the melt initially received only small ceramic grains and longer melting times caused the drifting out of larger grains. These grains are dissolved in melted intermetalics and this process causes an increasing oxygen content in re-melted alloy. This result also means that the yttrium content in the alloys increases, but this is not possible to confirm by EDS analysis, because the composition of Yttria is out of the detection limit of the EDS method. Measuring the yttria content in the alloy using a different method for example WDS is a possible topic for a future study.

5) The volume fraction of ceramic particles transferred into the melt was evaluated using the ACC image analyzer. The highest volume fraction of yttria particles (1.7%) was found in the cast microstructure after melting at 1730 °C and 900 s almost ten times smaller (0.2%) was measured at the cast microstructure prepared at 1630 °C and the melting time of 300s. The results show that the volume fraction of particles in the alloy depended mainly on melting temperature.

6) Oxygen content measurement results using IGF showed that the highest contamination values are characteristic for alloys melted at the highest temperatures. This fact is also supported by thermodynamic calculations, which confirmed that with increasing temperature, the Gibbs free energy of the reaction solvent decreases.

8) The experiments have also resulted in a new design for continuous measurement of temperature of the melt during the melting experiment. Thermocouple type C (tungsten-rhenium) made it possible to achieve smooth measurements during the entire experiment lasting more than 30 minutes at temperatures up to 1730°C.

Based on the experimental results (TEM, SEM, EDX), thermodynamic calculations, image analysis and the analysis of oxygen contamination, due to the erosion of Y_2O_3 ceramic crucibles, the following recommendation can be made as far as further melting and optimization of the TiAlNb casting process.

R1) Make the process of melting as short as possible to minimize yttria grain and equally oxygen contamination of the TiAl alloy as well as to minimize expenses connected with electric energy consumption. The process of melting could generally be very short in the case of good the homogeneity of the primary alloy.

R2) To minimize oxygen contamination of the alloy it is necessary to reduce the melting temperature to a minimum. Because the temperature is one of the most important factor of melt viscosity, the minimum possible temperature will strongly depend on casting technology and the shape and thickness of the inner part of the casting form. Thinner and more complicated shapes of the casted part will need to heat the alloy to high temperatures, which increases the oxygen content in the final product.

R3) Use type C thermocouples with a Mo-Al_2O_3-ZrO_2 shiled and protective yttrium oxide coating for measuring the temperature of overheated melt during melting. The possibility of continuous measurements and high durability is ensured when restoring the protective Y_2O_3 coating after each use.

R4) Final costs for the presented melting technology - TiAl intermetallics in Y_2O_3 crucibles are very high in the laboratory mode. The price of the crucible is one of the major

contributions. However after the introduction of continuous production we could expected a substantial reduction in the manufacturing costs of the crucible as well as repeated use of the same crucible for more castings cycles which was not possible during the laboratory experiments.

R5) Applying the electric potential on the crucible wall could be helpful to reduce the dissociation potential of ceramics wall during melting.

10. References:

[1] TETSUI, T.: Development of a New TiAl for High Temperature Use. *3rd International Workshop on Gamma TiAl Technologies,* 28th – 31st May 2006, Bamberg, Germany, [CD].

[2] LIU, C. T., MAZIASZ, P. J.: Microstructural control and mechanical properties of dual-phase TiAl alloys. *Intermetallics,* 1998, vol.6, no. 7-8, p. 653–661.

[3] KROL, S., at. all: The influence of chosen parameters on the course of cyclic oxidation of TiAl Intermetallics. *Slévárenství*, 2007, vol. 55, no. 7, p. 303-306.

[4] JONES, S., MARQUIS, P.M.: Interaction Between Gamma TiAl and Pure Oxide Refractories. *10th World Conference on Investment Casting*, 14th -17th 2000, Paper7, 20p., Le Metropole Hotel, Monte Carlo.

[5] YANQING, S., at all: Composition Control of TiAl Melt During the ISM process. *Journal of Alloys and Compounds,* February 2002, vol. 334, no. 1-2, p. 261-266.

[6] KIM, YOUNG-WON: *Gamma Titanium Aluminides*, JOM, 1995, p. 475–483, ISSN 1047-4838.

[7] KUANG, J. P., at all: Investigation into refractory as crucible and mould materials for melting and casting γ-TiAl alloys. *Materials Science and Technology,* 2000, vol. 16, no. 9, p. 1007-1016.

[8] ZEMČÍK, L., DLOUHÝ, A.: Metalurgie Intermetalických Slitin Typu TiAl. *Metal 2003*. 20th – 22nd May 2003, Hradec nad Moravicí, ČR, ISBN 80-85988-82-8.

[9] LAMINARD, M.: Relative Effects of Cr and Nb on Microstructure and Mechanical Properties as a Function of Oxygen Content in TiAl Alloys. *Skripta Materialia,* 2007, vol. 55, no. 5, p. 325-328

[10] RISHEL, L. L., at. all: Cast Structure and Property Variability in Gamma Titanium Aluminides, *Intermetallics*, 1998, vol. 6, no. 7-8, p. 629–639.

[11] TAKEYMA, M., at. all: Phase Equilibria and Microstructural Control of Gamma TiAl Based Alloys, *Intermetallics*, 1998, vol. 6, no. 7-8, p. 643–646.

[12] LORETTO, M. H., at. all: The Influence of Composition and Processing on the Structure and Properties of TiAl Based Alloys, *Intermetallics*, 1998, vol. 6, no. 7-8, p. 663–666.

[13] JIANBO, LI, at. all: High Temperature Deformation Behavior of Near Gamma Phase High Nb-coating TiAl alloy. *Intermetallics,* 2014, vol. 52, no. 5, p. 49-56

[14] YANG, R., at. all: Alloy Development and Shell Mould Casting of Gamma TiAl, *Journal of Materiále Processingn Technology*, 2003, vol. 135, no. 2-3, p. 179–188.

[15] YING, W., at. all: The formation mechanism of the O phase in a Ti3Al±Nb alloys. *Intermetallics*, 2000, vol. 8, no. 5-6, p. 629-632.

[16] RYBIN, V., V.: Examining the Bimetallic Joint of Orthorhombic Titanium Aluminide and Titanium Alloy (Diffusion Welding). *Welding Journal* [online]. 07/2007, [cit. 2014-06-11]. Available from: http://www.aws.org/wj/supplement/WJ_2007_07_s205.pdf

[17] WESTBROOK, J. H., FLEISCHER, R. L.: *Intermetallics Compounds, Volume 2, Basic Mechanical Properties and Lattice Defects of.* 2nd Edition, Wiley, 2000, 284 pages, ISBN: 978-0-471-61175-2.

[18] HENAF, G., GLOANEC, A.: Fatigue Properties of TiAl. *Intermetallics,* 2005, vol. 13, no. 5, p. 543 – 558.

[19] KUANG, P., at. all: Microstructures and Properties of Investment Casting of gamma titanium aluminide. *Material Science and Engineering A,* 2002, vol. 329-331, p. 31-37.

[20] HU, D., at. all: Microstructure and Tenzile Properties of Cast Ti-44Al-4Nb-4Hf-0.1Si-0.1B Alloy With Refined Lamellar Microstructures. *Intermetallics,* 2009, vol. 17, no.1, p. 744-748.

[21] DLOUHÝ, A., KUCHAŘOVÁ, K., ORLOVÁ, A.: Long-therme Creep and Creep Rupture Characteristic of Ti-Al Base Intermetallics. *Materials Science and Engineering A,* 2009, vol. 510-511, p. 350-355.

[22] LIN, J. P., at all: High Temperature Deformation Behaviors of High Nb Coating TiAl Alloy. *Intermetallics,* 2007, vol. 15, no. 5-6, p. 668-674.

[23] WANG, J. N., XIE, K.: Refining of Course Lamellar Microstructure of TiAl Alloys by Rapid Heat Treatement, *Intermetallics,* 2000, vol. 8, no. 5-6, p. 545-548.

[24] XIA, Q., WANG, J. N., at. all: On the Massive Transformation in TiAl Based Alloys. *Intermetallics,* 2001, vol. 9, no. 5, p. 361-367.

[25] WANG, J. N., at all: Microstructural Instability in Crept Fully Lamellar TiAl Alloy. *Intermetallics,* 1999, vol. 7, no. 7, p. 757-763

[26] KIM, YOUNG-WON: Strenght nad Ductility in TiAl Alloys, *Intermetallics,* 1998, vol. 6, no. 7-8, p. 623-628.

[27] KIM, S-W., at all: In Situ TEM Study on Room Temperature Ductility of TiAl Alloys With Fully Lamellar Microstructure, *Material Science and Engineering A,* 2014, vol. 589, no. 1, p. 140-145.

[28] RECINA, V., AHLSTROM, J., KARLSSON, B.: Sample Preparation and Micro-structural Characterization of the Gamma Titanium Aluminide Ti-48Al-2W-0.5Si, *Materials Characterization,* 1997, vol. 38, no. 4-5, p. 287-300.

[29] ZHENG, R. T., at all: The Ambient Temperature Tensile Behavior of Duplex TiAl Based Alloys, *Material Science and Engineering A,* 2003, vol. 362, no. 1-2, p. 192-199.

[30] GUO, A. F., at all: Effect of Internal Stresses on The Fracture Toughness of TiAl Based Alloy with Duplex Microstructure, *Acta Materialia,* 2003, vol. 51, no. 18, p. 5349-5358.

[31] WANG, J. N., XIE, K.: Grain Size Refinement of a TiAl Alloy by Rapid Heat Treatment, *Scripta Materialia,* 2000, vol. 43, no. 5, p. 441-446.

[32] QUIANGFEI, XIA, at all: Efect of Heating Rate on The Grain Refinement of TiAl Alloy by Cyclic Heat Treatment, *Material Science and Engineering A,* 2001, vol. 300, no. 1-2, 309-311.

[33] GUXIN, CAO, at all: The Relationships of Microstructure and Properties of Fully Lamelar TiAl Alloy. *Intermetallics,* 2000, vol. 8, no. 5-6, p. 647-653.

[34] HUANG, S. C., at all, *Structural intermetallics*. 1993, Warrendale, PA, TMS, p. 299, *ISSN* 0938-0108.

[35] HUANG, S. C., McKEE, D. W.: The Oxidation Behavior of Gamma Titanium Aluminide Alloys under Thermal Cycling Conditions. *Corrosion Science,* 1992, vol. 33, no. 12, p. 1899-1914.

[36] WANG, YONG, at. all: Control of Fined Grained Microstructure for Cast High-Cr TiAl Alloys. *Material Science and Engineering A,* 2005, vol. 392, no. 1-2, p. 235-239.

[37] NISHIKIORY, S., at all: Microstructure and Creep Strength of Fully-Lamellar TiAl Alloys Containing Beta Phase, *Material Science and Engineering,* 2012, vol. 329-331, p. 208-209.

[38] WANG, J. N., at all: On the Grain Size Refinement of TiAl Alloys by Cyclic Heat Treatment, *Material Science and Engineering A,* 2002, vol. 329-331, no. 5-6, p. 118-123.

[39] BARBI, N., at all: Fracture and Convoluted and Lamellar alpha$_2$ and gamma TiAl Alloys, *Intermetallics*, 2012, vol. 22, p. 176-188.

[40] WANG, Y. H., at all: Microstructure and Mechanical Properties of As-Cast Ti-45Al-8.5Nb-(W, B, Y) Alloy with Industrial Scale, *Material Science and Engineering A,* 2007, vol. 471, no. 1-2, p. 82-87

[41] PARTHASARATHY, T. A., at all: Observation of Creep Bahaviour of Fully Lamellar Polycrystalline TiAl: Identification of Critical Effects. *Scripta Materialia*, 1997, vol. 37, no. 3, p. 315-321.

[42] CHAN, K. S., KIM, Y-W.: Effects of Lamellae Spacing and Colony Size on the Fracture Resistance of Fully Lamellar TiAl Alloy. *Acta Metallurgica et Materialia,*1995, vol. 43, no. 2, p. 439-451.

[43] MUHLBAUER, A.: *History of Induction Heating and Melting*, Vulkan, Germany, 2008, 175 p., ISBN 978-3-8027-2946-1

[44] ASHTON, M. C.: Induction Scull Melting (ISM) of Titanium Alloys [online]. [pub. 2007-03-08], [cit. 2014-06-12]. Available from: http://www.castingstechnology.com/ismtialloys.asp

[45] ZEMČÍK, L., DLOUHÝ, A.: Tavení Intermetalických Slitin Typu Gama TiAl ve Vakuových Indukčních Pecích. *Slévárenství,* 2004, vol. 52, no. 6, p. 223-227.

[46] ZEMČÍK, L., DLOUHÝ, A.: Metalurgie Intermetalických Slitin Typu Gama TiAl. *METAL 2003* [CD-ROM]. Ostrava, Tanger, 2003, s.1-6

[47] ZEMČÍK, L., DLOUHÝ, A., KRÓL, S.: Vakuová Metalurgie Intermetalik TiAl. *METAL 2005*, *14. mez. konference metalurgie a materiál*u. Ostrava, TANGER, 2005, p. 1 – 7. ISBN 80-86840-13-1.

[48] DOČEKALOVÁ, K., *Fyzikálně Chemické Aspekty Přípravy Slitin na Bázi Gama – TIAl*, PhD. Theses, 2006, FCH VUT, Brno

[49] KUANG, J. P., HARDING, R. A., CAMPBELL, J.: Microstructures and properties of Investment Casting of Gamma Titanium Aluminide. *Materials Science and Engineering,* 2002, vol. 329-331, no. 6, p. 31-37.

[50] KIM, M-G., at all: Microstructure, Metal-Mold Reactions and Fluidity of Investment Cast TiAl Alloy. *Materials Transakcions,* 2004, vol. 45, no. 2, p. 536-541.

[51] GSCHNEIDNER, K. A., at all, *Handbook of Physics and Chemistry of Rare Earths Volume 39*, 1st edition, 2009, Elsevier, 411 p., ISBN 978-0-444-53221-3.

[52] SUILIK, A. S. B., at all: Preparation and High Temperature Oxidation Behavior of Refractory Coatings for Gamma TiAl Intermetallics Compounds. *Intermetallics,* 2007, vol 15, no. 8, p. 1084-1090.

[53] GAO, J., at all: Oxidation Behavior of Gamma TiAl Based Alloy With Al_2O_3-Y_2O_3 Composite Coatings Prepared by Electrophoretic Deposition, *Surface and Coatings Technology,* 2011, vol. 205, no. 19, p. 4453-4458.

[54] ZEMČÍK, L.: *Studium pochodů na rozhraních žárovdornina - tavenina - atmosféra ve vakuových pecích*, Habilitační práce, Ostrava, 2001.

[55] KOBAYASHI, Y. and TSUKIHASHI, F.: Thermodynamics of Yttrium and Oxygen in Molten Ti, Ti3Al and TiAl. *Metallurgical and Materials Transactions B*, October 1998, vol. 29B, p. 1037–1048.

[56] CHEN, B., MA, Y., GAO, M., and LIU, K.: Changes of Oxygen Content in Molten TiAl Alloys as a Function of Superheat during Vacuum Induciton Melting, *Journal of Material Science and Technology,* 2010, vol. 26, no. 10, p. 900-903.

[57] RENJIE, C., at all: Interactions Between TiAl Alloys and Yttria Refractory Material In Casting Process. *Journal of Materials Processing Technology,* 2010, vol. 210, p. 1190-1196.

[58] DJUROVIC, D., ZINKEVICH, M., ALDINGER, F.: Thermodynamics Modeling of the Yttrium-Oxygen System. *Computer Coupling of Phase Diagrams and Thermochemistry,* 2007, vol. 31, p. 560-566.

[59] MOORE, J.J.: *Chemical Metallurgy*, Butterworths, London 1981, England, p. 1-380, ISBN 0 408 00430 4

[60] KUBASCHEWSKI, O., ALCOCK, C.B.: *Metallurgical Thermochemistry*. 5th Edition Revised and Enlarged, Pergamon Press Ltd., Oxford, England, 1970, ISBN 0 08 020897 5

[61] COUDURIER, L., HOPKINS, D.W., WILKOMIRSKY, I.: *Foundamentals of Metallurgical Processes. 2nd Edition.* Pergamon Press Ltd., Oxford, England, 1978

[62] PARKER, R.H.: *An Introduction to Chemical Metalurgy*. Pergamon Press Ltd., Ontario, Canada, 1978, ISBN 0-08-022125-4

[63] FILIPPOV, S.: *The Theory of Metallurgical Processes.* MIR, Moscow 1975, ISBN 0-07-0335876-5

[64] ZEMCIK, L.: *Formation on Oxide Films in Castings From Nickel-Base Superalloys*. International Journal of Metalcasting, in press

[65] DEVEREUX, O.F.: *Topics in Metallurgical Thermodynamics*. John Willey & Sons Inc., Canada, 1983, ISBN 0 471 86963 5

[66] ROSENQUIST, T.: *Principles of extractive metallurgy*. McGraw-Hill Book Co, Singapore, 1985, ISBN 0-07-053910-3

[67] RAY, H. S., SRIDHAR, R., ABRAHAM, K. P.: *Extraction of Nonferrous Metals*, Affiliated East-West Press PVT LTD, EWP, New Delphi – Madros, India, 1985

[68] ŠATAVA, V.: *Úvod do Fyzikální Chemie Silikátů*, SNTL, Praha, 1965, 407 p.

[69] KOBAYASHI, Y., at all: Consideration of the Influence of Contamination from Oxide Crucibles on TiAl Cast Material and Possibility of Achieving Low Purity TiAl Precision Cast Turbine Wheels. *Intermetallics,* December 2012, vol.31, p. 274-281.

[70] KARTAVYKH, A. V., at all: TiAl-Nb Melt Interaction with AlN Refractory Crucible. *Materials Chemistry and Physics,* 2009, vol. 116, p. 300-304.

[71] DLOUHY, A., DOCEKALOVA, K., BARTAK, T., DLOUHY, I., ZEMCIK, L., *Refractory crucible melting and related mechanical properties of Nb-containing TiAl alloys.* TMS 2008 Annual Meeting & Exhibition, New Orleans, Louisiana, USA, 2008, p. 9-14, ISBN 0873397169

[72] BARTÁK, T., DLOUHÝ, A., DOČEKALOVÁ K., ZEMČÍK, L.: Interactions between Ti- Al - Nb melts and Y_2O_3 crucibles. [CD-ROM], *Metal 2008, Hradec nad Moravicí*, ČR, 2008.

[73] DOČEKALOVÁ, K., DLOUHÝ, A., ZEMČÍK, L., FIALA, J.: Interakce mezi TiAl taveninou a keramickými tavicími kelímky s povlaky. [CD-ROM] *Konference Metal 2005*, Hradec nad Moravicí, 2005

[74] GOLDSTEIN, J., at all: *Scanning Electron Microscopy and X-Ray Microanalysis,* 3rd Edition**,** 2003, Springer US, 689 p. ISBN 0306472929

[75] ECHLIN, P., at all: *Advanced Scanning Electron Microscopy and X-Ray Microanalysis,* 2013, Springer US, 454 p. ISBN 1475790295

[76] WILIAMS, D. B., CARTER, C.B.: *Transmission Electron Microscopy A Textbook for Material Science,* 2nd Edition, 2009, Springer US, 757 p. ISBN 978-0-387- 76502-0

[77] DLOUHÝ, A., BOJDA, O., FIALA, J.: Kvantitativní Obrazová Analýza Fází v Tvarově - Paměťových Slitinách NiTi. [CD-ROM], *13th International Metallurgical and Material Conference,* Hradec nad Moravicí, ČR, 2004

[78] *Official website of VUHZ company,* [online] 2014, last revision 2014-06-12 [cit. 2014-06-12]. Available from: http://www.vuhz.cz/pages/cs/zamereni-firmy/s2/laboratore-a-zkusebny/laboratore-a-zkusebny.php

[79] AMERICAN SOCIETY FOR TESTING AND MATERIALS: *Manual on Use of Thermocouples in Temperature Measurement,* 1974, ASTM, USA

[80] TILLMANN, V., at all: Thermal Protection Shield Concept for Diamond Impregnated Tools. *Material Science Forum,* 2007, vol. 534-536, p. 1145-1148.

[81] HRNCIR, T.: *TEM lamella preparation* [online] 2011, last revision 2014-06-12 [cit. 2014-06-12]. Available from: http://www.tescan.com/en/applications/gallery/others/tem-lamella-preparation

[82] KOSTOV, A., FREIDRICH, B., ZIVKOVIC, D.: Predicting thermodynamics properties in Ti-Al binary system by FactStage. *Computational Material Science,* 2006, vol. 37, no. 7, p. 355-360.

[83] BARBOSA, J., at all: Influence of Superheating on Casting of Gamma TiAl. *Intermetallics,* 2007, vol. 15, no. 7, p. 945-955.

[84] HUMPHREYS, N. J., at all: Modeling and Validation - Casting of Al and TiAl Alloys in Gravity and Centrifugal Casting Processes. *Applied Mathematical Modeling,* 2013, vol. 37, no. 14-15, p. 7633-7643.

[85] AGUILAR, J., at all: Investment Casting Technology for Production of TiAl Low pressure Turbine Blades – Processing Engineering and Parameter Analysis. *Intermetallics,* 2011, vol. 19, no. 6, p. 757-761.

[86] WU, Y., at all: Influence of Y-addition on the Oxidation Behavior of Al-rich Gamma TiAl Alloys. *Intermetallics,* 2004, vol. 12, p. 519-532.

[87] LAMIRAND, M., at all: Relative Effect of Chromium and Niobium on Microstructure and Mechanical Properties as an Function of Oxygen Content in TiAl Alloys. *Scripta Materialia,* 2007, vol. 56, p. 325-328.

[88] KESLER, M. S., at all: A Study of Phase Transformation in a TiAlNb Alloy and the Effect of Cr Addition. *Material Science and Engineering A,* 2010, vol. 15, p. 350-357.

[89] BARBOSA, J., RIBERIO, C.: Influence of Crucible Material on the Level of Contamination in TiAl Using Induction Melting, *Internationa Journal of Cast Material Research,* 2000, vol. 12, p. 293-301.